TUM

Technische Universität München

TUM School of Natural Sciences

DFT Studies on the SnIP gas phase Mechanism and SnIP Hybrids

Markus Rudolf Peter Pielmeier, M.Sc.

Vollständiger Abdruck der von der TUM School of Natural Sciences der Technischen Universität München zur Erlangung des akademischen Grades eines

Doktors der Naturwissenschaften (Dr. rer. nat.)

genehmigten Dissertation.

Danksagung

Mein Dank gilt allen, die meine Zeit der Promotion mit Unterstützung, Anleitung und Kameradschaft begleitet haben.

Im Besonderen gilt mein Dank natürlich Prof. Dr. Tom Nilges, der mich zu jeder Zeit unterstützt und gefördert hat. Seine Betreuung ging weit über das rein Fachliche hinaus, wodurch wir alle auch als Personen reifen konnten.

Außerdem möchte ich an dieser Stelle Prof. Dr. Antti Karttunen von der Aalto University meinen herzlichsten Dank aussprechen, weil er mir ein unersetzbarer Mentor und Ansprechpartner während meiner ganzen Dissertation war.

Ein besonderer Dank geht zudem an meine lieben Kollegen in der Arbeitsgruppe für die kameradschaftliche Zusammenarbeit, anregenden Fachgespräche und unterhaltsamen Stunden. Hervorheben muss ich hier unsere gute Seele der Gruppe, Lucia Weissenborn, die unser Leben an der Universität nicht nur leichter, sondern auch wesentlich angenehmer gemacht hat.

Von Herzen möchte ich meiner Familie danken, die schon immer an mich geglaubt, mich wiederholt motiviert und mir immer mit Rat und Tat zur Seite steht.

Zu guter Letzt möchte ich meiner Frau, Tanja, meinen Dank aussprechen für ihr Verständnis und v.a. für all die tagtäglichen Kleinigkeiten, mit denen sie mir den Rücken frei hält.

Contents

Abbreviations

DFT	Density Functional Theory
PBE	Perdew-Burke-Ernzerhof functional from 1998
HSE06	Heyd-Scuseria-Ernzerhof functional from 2003
AOs	Atomic Orbitals
LCAO	Linear Combination of Atomic Orbitals
MOs	Molecular Orbitals
GGA	Generalized Gradient Approximation
ECP	Effective Core Potential
DOS	Density Of States
COHP	Crystal Orbital Hamilton Population
CVD	Chemical Vapor Deposition
CNT	Carbon NanoTube
hBN	hexgaonal Boron Nitride
C_3N_4	melamine-based Carbon Nitride
C_6N_8	tri-s-triazine-based Carbon Nitride
XPS	X-ray Photoelectron Spectroskopy
CalPhaD	Calculated Phase Diagram
(SW)CNT	(Single Walled) Carbon NanoTube
G	Gibbs free energy
E_{tot}	total Energy
K	Kelvin
kJ	kilo Joules
h	hour
D	Diameter

Zusammenfassung

In dieser Arbeit werden die Bildungsmechanismen von SnIP und schwarzem Phosphor zum ersten Mal detailliert beschrieben. Zusätzlich werden die energetischen Stabilitäten von einzelnen SnIP Strängen und ihrer Hybride mit 2D-Materialien für ausgewählte Beispiele gezeigt.

Ab-initio Rechnungen mit SnIP und verwandte Systeme werden im Rahmen von DFT auf GGA-Niveau (PBE) mit Dispersionskorrektur (D3) ausgeführt. Im ersten Teil wird seine Bildung in einer Gasphasentransportreaktion untersucht. Aufgrund der engen Beziehung zur $P_{schwarz}$-Synthese werden beide Bildungsmechanismen unter Berücksichtigung experimenteller Daten und CalPhaD aufgeklärt. Die Synthese von $P_{schwarz}$ beginnt bei 923 K mit dem direkten Angriff von SnI_2 auf weißen Phosphor, der bereits teilweise zu P_2 zerfällt. Das führt zur Bildung eines Dimers, das durch vier SnI_2 stabilisiert wird. Dies ist der Ausgangspunkt für eine Polymerisation, die unendliche Phosphorenschichten wachsen lässt, die zu schwarzem Phosphor gestapelt werden können. Bei 673 K entsteht SnIP durch den Angriff zweier SnI_2-Dimere auf einen weißen Phosphortetraeder. Dieser Baustein kann polymerisieren und je nachdem, auf welcher Seite die Phosphor-Butterfly-Unterstruktur geöffnet wird, können beide Chiralitäten von SnIP erhalten werden.

Die Stapelreihenfolge wird ebenfalls untersucht und das Racemat, als das es im Kristall vorliegt, wird energetisch um 8,5 kJ/mol begünstigt. Als Matrix für eine Bottom-up-Synthese von einem einzelnen SnIP-Strang werden aufgrund ihrer vielseitigen Eigenschaften zunächst die CNTs untersucht. Eine Verringerung des Durchmessers kann wie das ausüben von Druck auf das System angesehen werden, was am besten in der Schwingungsanalyse zu sehen ist. Ein leichter Druck auf die äußere Helix führt zu einer Entspannung der inneren Helix, bevor sich bei höheren Drücken der Effekt umkehrt. Bisher hatte die Chiralität der Matrix keinen Einfluss auf die Stabilisierungsenergie der SnIP-Enantiomere. Dies gilt auch im nächsten Schritt, wo der Matrixdurchmesser konstant gehalten wird (13,1 - 13,8 Å) und aufgerollte 2D-Schichten mit unterschiedlichen Eigenschaften zu 1D-SnIP@2D-Materialien kombiniert werden. Neben den energetischen Aspekten werden die COHPs verwendet, um Informationen über die Natur der Wechselwirkungen an der Grenzfläche zwischen Matrix und SnIP zu extrahieren. Das allgemeine Bild zeigt, dass die Atome in der Nähe dieser Grenzfläche bereits elektronisch gesättigt sind, was zu hauptsächlich antibindenden Zuständen in der Nähe des Fermi-Niveaus führt. Um besser adaptierende Matrizen zu entwickeln, sollten weitere Versuche mit dotierten oder funktionalisierten 2D-Materialien umgesetzt werden.

Abstract

In this work for the first time the formation mechanisms of SnIP and black phosphorus are described in detail. Additionally, the energetic stabilities of single SnIP strands and their hybrids with 2D materials are shown for selected examples.

Ab-initio calculations with SnIP and related systems are carried out in the framework of DFT on the GGA level (PBE) with dispersion correction (D3). In the first part, its formation in a gas phase transport reaction is explored. Due to the close relation with the P_{black} synthesis, both formation mechanism are elucidated while respecting experimental and CalPhaD data. The synthesis of P_{black} starts at 923 K with the direct attack of SnI_2 on white phosphorus, which is already partially decomposing to P_2. That leads to the formation of a dimer and two adjacent P atoms stabilized by four SnI_2. This is the starting point for a polymerization that can grow infinite phosphorene sheets, which can be stacked to form black phosphorus. At 673 K SnIP is formed by the attack of two SnI_2 dimers on a white phosphorus tetraeder. The resulting building block can polymerize and depending on which side the phosphoric butterfly substructure is opened, both chiralities of SnIP can be obtained.

The stacking order is also investigated and the racemic mixture as present in the bulk is energetically favored by 8.5 kJ/mol. As matrix for a bottom up synthesis of single strand SnIP the CNTs are investigated first because of their versatile properties. A reduction in diameter can be interpreted as pressuring the structure, which can best be seen in the vibrational analysis. A slight pressure on the outer helix leads to a relaxation of the inner helix, before at higher pressures the effect is reversed. Up until now, the chirality of the matrix did not influence the stabilization energy of the SnIP enantiomers. This also holds true in the next step, where the matrix diameter is kept constant (13.1 - 13.8 Å) and rolled-up 2D sheets with differing features are combined to 1D-SnIP@2D materials. Besides the energetic aspects, the COHPs are used to extract information about the nature of the interactions at the interface between matrix and host. The general picture indicates, that the atoms near this interfacial area are electronically saturated, which leads to mainly antibonding states near the Fermi level. To develop better adapting matrices further adjustments with doped or functionalized 2D materials should be implemented.

1 Introduction

Our way of life is heavily dependent on the technological advancements, which are always supported by materials science. It is defined as the relationship between the structure and the properties of the respective material and has a long history. In ancient Rome, there were already books about this topic describing in detail the properties and the hardening process of concrete, where the components can be found and why they are formed in special places[1]. This macroscopic approach was the only possible way until more sophisticated analytical methods in physics and chemistry were developed. An essential milestone depicting this process is the periodic table of the elements, which was introduced in 1869 by Dimitry Mendelejew. It can also be regarded as the register for mono-atomic materials, in which they are grouped by properties[2].

After the elements and their properties were explored, scientist logically ventured in the fields of higher order systems. Well known pioneers for binary phases like E. Zintl or W. Hume-Rothery were able to not just enlarge the knowledge about material properties, but also deepen the understanding of basic concepts in chemistry. Just to name two examples, there is the theory of super-lattice structures in alloys emphasizing the importance of annealing or the Zintl concept deduced from the anomalies in inter-metallic phases containing alkali or alkaline earth metals[3, 4]. Another important milestone for humanity is the development of transistors in Bell Labs in the late 1940s. They are up until today the most commonly known area of application for semiconducting materials, which thereafter got a huge boost in scientific and commercial interest. A myriad of things that were engineered in the last century are based on transistors and facilitate the simple life on earth (e.g. radio, phones, vehicles and computers)[5]. As the need for improvement in certain areas became obvious and the knowledge base got more extensive, the idea of analyzing materials to know their properties slowly has been reversed to the design of materials for specific predetermined applications, also known as material engineering.
A prominent example thereof are battery materials, which are synthesized in order to meet the high-energy demand of modern, rechargeable lithium ion batteries[6]. In this field of research, the driving force for improvement of the material design and the engineering capabilities to develop "next-generation" technologies is explicitly visible[7]. Before storing power in batteries, it has to be converted to electrical current, which is happening e.g. in solar cells. Aside from the classical silicon based cells, there are various approaches from material science to further enhance the conversion rate and still use abundant resources. Examples for these new solar cell materials are thin films of cadmium telluride and copper indium gallium di-selenide, nanocrystalline titanium

dioxide or any combination of donor and acceptor polymers[8].

In this century a great number of such artificially made materials, which exhibit astonishing properties (e.g. with negative values for index of refraction, electrical permittivity or magnetic permeability) that are not found in natural variants, were published and are referred to as metamaterials[9]. In order to obtain such a material, usually a symbiotic cooperation of divers disciplines is essential (e.g. optics, acoustics and solid state chemistry). The Journal of Optics titled an overview article on this matter with "The century of metamaterials", even though the term is known for hardly two decades, to highlight their impact on the basics of optics and other sciences[10].

The responsibility of material science doesn't end there, on the contrary, the problems are just starting. After designing, synthesizing and characterizing e.g. a new solid state material, the technical hurdles on the way to commercialization are enormous. Depending on the final application (e.g battery material, sensors, catalysts, etc.) different prioritization of the properties and follow up testing is needed[11]. The results of these tests can nowadays be estimated beforehand with the help of DFT, where e.g. the structural stability can be correlated to the formation or free energy calculations. Also the analysis of the electronic structure or charge distributions can be used to predict transport kinetics or adsorption processes[12]. A descriptive example for this approach is the reduction of energy disorder in Sn-Pb alloyed perovskite solar cells. Here, the author reports that the combination of 1-bromo-4-(methylsulfinyl) benzene (BBMS) and SnF_2 greatly restrains the oxidation of Sn^{2+}. DFT helped to clarify the reason for the improvements, which is the interactions between BBMS and the perovskite, yielding unusually stable, highly efficient devices at temperatures of up to 60°C [13].

1.1 Semiconducting Materials

Though transistors are known for more than 80 years now, the evolution of semi-conducting materials is far from over. Nowadays, they are subjected to the needs predefined by their applications and are widely researched in the material science community[14]. A semiconductor has the electrical properties of an insulator at ground state, but it's band gap is small enough so it can be overcome by thermal activation of the electrons from the valence band into the conduction band. Another way to look at this phenomenon is, that there is no difference between semiconductor and insulator at 0 K, while metals are still able to transmit current under this condition. In comparison to an insulator, when the temperature is rising, the conductance of the semiconductor also increases proportionally to the population of the conduction band[15]. Alterations like doping, delamination or particle size reduction can tune the performance of the material. Doping for example increases the number of electrons in the conduction band (n-type) or the number of electron holes in the valence band (p-type), which both boost the conductance. More mechanisms for band gap engineering are size, shape and composition control, hetero-structure band offset and lattice strain[16].

The monolayer element allotrope of black phosphorus (P_{black}) is called phosphorene, which is a semiconductor with intriguing physical properties and application potential as gas sensor, FET or lithium ion battery material[17, 18, 19]. The atomic arrangement is comparable to a corrugated graphene sheet, from which phosphorene distinguishes itself by a fundamental band gap and a high hole mobility[20]. In 2016, a procedure to directly synthesize thin film phosphorene by CVD was introduced[21]. Before that, the only way to obtain phosphorene in a reliable manner was the mechanical exfoliation from P_{black} (Figure 1a).

A phase pure synthesis procedure was developed in our work group, resulting in a scalable CVD process published in 2007[22]. Furthermore, it could be affirmed by in situ neutron diffraction, that P_{black} was formed directly from the gas phase[23]. Aside from the reaction conditions and reactants, nothing about the formation mechanism or the reactive species was known. Consequentially, the starting point for the development of catalytic and mineralizer concepts based on well-grounded facts was missing. During the optimization of reaction parameters an interesting, needle-shaped side phase, which turned out to be SnIP (Figure 1b), appeared. Why P_{black} and SnIP can be obtained from the same starting materials with slightly different temperature profiles and molar ratios is a vital question and motivation for this work.

Double helices are interesting mysteries for scientists since the discovery of DNA in 1953 and pose a significant challenge in synthesis[24, 25]. In 2000, first experimental results hinted towards helical arrangements of atomic chains in matrices like iodine
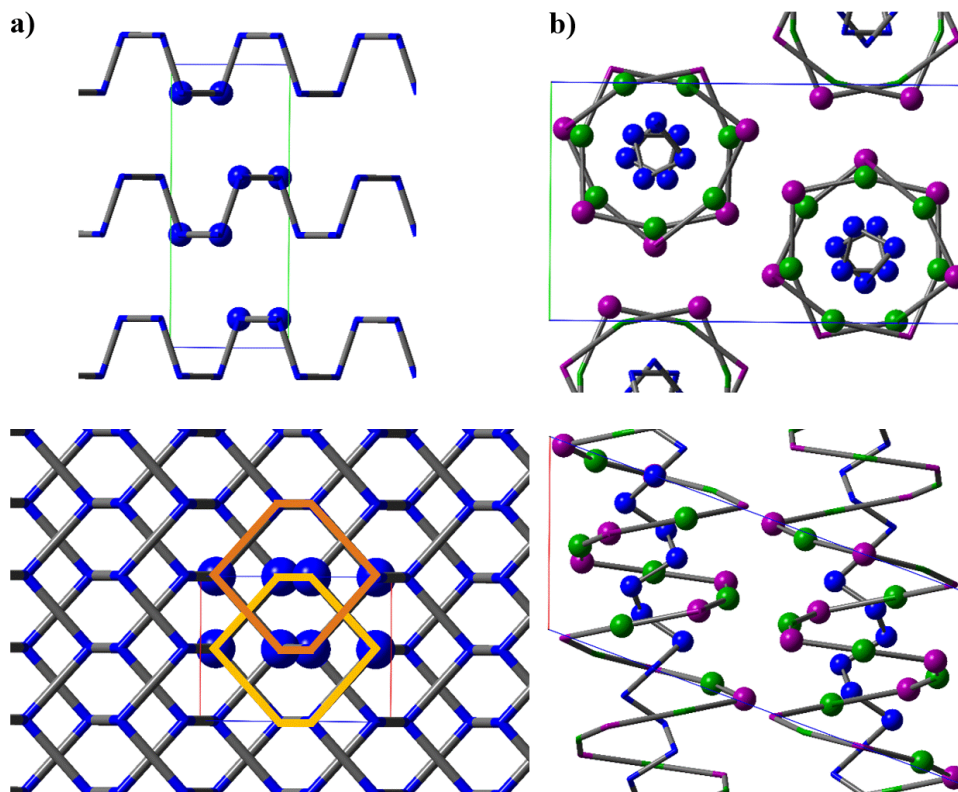
Figure 1: Crystal structure sections of a) P_{black} and b) SnIP. On the top, the view is along the a-axis, while on the bottom the projections are shown along the b-axis. Atoms inside the first unit cell are shown additionally with balls, while the rest is depicted with sticks only. Orange hexagons illustrate the stacking order AB in P_{black}. These graphics are excerpts from 3.1.

in CNTs[26]. In the last decade, there was more success forming small double helical systems using templates, e.g. with selenium, sulfur or LiP in CNTs, but only after their prediction by theory[27, 28, 29]. After the discovery of SnIP, chemically related ternary compositions under the same synthesis conditions usually yield the thermodynamic product, which is in most cases the clathrate[30]. Only theoretically predicted homologues, although a considerable number of them, were known[31]. In 2022, finally one of the predicted double helical structures, SnBrP, was published as the second representative of this new, double helical, ternary material class[32].

The first inorganic, atomic-scale, one-dimensional and nontemplated double helix was patented in 2015 and published in 2016 by our work group[33, 34]. It is composed of an inner $[P]^-$ helix and an alternating outer $[SnI]^+$ helix (see Figure 2) consisting of 7 and 14 atoms within the translation unit, respectively. The diameter of a single double helix is 9.8 Å, while the mean bond lengths are $P-P = 2.20$ Å, $Sn-I = 3.16$ Å and $Sn-P = 2.69$ Å. SnIP crystallizes in an unit cell with the space group $P2/c$ (No. 13), which contains two double helices with different winding directions, thus forming a racemic mixture of M- and P-SnIP in the bulk. This nomenclature of the right
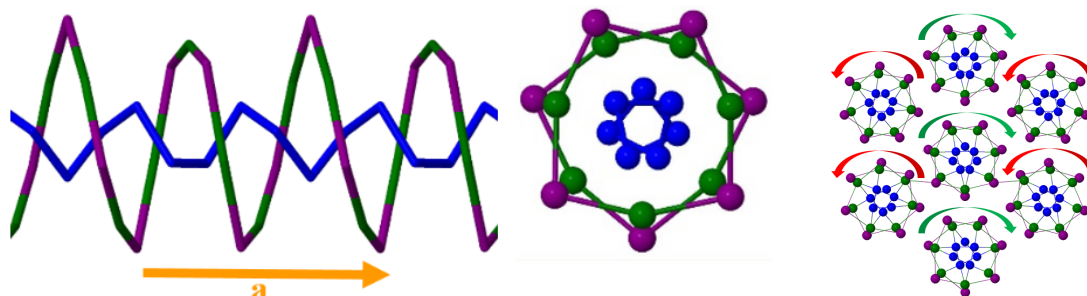
Figure 2: A single P-SnIP rod is shown with view along the c- (left) and the a-axis (middle). The orange vector on the left marks the translation unit along the a-axis of the sticks representation. For all other structures, the balls and sticks depiction is used. On the right, the first shell of the pseudo hexagonal rod packing surrounding a central P-SnIP strand is illustrated. M- or P-SnIP is determined respectively by the red or green arrows and they are arranged as found in the bulk material. These graphics are excerpts from 3.2.

(M)- and left (P)-handed helices and the general application of rod symmetry rules is discussed in detail by Prof. U. Müller[35]. The cell parameters for this monoclinic structure are $a = 7.934(2)$ Å, $b = 9.802(3)$ Å, $c = 18.439(9)$ Å and $\beta = 110.06(5)°$[34]. To achieve the racemic mixture in the bulk different arrangements of rod packages are thinkable. The pattern indicated in Figure 2 on the right is verified by experiment and reconfirmed by theory[36]. The phase pure preparation of SnIP is possible on a gram scale in a simple solid state annealing reaction from tin, phosphorus and tin tetra-iodide at 673 K[34]. Later, a yield optimization could be accomplished by substituting Sn/SnI_4 for Sn/SnI_2, thus suggesting a beneficial role of SnI_2 in the synthesis.

1.2 Quantum Mechanics

The theory behind all calculations today was established from classical mechanics. The first models for point charges were set up by the formalism of Newton and Hamilton, providing the canonical equation of motion (equation 1) for a quantum mechanical particle (e.g. an electron)[37].

$$H = \frac{p^2(r)}{2m} + V(r) \tag{1}$$

Here, H stands for the Hamilton function, p is the momentum, r is the three dimensional position vector, m is the electron mass and V is the potential energy. However, solving this equation for electron trajectories in atoms could provide a satisfying solution for emission spectra of light atoms only. In order to solve this problem completely, many scientists had to come up with brilliant ideas to simplify the divers interactions in an atom. To name only a few, there was the Born - Oppenheimer approximation[38], which decoupled the core - electron relations, the Heisenberg uncertainty principle[39, 40], which explained why only position or momentum of an electron could be determined at a certain moment in time, and finally the operator based Schrödinger equation[41], which unifies all possible states of measurable quantities. In equation 2, a wavefunction $\psi(r_1, ..., r_N)$ (N is the number of electrons) is described as a stationary electronic state, which satisfies the time-independent Schrödinger equation[37].

$$\hat{H}\psi = [\hat{T} + \hat{V} + \hat{U}]\psi = E\psi, \tag{2}$$

All letters with a hat still represent the same quantity as before, but as an operator. The new denominations are $\hat{T}$ as the kinetic energy, $\hat{U}$ as the electron - electron interaction energy and E as the total energy of the system. This complete Hamiltonian can be expressed as a sum of all electrons in the system, the many electron Schrödinger equation[37].

$$\hat{H} = \sum_{i=1}^{N}(-\frac{\hbar^2}{2m_i}\nabla_i^2) + \sum_{i=1}^{N} V(r_i) + \sum_{i<j}^{N} U(r_i, r_j) \tag{3}$$

$\hbar$ is Planck's quantum of action and ∇ is the Laplace operator, which splits the kinetic energy term in three orthogonal portions following the Cartesian vectors. Equation 3 is not separable into simpler single particle terms because of $\hat{U}$, which is dependent on all possible, non-repeating interactions of r_i and r_j[37].

Nowadays, there are many sophisticated methods to solve the Schrödinger equation after expanding the wavefunction in Slater determinants. Under the precondition of standardized, linearly independent elements, a combination of orbitals can be con-

structed and mathematically modified without changing the value of the determinant. This was introduced in 1929 as a means of ensuring the anti-symmetry of a many-body wavefunction[42].

The procedure to calculate energies by approximation of the previously mentioned many-body, time-independent Schrödinger equation was introduced by Hartree in 1927[43]. In the course of this work, the requirement of the self-consistent charge distribution when comparing calculated and initial field was formulated (SCF). Only one year later, the variational principle was introduced and applied on an ansatz, which was a product of single-particle functions by Gaunt[44]. However, the lack of anti-symmetry in the Hartree product was a fundamental flaw and hurt the Pauli exclusion principle[45]. In 1930, Fock showed, that a diagonalized Slater determinant of one particle orbitals can cope with the anti-symmetric nature of the exact solution and hence the variational principle could be applied successfully[46].

$$\langle E \rangle \geq E_0 \tag{4}$$

In essence, the variational principle in equation 4 states, that under the preconditions of normalizability, continuity and non-ambiguity the ground state E_0 is the bottom threshold for the expectation value of the energy $\langle E \rangle$. Hence, the obtained expectation value after the application of this principle acts as the upper limit for the calculated system's real energy[37]. All historic contributions up to now resulted in the SCF procedure as we know it today. Even though achievements in this area keep enhancing the computational effectiveness like Anderson, Broyden and Pulay[47, 48, 49], the essential steps still depend on the striking success of the here mentioned pioneers.

In Figure 3, the whole phrasing is already in terms of DFT, as this is the method exclusively used in this work. But by replacing the words electron density with molecular orbitals and Kohn-Sham hamiltonian with Fock matrix, the cycle holds true, too. The difference is mainly in the way the ansatz is processed, meaning in the Fock matrix the coordinates for each particle is generated independently, while in the Kohn-Sham approach a single electron cloud is constructed.

For completeness, it should be mentioned here, that at the same time (1925 - 1932) experts of the MO theory like Friedrich Hund and Robert Mulliken already established their own descriptions of chemical bonding[50, 51, 52]. The detailed assignment of quantum numbers or the classification and definition of bonding situations through the atomic electron eigenfunctions between two atoms was a fundamental contribution for all molecular simulations[53, 54, 55]. The fact, that the interchangeable one particle
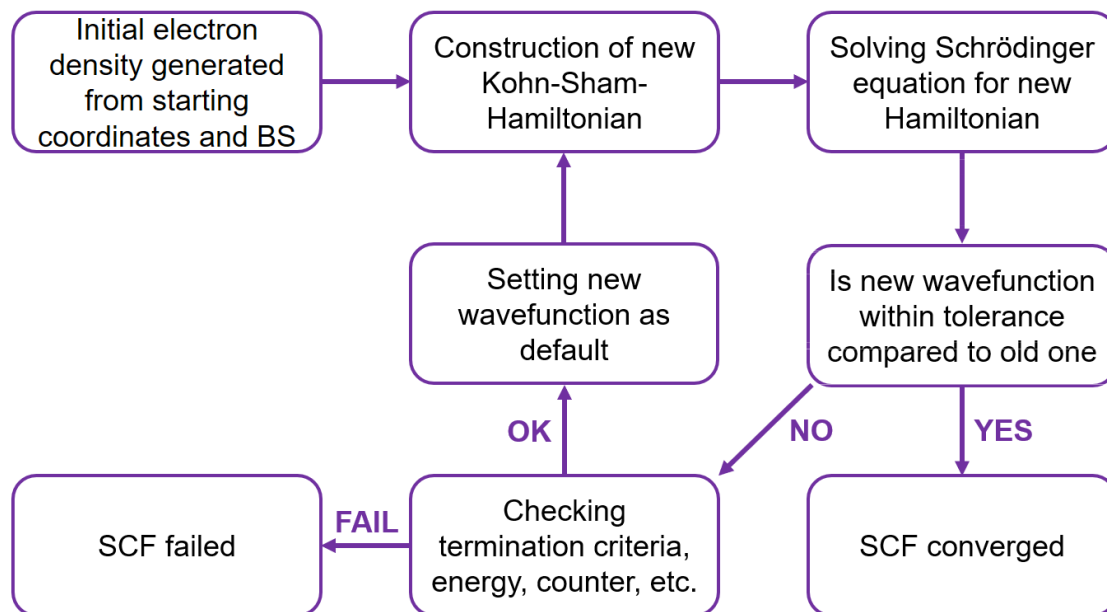
Figure 3: Schematic diagram of the essential steps in a SCF procedure with DFT starting conditions.

orbitals in the Slater determinant made the integration of these concepts into the calculation scheme relatively intuitive was one of the major advancements in the whole field of theoretical chemistry, comparable with the introduction of computers many years later.

1.3   High Performance Computing

High performance computing (HPC) summarizes all processing operations done with supercomputers, which have a significant higher number of CPUs than personal computers. Due to the sheer amount of data generated, this usually also leads to an enhanced network infrastructure for data transfer. Of course, there are many possible ways to install such systems, but normally they are arranged in clusters of machines, called nodes. Each of those contains a fixed number of CPUs, that can be used for the software applications. When storing many of these nodes together in a confined space, the heat dissipation is one of the obvious problems and it can be solved in various ways[56].
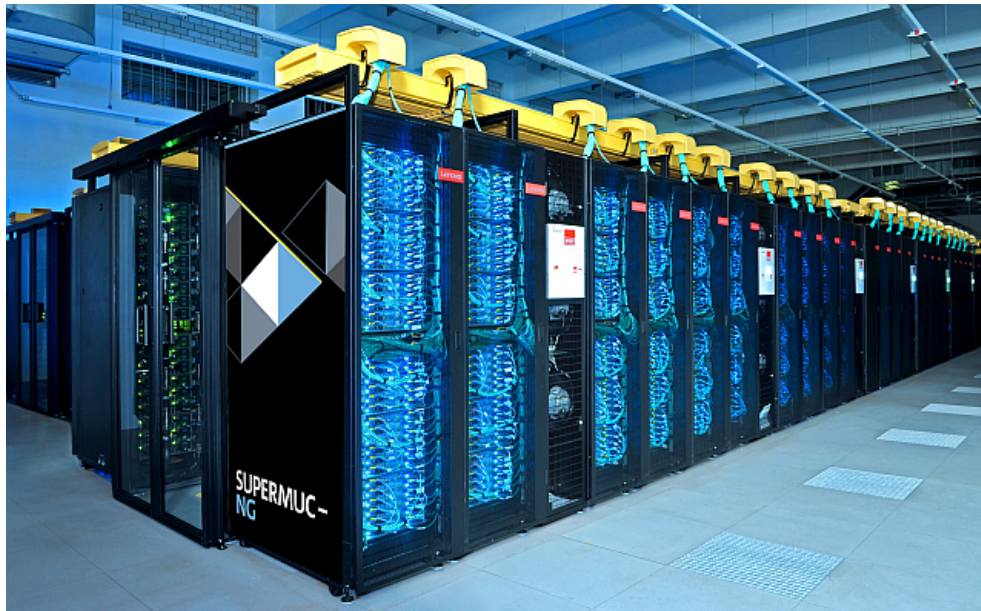

Figure 4: A picture the HPC cluster fo the SuperMUC-NG in the LRZ, taken from their website: https://doku.lrz.de/download/attachments/43320790/image2019-11-15_12-48-5.png?version=1&modificationDate=1594900824290&api=v2. The stacking of the nodes in the racks and the network connections on the top are visible.

In the Leibniz Rechenzentrum (LRZ), the supercomputing center of the TUM, this is solved by a warm water cooling loop (max 55°C), which is surcharged only in the range of 10% of the energy spent on operating the whole IT equipment. Usually such sites operate the cooling cycle in the order of 30-50% of the yearly energy costs, meaning the LRZ installed already in 2011 an energy efficient heat absorbing system. Furthermore, the heated water can be reused for heating and adsorption refrigeration, which makes it even more sustainable[57].

The LRZ hosts more than 300.000 computing cores with a main memory of over 700

TB. The SuperMUC-NG, as the newest system is named, holds 6.480 nodes with 48 cores each, while the older ones are called CoolMUC(-2 and -3). Those are based on 28 and 64 core nodes, respectively. All of them have a large variety of capabilities like MPI, OpenMP, secure shell data access, development environment and the SLURM scheduler[58]. Parallel processing is used in the CRYSTAL17 program, which is the most computation power consuming package in this work. Especially, when the 1D-simulations without symmetry restrictions and more than 200 atoms are done, sometimes even the combined power of up to 8 nodes for 72 hours was not enough to finish the job in one attempt.

Consequently, scientist using quantum mechanics are also attracted by the new advantages of quantum computing (QC). The rapid progress in this field nurtures the hope for powerful quantum machines, which could herald enormous improvements in theoretic chemical research[59]. The idea, that quantum computers could be used to describe natural phenomenons in a simulation exactly due to their shared working principles was already published in 1982 by Feynman. He even points out the need to rethink our reasoning, observations and measurements in the face of these new QC systems, which leads to an interesting philosophical discussions[60].

In the classical computational logic, the information carrying bit is binary, usually denoted with 0 or 1. The approach in QC is different, because the information can be stored on so called qubits, which carry them on the surface of a Bloch sphere in a linear superposition[61]. This feature alone outperforms the classical memories by far and is supplemented by entanglement, which enhances parallel computing and processing of data exponentially[62]. As this is the source of power for QC systems, one can imagine the challenges entailing the switch to such complex qubits. The need to reformulate and adjust the programming, reevaluate the constraints and reinvent the cornerstones of theoretical chemistry is mandatory for a successful transition. Despite the relatively recent emergence of QC, relevant developments concerning simulations in quantum chemistry have already been made[63].

2 Methods

2.1 Density Functional Theory

DFT is a computational, quantum mechanical modeling method for structure exami-
nations of the ground state in many-body systems. Already in 1935, Manning could
show that an exact solution of the one dimensional Schrödinger equation is possible. For
many-body systems this is also possible with the configuration interaction method, but
it requires an substantial amount of computational power, even for small molecules[64].
Many scientists tried to refine the post Hartree-Fock methods, but there were a few
ingenious brains working on a completely new approach. The idea was to represent
any configuration, whether it was 3D or a molecule, with the unique electron cloud for
each system[65]. At first, this seemed to be a crude approximation, but it has the un-
deniable benefit, that you only have to keep track of one spatial coordinate. However,
the energy is only obtained after approximating the exchange correlation functional,
which is unknown for new systems. Different approaches to determine this part of the
equation lead to various classes of such functionals with differing goals. In figure 5 an
overview of the classes (left side of the ladder) and of the most popular functionals of
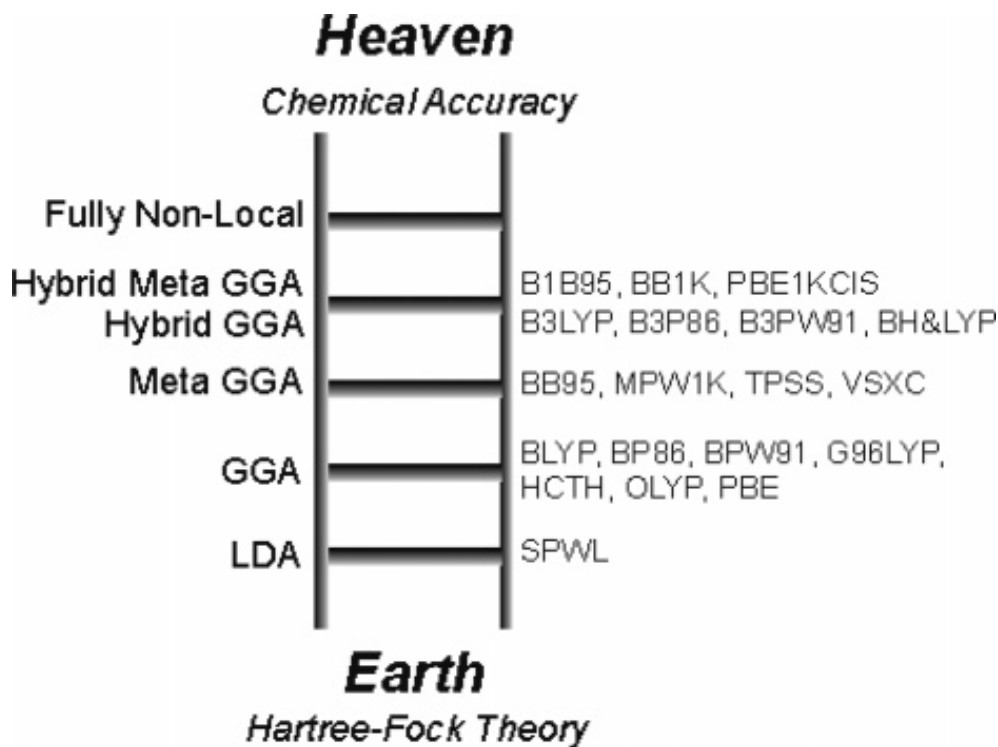these classes is depicted.

Figure 5: Jacob's ladder of chemical accuracy with five levels for the different genera-
tions of functionals - excerpt from an article of S. F. Sousa et al[66].

The basic approach to structure optimization is summarized in Figure 6, as this is in most cases the prerequisite to all subsequent computations. Even if there is no immediate need of a geometry optimization before these property calculations, practical experience indicates a much higher success rate for obtaining reliable and consistent data sets when an optimized structure is used. Taking the fact into account, that the ansatz for the structure might not be very accurate (e.g. geometry generated by hand), this is the logical consequence because the expectation value of the systems is usually lowered in the process.
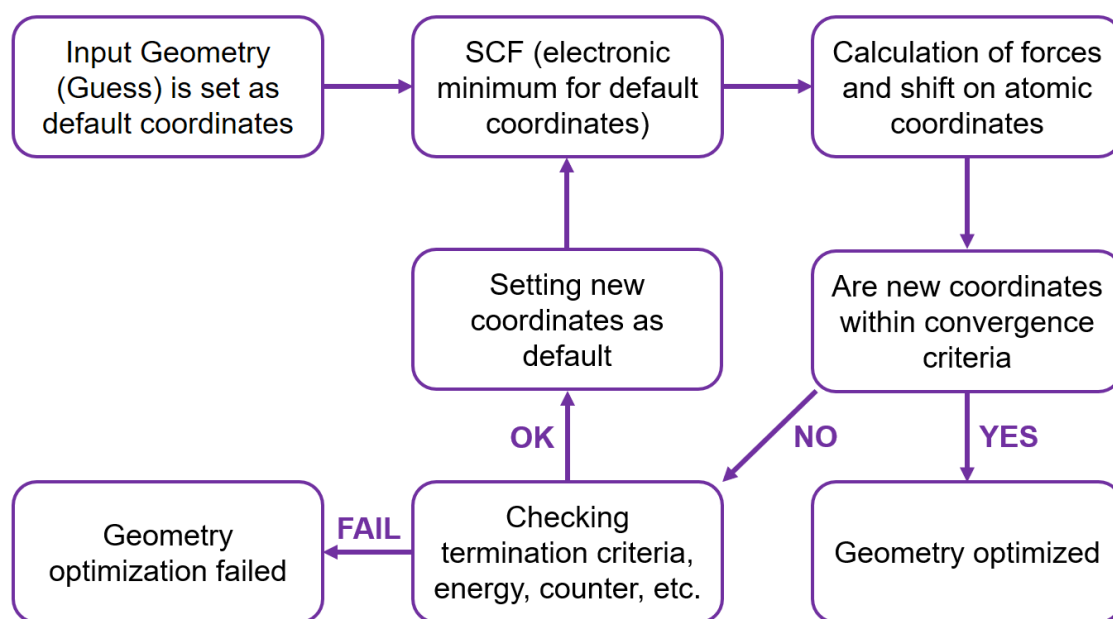

Figure 6: Schematic diagram of the essential steps in a structure optimization procedure with DFT starting conditions.

In figure 6 the repetitive character of the optimization steps is emphasized. The cyclic procedure is started with a guess, meaning a set of input coordinates and basis sets from which the electronic structure is derived. Then the Hamiltonian is constructed, the SCF (see figure 3) is carried out for this set of coordinates and finally the forces in the system are estimated by derivation. The direction and magnitude of these forces are used to create displacement vectors for the atom cores, producing a new set of coordinates, which are checked for the defined convergence criteria. If the initial guess was good enough, the end is reached, if not the termination parameters must be tested. Correspondingly, if the first ansatz was too bad, the optimization fails here, but in all other cases the new coordinates run the same procedure as the initial guess again until the convergence criteria are fulfilled or the iteration fails a termination criterion.

Over the years, many methods to reduce the need of computational power of this cycle were developed. Logically, the best approach to make this cycle more efficient is

either to make the SCF faster or to make the steps needed to reach the minimum less. The optimum would be reached by applying both of these concepts without loosing accuracy. In the SCF, the direct inversion of the iterative subspace (DIIS) as proposed by Hamann in 1979, which mixes Fock and Kohn-Sham matrix derivatives, is the default convergence accelerator in CRYSTAL17[67, 68]. Theoretically, the minimum structure can be found in a single optimization step, if the initial guess is within a basin of attraction of the minimum with the Newton-Raphson method[69]. However, there are some downsides like the need of an exact, non analytical derivative or a potential poor starting point to this procedure. That is why the applied procedure in CRYSTAL17 is called a quasi-Newton algorithm, which is a lot less susceptible to the aforementioned problems[70].

There is a myriad of possibilities to apply DFT in material science and here just a few recent examples are mentioned in order to emphasize the diversity. First, there is a study about the chemisorption of CH_4 and CO_2 at Zn_nO_n (with n = 12, 15, 18, 20, 22 and 24) nanoclusters. It shows the favorable electronic and reactive properties of $Zn_{22}O_{22}$ in this material class. The comparison of the results is in good agreement with experimentally obtained data and leads to the conclusion, that bio-safe sensors made up of ZnO nanoclusters for gas sensing should be feasible[71]. Furthermore, the work about the regioselectivity of the catalyst in the hydroformylation reaction is more complex than anticipated by the authors. The usage of biphosphine ligands with a carboxylate binding site in the supramolecular substrate leads to excess aldehyde formation in all reported cases of alkenes. Mechanistic and energetic insights into the regioselective, rhodium-based catalytic reaction are detailed enough to potentially influence future designs of new catalysts for selective transformations[72]. Finally, there is a multi-methodological approach to the detailed structure anaylsis of scandium oxychloride (ScOCl) by sampling its entire energy landscape. It was performed with Monte-Carlo walks (length of 3000 steps each) and supported by a simulated annealing based algorithm for global optimization. While the already known α- and β-phase appeared several times as highly symmetric minima during global optimization, the unknown γ- and δ-modifications could also be identified. After that, *ab-initio* optimizations with different functionals as well as *E(V)* and *H(p)* curves for these phases were calculated. The newly predicted structures should now be further researched with high temperature and high pressure synthesis experiments[73].

2.2   CRYSTAL17

The CRYSTAL17 code was published by the University of Torino and is continuously developed since 1988[74]. There are numerous program features provided and even more people contributed to its evolution. Here, some of the program packages, that are vital for this work, are mentioned, but the full list, a detailed description and all of the cooperators can only be found in the manual[70].

CRYSTAL17 is designed for *ab initio* calculations on the potential energy surface and properties of periodic systems. Periodicity in 3 (crystals, 3D), 2 (slabs, 2D), 1 (polymers, 1D) and even 0 (molecules, 0D) directions is treated equally with either Hartree-Fock (see 1.2) or Kohn-Sham Hamiltonians. In both cases, the single particle functions made up of a linear combination of Gaussian type functions are defined in the input by the basis set option. Those are expanded to AOs by the linear combination of Bloch functions[75].

The automated handling of 230 space groups, 80 layer groups, 99 rod groups, 45 point groups and an expanding number of helical rod groups is utilized for the construction of complex input and the reduction of its computation time. Input tools help with the transformation of 3D systems to slabs (2D), polymers (1D), clusters (0D) and even nanotubes. When the desired structure is composed, every atom can still be altered separately to simulate e.g. doping, solid solutions, vacancies, etc.

One major advantage of CRYSTAL17 is the possibility of using detailed, adaptable and properly explained functions for a large variety of applications without loosing the simplicity of the input. On one hand, a single point calculation for a known structure can be finished with hardly any parameters needed for the keywords, as there are default options defined in most cases. On the other hand, there is a logical series of steps the program is processing, which allows the user to generate e.g. a structure optimization with convergence accelerator, a mulliken population analysis, a band structure, a projected density of states and a COHP analysis with a single, well prepared command.

One of the newest features is the modeling of periodic, helical nanostructures in an efficent way. The new algorithm can interpolate between the properties of a sequence of periodic substructures in order to get the properties of the 1D helix without the translational periodicity[76]. The results show, that several potential energy local minima are present in these systems, depending on the irrational order of the helical axis.

The CRYSTAL17 package is not only constantly expanded, but also increasingly ap-

plied in property studies for a vast variety of new materials. A few recent examples for such investigations are the magnetism-induced spin splitting of crystals[77], the heterojunction formation in a molybdenum disulfide/graphene heterostructure[78] and the construction of active sites for catalytic oxygen evolution reaction[13]. 3.2 and 3.3 exhibit the energetic stability and heterojunction formation of the examined hybrid materials, while the reactivity of white phosphorus inside carbon nanotubes[79] and the feasibility of comparable studies within the framework of the CRYSTAL17 code are affirmed[80].

2.3   Crystal Orbital Hamilton Population

The crystal orbital Hamilton population is a partitioning method for analyzing the k-space dependent wavefunction. In contrast to the crystal orbital overlap population, the COHP partitions the band structure energy rather than the number of electrons. A simple energy integral of a calculated COHP curve has an energy value as result, that hints towards the bond strength. As it partitions the one-particle eigenvalues (not the total energy of the system), it does not exactly equate the bond strength. However, the authors state that they are highly instructive, when put in the right perspective[81].

Historically, the development of the code was started in the 1980s in the Max-Planck-Institute for Solid State Research in Stuttgart, Germany. Everything started in the work group of Prof. A. Simon, where R. Dronskowski was responsible for the implementation of the code for the *Hamilton-projected densities of states* subroutine on a 6 MHz computer. First calculations were carried out with crystalline silicon and molybdenum clusters, but remained unpublished until Dronskowski returned from his postdoctoral time in 1993[82]. More and more projects were conducted under his lead and made the method known to the community. One example thereof is the examination of the bonding in perovskite-type oxynitrides (ABO_2N), where the COHP analysis is used as theoretical proof for the optimization of the metal-nitrogen bonds. This is achieved by distortion of local site symmetries from cubic to orthorombic, while keeping the macroscopic cubic description for the unit cell[83].

This method has been implemented in various known code packages for quantum chemical simulations like CRYSTAL17 or VASP as optional functions. Local Orbital Basis Suite Toward Electronic Structure Reconstruction (LOBSTER) is the newest software for interpreting chemical bonding by an analytic projection from projector-augmented wave DFT computations[84]. Nowadays, the algorithm is still evolving, meaning the procedure is made more efficient, more versatile and more automated. Recent developments make it possible to illustrate the results via plots, give textual descriptions and provide key data in machine-readable format[85, 86].

2.4   GAUSSIAN09

GAUSSIAN09 is a quantum mechanical code optimized for the prediction of energy, structure, vibrational frequencies and many more properties of molecular systems in different chemical environments[87]. Furthermore, it offers tools for influencing the re-searched systems with e.g. electric fields or solvents[88, 89]. In contrast to the text based input in CRYSTAL17 it is equipped with a formidable graphical user interface, featuring options like bond length and angle manipulation, fragment builder, valence addition, image generation, pre-optimizations with molecular dynamics and simulation parameter settings[90].

The code is able to perform molecular dynamics or quantum mechanics with HF (see 1.2) and DFT (see 2.1) procedures on diverse levels. As implemented post-HF meth-ods, examples like Moller-Plesset, Coupled Cluster and Brueckner doubles should be mentioned. In 3.1, DFT on the GGA level with the PBE functional was used for all optimizations, frequency and thermodynamic calculations. The structure models are illustrated with 75% vdW radius for all atoms in the visualization tool GaussView. In order to obtain 3.1, an extensive *ab initio* study in the gas phase was initiated, in which a very large number of chemically sensible structures are probed for their energy. This is repeated for every reaction step between the known products SnIP and P_{black}, while comparing the energy of every intermediate structure to the educts.

The number of such probing works is rising in recent publications, because the accuracy of the predictions are constantly increasing while a substantial amount of resources can be preserved. This is especially true for scarce and/or expensive elemental materials like palladium or gold in catalysis[91].

2.5   Calculated Phase Diagrams

Since the 1980s the assessment of the thermodynamic stability is an important tool to test the accuracy of the applied theory. Especially well observed phase diagrams of alloys were used to substantiate the and improve the programs to calculate them[92]. In general, such a code uses a numerical procedure to evaluate a reaction matrix and follows criteria for inclusion and elimination of condensed phases, meaning it is heavily dependent on stoichiometry and parameters[93].

Here, the programm Tragmin Verison 5.1 is used to estimate the gas phase species in a closed, evacuated ampule, because it was optimized for solid state - gas phase equilibria in chemical transport reactions[94]. In the graphical user interface any number of solid phases can be given, complemented by the mass, the volume, the number of atoms, the pressure, the length of the ampule and the temperature steps and range. When the input is combined correctly, transport rates, partial pressures and solubility of components is calculated and graphically processed within seconds. In 3.1, the gas phase atmosphere was calculated from the known initial weights and used to indicate the most probable starting materials for the unknown mechanisms.

This program was already used on divers gas phase composition problems in literature like the chemical vapor transport of bismuth and antimony chalcogenides in order to reduce experimental effort[95]. Another example is the exploration of complex crystal formations in rare earth phosphates, arsenates and antimonates after chemical vapor transport and the therefor responsible species in gas phase, which can be unexpected in some cases (e.g. $TeOCl_2$ instead of $TeCl_4$)[96].

3   Results

3.1   Formation Mechanisms for Phosphorene and SnIP

Markus R. P. Pielmeier[a] and Tom Nilges[a]

[a]Technical University of Munich, Department for Chemistry, Lichtenbergstraße 4, 85748 Garching bei München, Germany

This project started with the idea to unravel a reason for the racemic mixture in SnIP synthesis and to figure out the vital mechanistic differences compared to the black phosphorus synthesis[23]. Both of them are produced via a short way transport reaction using Sn/SnI_4 and P_{red} and only differ in reaction temperature and the molar ratios of the educts. First, CalPhaD graphs were generated to determine the gas phase compositions for the two temperature regimes and the masses of starting materials, respectively. These diagrams reinforce the results of Utrap et al. stating, the SnIP formation can be accelerated by using SnI_2 as precursor[97]. Furthermore, a visual examination of the ampule during the cooling process hints to an I_2-free atmosphere, also supporting the found mechanism.

The SnIP formation starts from a equimolar ratio (3 $Sn/SnI_4/P_4$) with the most prominent gas phase components P_4 and SnI_2 at around 673 K. After a dimerization of the latter, two dimers arrange in such a way around the phosphorus tetraeder, that parts of the alternating Sn-I chain become visible. The surplus iodine atoms are eliminated simultaneously with the opening of P_4 to a butterfly arrangement. Energetically, this is the most demanding step and then a polymerization of these units can take place. Therefore, one more bond breaking, which can decide the chirality of the finished strand, is needed. Finally, the inner helix is formed and outer helix just follows its lead for the winding direction. The solidification process could influence the chirality of the double helix, if the butterfly substructure is opening when attaching to the bulk material and could potentially entail the racemate of double helices.

During the formation of P_{black} the gas phase composition hardly changes, but the higher temperature and larger quota of P_2 in the CalPhaD at 923 K make a direct attack of SnI_2 on the phosphorus tetraeder reasonable. This breaks two bonds in P_4 directly by inserting Sn and I, which makes it the highest energy point in this reaction pathway. The resulting triangle of phosphorus atoms can form a dimer with itself, yielding a

six-membered ring with two remaining P atom on opposite sides, which are stabilized by two SnI_2 for each atom. This is already the building block for a single phosphorene sheet by substituting a SnI_2 with another one of these P_8 substructures, which can be repeated in all directions in the plane indefinitely. The production of P_{black} crystals can be achieved with this mechanism by layering the expanding sheets above one another.

Author contributions: M. R. P. P. selected suitable starting materials for the quantum mechanical calculations, revised the pathway according to the sensible steps, generated the CalPhaDs and presented all optimizations, graphs and pictures. M. R. P. P. and T. N. were involved in discussing the results as well as writing and revising the manuscript.

Reprinted with permission of *John Wiley and Sons* from *Formation Mechanisms for Phosphorene and SnIP*; Markus R. P. Pielmeier, Tom Nilges; *Angewandte Chemie International Edition*; 60 (12), 6816-6823, **2021**; special permissions are not required for this Open Access Article.

GDCh

Research Articles

Angewandte
Chemie
International Edition

Check for updates

Formation Mechanisms for Phosphorene and SnIP

Markus R. P. Pielmeier and Tom Nilges*

Dedicated to Professor Ulrich Müller on the occasion of his 80th birthday

Abstract: *Phosphorene—the monolayered material of the element allotrope black phosphorus (P_{black})—and SnIP are 2D and 1D semiconductors with intriguing physical properties. P_{black} and SnIP have in common that they can be synthesized via short way transport or mineralization using tin, tin(IV) iodide and amorphous red phosphorus. This top-down approach is the most important access route to phosphorene. The two preparation routes are closely connected and differ mainly in reaction temperature and molar ratios of starting materials. Many speculative intermediates or activator side phases have been postulated especially for top-down P_{black}/phosphorene synthesis, such as Hittorf's phosphorus or $Sn_{24}P_{19.3}I_8$ clathrate. The importance of phosphorus-based 2D and 1D materials for energy conversion, storage, and catalysis inspired us to elucidate the formation mechanisms of these two compounds. Herein, we report on the reaction mechanisms of P_{black}/phosphorene and SnIP from P_4 and SnI_2 via direct gas phase formation.*

Introduction

For many years the research on phosphorous allotropes and compounds has led to fascinating results and has not yet come to an end.[1] Allotropes like red phosphorous have been known for many decades, but they are still controversially discussed in the community while trying to unveil their structure with solid data.[2]

Phosphorene is an important 2D material with many possible applications in modern technology.[3] Fields of application are sensors,[4] field effect transistors (FETs),[5] catalysts for water splitting[6] or hydrogen evolution, and active materials for batteries.[7] Mono- and multilayer phosphorus materials are investigated by quantum chemists and physicists owing to their conformational flexibility[8] (as single sheet), stacking variability and Moiré-driven optical transitions (double and multiple layers).[9] Recently, an extensive theoretical work was published discussing possible conforma-

tions of a single phosphorene sheet, which consist of two chair conformers, a black phosphorus monolayer, a gray arsenic-type (rhombohedral phosphorus or blue phosphorus) and a boat conformer.[8] Phosphorene is often prepared by a top-down approach from black phosphorus (P_{black}), which defines the P_{black} synthesis as a crucial step in phosphorene science. The most feasible top-down approach to phosphorene is delamination of large P_{black} crystals made by the aforementioned synthesis process. In the past few years, bottom-up approaches have emerged and several studies have been performed to identify a possible reaction mechanism for this P_{red}-to-P_{black} gas-phase transformation reaction in CVD processes.[10a,b] In solution, another bottom-up reaction mechanism has been evaluated and investigated, featuring a nucleophilic attack of a free lone pair of ethylenediamine (en) on P_{white} (P_4 molecule)[7a] and P_{red}.[10c] Here, the P_4 entity (P_{white}) is opened to a reactive species, which tends to rearrange into layers of corrugated P_{black} sheets afterwards. Unfortunately, this solution-based synthesis with ethylenediamine leads to P−N bond formation and nitrogen impurities in P_{black}, which has been proven by XPS.[10c] Such impurities, which form in addition to common oxygen impurities caused by oxidation processes in solution and during workup procedures, can affect the performance of P_{black} in applications. Using a gas-phase-based synthesis route, the solvent influence can fully be suppressed and the oxidation problem can be minimized. Also, the crystal quality is generally much higher than for solution-based processes. Therefore, the gas-phase-based synthesis remains the crucial method to grow pure, highly crystalline, large-area crystals of P_{black} for a top-down fabrication of phosphorene.

SnIP, an inorganic double helix material, consists of an outer $[SnI]^+$ and an inner $[P]^-$ helix.[11] Each chiral SnIP double helical strand has a diameter of approx. 1 nm and shows either left- (*M* helix) or right-handed (*P* helix) chirality (Figure 1). Those two different enantiomeric rods appear as a racemic mixture arranged in a pseudo-hexagonal rod-packing along the *a* axis. After SnIP's discovery the preparation process was optimized by varying, for example, temperature profile and reactant ratios, and the stereochemistry as well as stacking variations of chiral double helices in SnIP bulk material were investigated.[12]

Herein, our investigation focuses on the formation mechanisms of the two title compounds. Taking the state-of-the-art knowledge on P_{black} synthesis and its formation into account, as nicely reviewed by Wang et al., it becomes obvious that the formation mechanism is still unknown.[1h] Several compounds, such as other phosphorus allotropes or ternary phases ($Sn_{24}P_{19.3}I_8$),[11c] are postulated as intermediates in the formation process.[1h] It has been shown in an in situ

[*] M. Sc. M. R. P. Pielmeier, Prof. Dr. T. Nilges
Department of Chemistry
Technical University of Munich (TUM)
Lichtenbergstrasse 4, 85748 Garching b. München (Germany)
E-mail: tom.nilges@tum.de

Supporting information and the ORCID identification number(s) for the author(s) of this article can be found under:
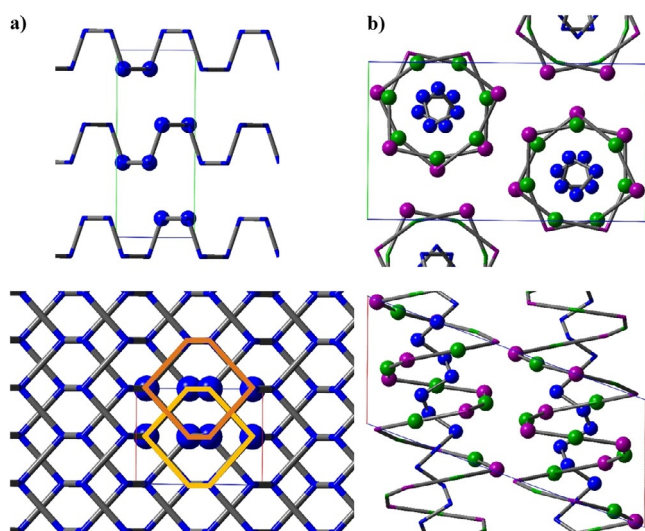https://doi.org/10.1002/anie.202016257.

Figure 1. Crystal structure sections of a) orthorhombic P_{black} and b) double helical SnIP. Top row, projections drawn along the *a*-axis and bottom row along the *b*-axis. Atoms in unit cells are shown as balls, while others are depicted as sticks. Orange hexagons outline AB stacking order for two visible planes.

experiment that P_{black} grows within minutes at temperatures significantly below synthesis temperatures reported earlier and without side phase formation.[3b] In general, such fast formation of P_{black} is very unlikely if intermediates need to be formed first to allow epitaxial growth on it (e.g. clathrate-type $Sn_{24}P_{19.3}I_8$) afterwards. The mere existence of side phases even in close vicinity to the desired product does not necessarily indicate an epitaxial growth mechanism. It has been shown earlier that SnIP decomposes peritectically to the aforementioned clathrate[11b] and it is therefore possible that SnIP may itself act as a precursor to form an intermediate clathrate or P_{black} directly. This speculation is at least feasible and might be another possible reaction pathway to be evaluated. An Sn-I-P intermediate was postulated first in 2016 in the literature[11b] and was discussed thereafter in other publications.[13] In none of the publications a clearly defined species has been identified which may explain the formation of P_{black} from simple materials via the gas phase. To stop speculation, we started a DFT-based investigation to envision formation mechanisms for SnIP at lower and P_{black} at higher temperatures.

Results and Discussion

We applied density functional theory (DFT) to unveil the gas phase formation process of two intriguing materials: P_{black}, an element allotrope of phosphorus, and SnIP, the first inorganic atomic-scale double helix compound (cf. Figure 1). P_{black} represents a precursor to 2D phosphorene, and SnIP is a quasi-1D material consisting of weakly bonded SnIP double helices. Within the framework of DFT we generated and optimized all local minimum structures along the reaction pathways using the Gaussian09 code.[14] Ab initio calculations were performed on GGA level and with the PBE functional.

All relevant DFT data are summarized in the Computational Methods Section in the Supporting Information. The main gas phase species were derived from **Cal**culated **Pha**se **D**iagram (CalPhaD) methods and thermodynamic data were calculated with the tragmin5.1 program suite.[15] In the following, we investigated the energy landscape at different temperatures and found detailed, chemically reasonable and energetically feasible reaction pathways capable of explaining all experimental observations during synthesis. We explored many probable combinations and summarize the most promising pathways in this work.

Despite obvious structural differences, the synthesis procedures for both compounds are rather similar. In both cases tin, Sn^{IV} iodide, and amorphous red phosphorus (P_{red}) act as starting materials.[16] While catalytic amounts of Sn and SnI_4 are necessary to transform P_{red} into P_{black}, equimolar ratios are needed for SnIP. A second important difference is the synthesis temperature window. P_{black} can be synthesized from 923 to 823 K, while SnIP is formed below 673 K. For further details concerning synthesis procedures and structural details, see the Supporting Information.

A detailed mechanism for the gas-phase-based P_{black} synthesis, which includes a quantum chemical investigation with local minima structures along the reaction pathway or alternatively the identification of any intermediate along the reaction pathway, is lacking. So far, only assumptions, such as the occurrence of epitaxial growth of P_{black} on $Sn_{24}Sn_{19.3}I_8$ or the formation of other phosphorus allotropes as precursor states, are used to explain or interpret the formation of P_{black}.

In a first evaluation step, we calculated the gas phase species to occur in the Sn/SnI_4-based synthesis of P_{black} and SnIP by CalPhaD methods. The latter is a powerful tool to investigate gas phase transport reactions.[17] We repeated CalPhaD calculations for P_{black}, substantiating the results reported by Lange et al. in 2007 (see Figure 2a),[16] and derived new ones for SnIP (Figure 2b). In both cases the dominating gas phase species with significant partial pressures are P_4 (**1**) and SnI_2 (**2**), while SnI_4 (**3**), I_2 (**4**), or P_2 does not exhibit mentionable presence. SnI_2 (green curves) and P_4 (black curves) partial pressures (Figure 2) are at least 3 orders of magnitude higher than any competing molecules in equilibrium. I_2 partial pressures are very low in both cases, even in the SnIP synthesis, where significant (equimolar) amounts of SnI_4 (**3**) are present, which possibly acts as an iodide source. It is therefore likely that the two main components **1** and **2** play a crucial role in the formation of both compounds. The decisive role of **1** was already proven in the phosphorene synthesis by Köpf in 2014 by in situ experiments.[3b] In all cases we reach saturation vapor pressures, represented by almost horizontal curves for **1** and **2** in Figure 2, prior to the applied maximum reaction temperatures (illustrated by dashed lines in Figure 2). During P_{black} synthesis (which starts at 923 K and continues during cooling) the P_4 saturation pressure remains present over a long temperature range from 923 to approx. 740 K. This feature is beneficial for the fast growth of P_{black}, which occurs within minutes in a temperature range from 773 to 673 K.[3b]

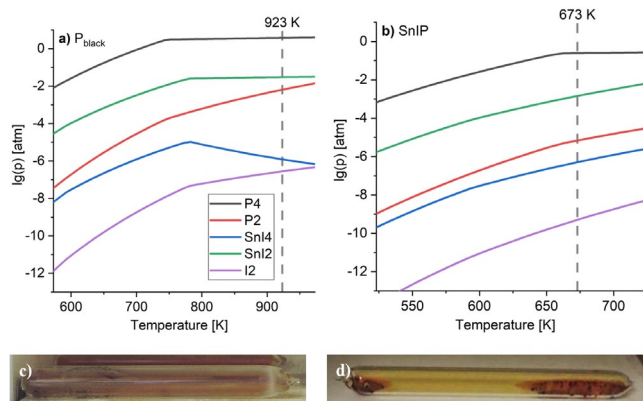In order to verify the results of our CalPhaD calculations we investigated the ampoules under synthesis conditions by

Figure 2. a) Partial pressure diagram featuring the corresponding equilibrium gas phase pressure during P_{black} synthesis in the temperature range from 600 to 950 K. b) Partial pressure diagram for SnIP from 500 to 750 K. Partial pressures are plotted on a logarithmic scale. The dashed lines show the maximum synthesis temperature (T_{max}) applied for each case. Silica glass ampoules in the oven during synthesis at c) $T_{max} = 923$ K (P_{black}) and d) $T_{max} = 673$ K (SnIP). Sn (boiling point approx. 2600°C) has no significant partial pressure in the given temperature range.
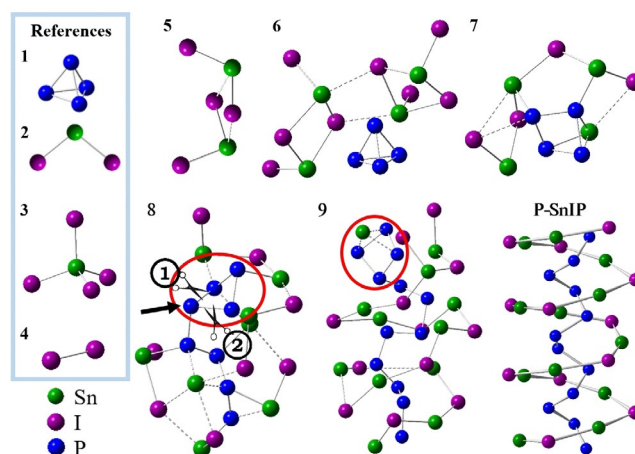

Figure 3. Local minimum structures along the reaction pathway to SnIP. Important starting materials (**1**, **2**) and a Sn_2I_4 dimer **5** are necessary to initiate SnIP formation. **3** and **4** are neglected due to chemical considerations and observations. P_4 activation takes place in **6**→**7**. **8** is a dimer of **7** in which the Sn_2I_4 units are opposed to each other. The phosphorous butterfly in the red circle can be opened by breaking bond 1 or 2. **9** points out that the addition of **7** can be repeated. The P-SnIP helix illustrates the corresponding part of the crystal structure of SnIP comparable to **9**. *P*-SnIP represents a right-handed double-helix strand.

opening the ovens at its respective reaction temperatures (see Figure 2 c,d; videos given in Supporting Information Note 1). We observed a light orange gas atmosphere and condensation of **2** during P_{black} synthesis (**2** shows an evaporation rate of 127 mg h^{-1} at 623 K and ambient pressure[18]) but no hints for **4** at both reaction temperatures. **4** is obviously not present and can therefore not contribute to any reaction mechanism. In gas phase balance and mass spectrometry experiments during P_{black} and $As_{0.83}P_{0.17,black}$ experiments only metal diiodide, Pn_4, and Pn_2 fragments (Pn = P, As) were identified as main gas phase species.[16,1k]

With this important information taken into account, the mechanisms for phosphorene and SnIP can now be deduced with P_4 (**1**) and SnI_2 (**2**) as starting materials (Figure 3).

It should be noted that the suggested two mechanisms are in accordance with our experimental findings, but other energetically favorable ones may exist. All molecules discussed in the following mechanisms are fully optimized and converged structures which represent a local minimum on their energy landscapes.

First, we investigate the formation of SnIP from equimolar ratios of the starting materials $3Sn/SnI_4/P_4$. Starting with the main components P_4 (**1**), SnI_2 (**2**) and neglecting the minor ones SnI_4 (**3**) and I_2 (**4**), we identified a dimerization of two SnI_2 molecules to Sn_2I_4 (**5**) as the first reaction step. A direct reaction of **1** with **2** as well as the dimer molecule **5** is investigated and leads to two different reaction pathways (Figures 3 and 5, see below). Unfortunately, no thermodynamic data are available for **5** to compare it to all other species in the partial pressure diagrams (Figure 2).

The proposed SnIP mechanism starts with the dimerization of **2** to **5**, which arranges itself in proximity to **1** (cf. Figure 3). Together with a second molecule of **5** the next local minimum structure $2Sn_2I_4@P_4$ (**6**) forms. In **6**, first Sn–I bond formation takes place towards [SnI]$^+$ chains as two **5** approach each other in a way that leads to alternating Sn/I

atoms along the dashed lines in **6**. The coordination of **1** with two entities of **5** to **6** is electronically favored by $\Delta E_{tot} = -208$ kJ mol^{-1}. In this step, due to entropy reasons, the high availability of SnI_2 in the gas phase and taking kinetic considerations into account, the formation of dimer **5** is favored. It must be stated at this point that we also performed calculations with SnI_2 monomers instead of **5** dimers coordinating **1**, but such models led to P_{black} formation (see below). Only with a dimer formation of two molecules of **2** to **5** we succeeded in reaching the desired final product SnIP.

In $Sn_4I_4@P_4$ (**7**) the elimination of four iodine atoms from **6** initiates a structural rearrangement in the outer sphere combined with a P–P bond opening towards a butterfly arrangement in the P_4 molecule (**1**). This is the energetically most demanding step in the proposed reaction mechanism, with $\Delta E_{tot} = +324$ kJ mol^{-1}.

5 ($\Delta E_{tot} = -83$ kJ mol^{-1}) can be obtained as *cis* or *trans* isomer (cf. Figure 4). The *cis/trans* isomerism and abstraction of iodine atoms, which is essential for achieving the final ratio (Sn/I/P = 1:1:1), needs further attention. We identified the *cis* isomer of **5** as the most favorable species to coordinate with **1** as stated in Figure 3, step **6**. The preference of the *cis* over the *trans* isomer is due to the following reasons: a) the steric hindrance during formation of **6** by two **5** is much lower; and b) the two lone pairs of **2** can attract two iodine atoms in *cis*-**5** in such a way that a six-membered local minimum state is formed. This process allows effective abstraction of four iodine atoms in the Sn–I substructure of **6** by two molecules of **2** (see Figure 4).

Following such a reaction pathway, the formation of iodine (**4**) is avoided, which is consistent with our observation during synthesis [cf. Supporting Information Note 1 and Eq. (1)].
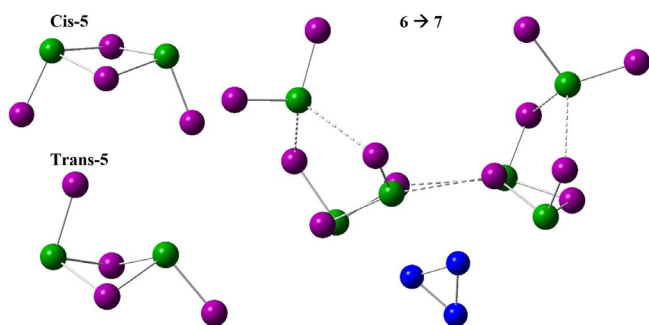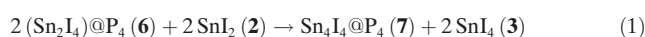
Figure 4. Sn_2I_4 molecules (**5**) in *cis* and *trans* configuration. Reaction Scheme for a **6**→**7** reaction pathway. Two SnI_2 (**2**) attract two *cis*-**5** entities in $2Sn_2I_4@P_4$ (**6**) during bond formation in the Sn—I substructure. In a next step, SnI_4 (**3**) will emerge during $Sn_4I_4@P_4$ (**7**) formation. I (purple), Sn (green), and P (blue) spheres. A P atom of P_4 is covered.

$$2\,(Sn_2I_4)@P_4\,(\mathbf{6}) + 2\,SnI_2\,(\mathbf{2}) \rightarrow Sn_4I_4@P_4\,(\mathbf{7}) + 2\,SnI_4\,(\mathbf{3}) \qquad (1)$$

Another, less-likely **6**→**7** reaction pathway step may involve the intermediate formation of iodine (**4**). Taking this assumption into account, additional **2** is not needed and **4** is formed simultaneously during formation of **7**. We assume that **4** must instantaneously be consumed by an oxidation reaction of elemental Sn to SnI_2 according to Equation (2).

$$Sn + I_2\,(\mathbf{4}) \rightarrow SnI_2\,(\mathbf{2}) \qquad (2)$$
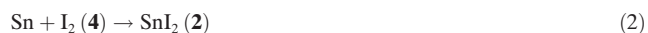
Dependent on the kinetics of such a reaction, an intermediate formation of **4** should lead to visible amounts of **4** during synthesis, which is obviously not the case.

Another observation may help to substantiate the proposed first **6**→**7** reaction pathway mechanism. As stated earlier in this manuscript, Sn and SnI_4 are used as starting materials for the synthesis of SnIP. It was also reported that SnI_2 will be formed in a slow comproportionation reaction with a reasonable reaction rate above 633 K.[19] This temperature is only slightly lower than $T_{max} = 673$ K applied in the SnIP synthesis (see Figure 2). If an equimolar $2Sn/2SnI_2/P_4$ mixture of starting materials is used instead of $3Sn/SnI_4/P_4$ where SnI_2 (**2**) is available directly, one can observe an optimized formation of SnIP. Much larger crystals and less starting material residues occur.[11a] The beneficial usage of preformed SnI_2 substantiates our proposed mechanism as shown in Figures 3 and 4 and underlines the importance of formation or presence of **2** during the SnIP synthesis.

To complete SnIP formation, two molecules of **7** need to arrange in such a way that two P_4 butterflies are in close proximity, enabling bond formation in the phosphorus substructure. Bond formation in the $[SnI]^+$ substructure and in the $[P]^-$ substructure during step **7**→**8** are energetically less demanding processes than the P_4 activation process in step **6**→**7**. We gain 103.3 kJ mol^{-1} compared to the aforementioned reaction step. A fully open P chain fragment is formed during this reaction step in $Sn_8I_8@P_8$ (**8**) enabling the inner P helix formation. In a quasi-polymerization reaction another molecule **7** reacts with **8** to larger units.

SnIP consists of two enantiomeric double helical forms, a left-handed *M* and a right-handed *P* double helix.[20] The stereochemistry of the inner $[P]^-$ chain is determined in **8**, dependent on the way the butterfly P_4 ring is opened. In **8** the three-bonded P atom (marked with an arrow in Figure 3) is attached to two other P atoms in the butterfly. Dependent on which bond (1 or 2, marked by scissors in Figure 3) is broken, a *M* or *P* double helix results, respectively. The outer $[SnI]^+$ helix seems to follow the presetting of the inner helix. This suggested mechanism can explain the racemic nature present in the final product where equal amounts of *M* and *P* helices are present.[11b]

Finally, the double helix formation starts in **9**, optimizing the overall bonding situation towards the favored double helix arrangement in the final product (the final structure is given in Figure 1). A total energy Scheme is illustrated in Figure 6. Overall, the formation of SnIP is favored by $\Delta E_{tot} = -26$ kJ mol^{-1} related to the starting materials.

Additional information and DFT data concerning all local minima structures **5** to **9** are summarized in Supporting Information Note 2.

In general, the P_{black} synthesis is performed at higher temperatures than the SnIP one. The phosphorene formation (single sheet formation) starts with the activation of **1** by a single SnI_2 (**2**) molecule (cf. Figure 5). When a tin atom first inserts into one of the P—P bonds, an iodine atom attaches to a neighboring phosphorus atom. Subsequently, **10** consists of two triangles above each other, an almost unchanged P_3 unit and a Sn-I-P unit with the remaining residual iodide coordinated to the tin atom. This local minimum **10** represents the highest energy point on the entire reaction pathway (+ 76 kJ mol^{-1}). **10** can react with another molecule **2** forming a highly symmetric $2(SnI_2)P_4$ local minimum structure (not shown in Figure 5), which is not able to dimerize further. In **11** the first P—P bonds are formed while SnI_2 is fragmented totally in $[SnI]^+$ and I^-.
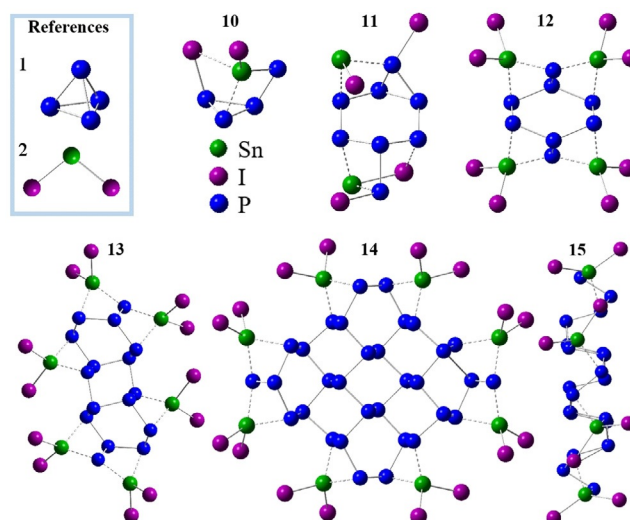

Figure 5. Starting materials (**1**, **2**) and geometry-optimized structures **10** to **15** in the proposed phosphorene mechanism. **14** and **15** are two different views on the same structure. In **14/15** four SnI_2 coordinate with two-bonded phosphorus in a highly symmetric way.

After this first dimerization step, **11** is stabilized by the addition of two additional SnI_2 molecules (**2**), yielding **12**. With this step, we created a primary essential building block for the phosphorene sheet, the corrugated six-membered ring in a chair conformation. On all ridges, single-bonded P atoms with a formal charge of 2− are coordinated by two Sn from both sides while two-bonded P are mono-coordinated with one **2**. Homo-atomically three-bonded phosphorus atoms exactly represent the bonding situation in an ideal phosphorene sheet. Following the same coordination and bond formation principle, two molecules of **12** can be merged to form **13**. Growth of the phosphorene sheet can now happen in any direction by adding additional **12** molecules to **13** or dimerization of **13**. In each case mentioned so far, SnI_2 (**2**) is replaced at the ridges where P−P bond formation occurs. For exampmle, in **14**, a dimerization of **13** took place and four **2** were removed. **15** represents a side view of **14** where the conformation of the P_{black}-related phosphorene layer becomes evident. The growth of a large-area phosphorene sheet might be possible without bulk P_{black} formation if the attachment of multiple phosphorene sheets is hindered by entities weakly coordinating the remaining lone pairs.

According to our 0 K calculations the formation of P_{black} (composed by phosphorene layers) is strongly favored ($\Delta E(\mathbf{14}) = -1040 \text{ kJ mol}^{-1}$) and a comparatively small energy portion is needed to form **10** from **1/2**. A full total energy Scheme is given in Figure 6 and DFT data are summarized in Supporting Information Note 2.

In both reaction cascades, the most energy-demanding step is to activate and break the first P−P bond in the P_4 tetrahedron. This step occurs at different points in the reaction cascade, in step **6** to **7** for SnIP and during step **1/2** to **10** in the case of P_{black}. The most obvious difference for both mechanisms is the initiation of a P−P bond activation. In the SnIP case, two dimerized Sn_2I_4 molecules are needed to coordinate the P_4 tetrahedron, followed by a concurrent bond opening and double iodide elimination [cf. Eq. (2)] to realize the reactive butterfly P_4 configuration. The dimerization is energetically favored in our calculations by approx. 200 kJ mol^{-1} (**1/2** to **6**). For phosphorene formation at higher temperatures (cooling gradient applied from 923 to 823 K during P_{black} synthesis)[3b] the P_4 activation ($\Delta E_{tot} = +76 \text{ kJ mol}^{-1}$, from **1/2** to **10**) occurs via a monomeric SnI_2 molecule (**2**) and by direct insertion into a P−P bond.

While the SnI_2 (**2**) partial pressure at 673 K, being the synthesis temperature of SnIP (see Figure 2), is comparable to the partial pressure for the P_{black} case (ca. 10^{-3} atm), the dimer formation of **5** should be favored at this temperature and disfavored at higher P_{black} synthesis temperatures.

The role of iodine and metal halides for the formation of phosphorene/P_{black} was subject to intensive research in the past few years.[21] Effective bulk P_{black} formation was observed if tin and iodine species were present as starting materials independent of the source. For almost any synthesis in which SnI_2 formation from a metal iodide and tin in elemental or intermetallic form was possible, the authors observed P_{black} formation. Besides SnI_2, the heavier homologue PbI_2 can act as a less active species for P_{black} formation, but it has a high activity and selectivity in the formation of black arsenic–phosphorus $As_{0.83}P_{0.17}$.[22] $As_{0.83}P_{0.17}$ crystallizes in the P_{black} structure type.

To elucidate these reaction mechanisms in more detail and to address a situation as close as possible to conditions during synthesis, we performed a DFT analysis at different temperatures and pressures.

From Barlow's law, the bursting pressure of our silica glass ampoules was deduced to be 100 bar (ca. 99 atm), but with the safety factor of 1.5, a maximum working pressure of 66 atm can be hypothesized (cf. Supporting Information Note 3).[23] It is also known that the formation takes place during slow cooling starting from maximum temperature for both compounds. Following this train of thought, the assumption of 50 atm seems reasonable while looking at different temperatures. Gibbs free energies (G) were calculated for every step mentioned above Figure 6 and the results for $\Delta G(p,T)$ with $p = 50$ atm are summarized in Figure 7.

We want to point out that for both pathways entropy (calculated by the partition function according Supporting Information Note 4) becomes more dominant the further one moves along the reaction coordinate.

In case of SnIP (Figure 7a), the dimer formation of **5** is still slightly exothermic at 673 K, which represents the maximum temperature in the synthesis process. Obviously, the dimerization of SnI_2 (**2**) to Sn_2I_4 (**5**) is a spontaneous process and thermodynamically favored at synthesis conditions. At higher temperatures (approaching P_{black} synthesis conditions) ΔG becomes positive. Even the attachment of **5** to
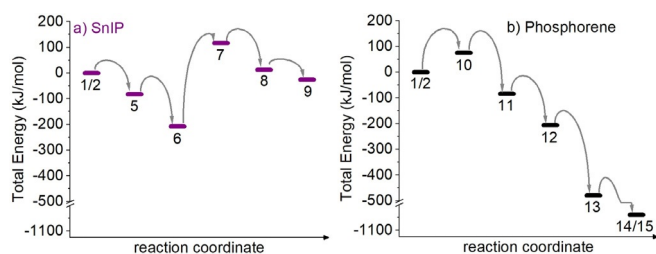

Figure 6. Consecutive reaction steps on the corresponding total energy scale (0 K) for a) SnIP and b) phosphorene. The numbering links each step to the structures in Figures 3 and 4. The arrows are used to clarify the succession and are not related to the actual barriers between the steps.

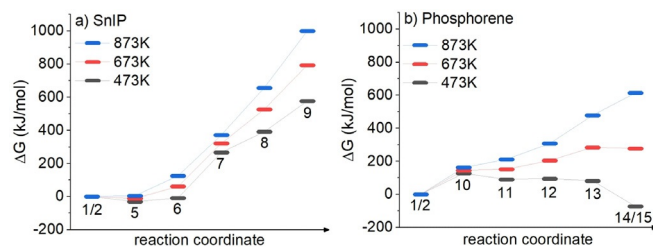**Figure 7.** Reaction pathways with $\Delta G(p,T)$ for a) SnIP and b) phosphorene calculated at three different temperatures ($T = 473$ K, 573 K, or 673 K). In all cases, pressure was set to 50 atm and Gibbs energies were referenced to the starting materials **1** and **2**. The lines between the local minima are drawn to guide the eyes and DFT data are summarized in Supporting Information Note 5.

P_4 (**1**) shows negative ΔG values at low temperatures, which indicates a certain driving force towards the dimer-driven activation of **1**. After the activation and bond breaking in **1**, each following step shows positive Gibb's free enthalpies up to significant, high values at 873 K; but at the lowest examined temperature of 473 K the Gibb's free enthalpy is halved from the one at 873 K, which indicates a more feasible formation tendency at lower temperatures. This feature is consistent with our observations that SnIP cannot be prepared at higher temperatures than 673 K. It needs to be stated at this point that SnIP decomposes peritectically at 740 K to $Sn_{24}P_{19.3}I_8$, which is the thermodynamically stable phase under these conditions. Therefore, at 873 K all SnIP data need to be interpreted with care or, in other words, it is most likely that SnIP cannot be formed at such high temperatures. Going back to the synthesis of SnIP, the starting materials are cooled down from 673 K with a rate of $5\,K\,h^{-1}$, which means the optimal reaction conditions are met somewhere between 673 K (Figure 7a, red lines) and 473 K (Figure 7a, black lines) from an experimental point of view. The calculated free energies for the formation of **9** are 576 kJ mol^{-1} at 473 K and 793 kJ mol^{-1} at 673 K. In a previous work the electronic energy contribution at 0 K for seven agglomerating SnIP double helices was found to be 879 kJ mol^{-1} already.[12b] Therefore, one can expect that lattice energy can compensate the positive formation energies calculated in this study.

The Gibbs free energy profile for the phosphorene formation mechanism across the different reaction steps is different in the case of P_{black} (Figure 7b). The first P_4 activation step **1/2** to **10** is the crucial one in the entire reaction cascade. This finding is equivalent to the previously discussed SnIP mechanism, where the dimerization of two SnI_2 molecules is favored at low temperatures in the vicinity of **1** during P−P bond activation. Obviously, the P−P bond activation and insertion of a single SnI_2 molecule into a P−P bond is the most energy-demanding step at elevated temperatures. This feature, taken from our 0 K calculations, is also valid at 473 K. If the temperature is raised further the following steps in the reaction cascade become more and more endergonic. At 673 K we derived a ΔG of 278 kJ mol^{-1} and at 873 K of 613 kJ mol^{-1} from our DFT data for the last reaction step **14/15**. A huge lattice energy contribution is needed to form P_{black} in the end. This seems to be the case because bulk P_{black} is formed in a temperature interval of 923 to 823 K upon slow cooling.[3b] We see a clear trend towards less positive and even negative ΔG upon reducing the temperature in our calculations. Somewhere between 673 and 473 K ΔG becomes negative for the last reaction step. This trend can perfectly explain the effective and rapid growth rate of P_{black} found between 773 and 673 K (and applying a temperature cooling rate of $100\,K\,h^{-1}$) in an in situ neutron diffraction experiment,[3b] in particular if the lattice energy gain during crystallization is also taken into account. Additional information concerning the in situ neutron experiment is given in the Supporting Information.

Conclusion

The formation mechanisms of phosphorene, a monolayer unit of P_{black}, and SnIP, a double helical inorganic semiconductor, were investigated in the framework of DFT. Both compounds can be prepared at different temperatures by a gas phase reaction with phosphorus, Sn, and SnI_4 as starting materials. While bulk P_{black} is formed at elevated temperatures and quasi-catalytic amounts of SnI_2, the formation of SnIP takes place at lower temperatures and equimolar ratios of all necessary elements. In a first step, CalPhaD methods were successfully used to identify the main gas phase species during both syntheses: P_4 and SnI_2. The latter is formed by a comproportionation reaction of Sn and SnI_4 above 633 K and represents the active gas phase species in both reactions. Iodine formation was fully ruled out by in situ observation during synthesis and our CalPhaD results.

Both reaction mechanisms were illustrated by total energy calculations at 0 K with geometry-optimized local minimum structures. In each case, P_4 activation is the most energy demanding reaction step. A Sn_2I_4 dimer is crucial in the SnIP reaction cascade to activate the P_4 molecule while a direct insertion of SnI_2 into a P−P bond of P_4 takes place during P_{black} synthesis. Low temperatures and high SnI_2 availability (due to the equimolar ratio of starting materials) in the SnIP case allows effective Sn_2I_4 dimer formation whereas such dimers are not stable (and present) at higher temperatures during P_{black} formation. As a direct consequence, the beneficial usage of SnI_2 as a starting material for optimized SnIP synthesis becomes obvious. Also, the previously reported favorable P_{black} synthesis in presence of Sn/I sources is a straightforward result of our proposed mechanism. In each case where catalytic amounts of SnI_2 can be realized during synthesis, an effective formation of P_{black} was found.

Gibbs free energy calculations were performed at elevated temperatures of 473, 673, and 873 K and a pressure of 50 atm in order to gain substantial information about the two reaction processes as close as possible to the applied synthesis conditions. Even at the SnIP synthesis temperature of 673 K the Sn_2I_4 dimer formation is energetically and thermodynamically favored, which corroborates our 0 K calculations. While all SnIP reaction steps are energetically demanding along the reaction pathway, the situation is slightly different for phosphorene. The more the temperature is lowered the more favorable the formation of phosphorene becomes. At the lowest temperature in our calculations, at 473 K, the growth of phosphorene in lateral dimensions shows negative ΔG values, which illustrate the thermodynamic stability of phosphorene sheets under these conditions. A very fast growth of P_{black} observed during a neutron diffraction experiment between 773 and 673 K—more than 150 K lower than the synthesis temperature itself—can perfectly be explained by our results.

CVD processes are an important technique to deposit material in thin films. With the knowledge of the formation mechanisms for SnIP, P_{black}, and phosphorene, such important one- and two-dimensional materials might be effectively deposited on substrates in the future. Based on this knowledge, CVD processes can be adjusted and optimized aiming

for crystalline and maybe oriented materials on various substrates.

Acknowledgements

Conflict of interest

The authors declare no conflict of interest.

Keywords: ab initio calculations · black phosphorus/ phosphorene · materials science · reaction mechanism · SnIP double helix material

[1] a) F. Bachhuber, J. von Appen, R. Dronskowski, P. Schmidt, T. Nilges, A. Pfitzner, R. Weihrich, *Z. Kristallogr. Cryst. Mater.* **2015**, *230*, 107–115; b) F. Bachhuber, J. von Appen, R. Dronskowski, P. Schmidt, T. Nilges, A. Pfitzner, R. Weihrich, *Angew. Chem. Int. Ed.* **2014**, *53*, 11629–11633; *Angew. Chem.* **2014**, *126*, 11813–11817; c) P. W. Bridgman, *J. Am. Chem. Soc.* **1914**, *36*, 1344–1363; d) P. W. Bridgman, *J. Am. Chem. Soc.* **1916**, *38*, 609–612; e) A. Castellanos-Gomez, L. Vicarelli, E. Prada, J. O. Island, K. L. Narasimha-Acharya, S. I. Blanter, D. J. Groenendijk, M. Buscema, G. A. Steele, J. V. Alvarez, H. W. Zandbergen, J. J. Palacios, H. S. J. van der Zant, *2D Mater.* **2014**, *1*, 025001; f) M. Hart, E. R. White, J. Chen, C. M. McGilvery, C. J. Pickard, A. Michaelides, A. Sella, M. S. P. Shaffer, C. G. Salzmann, *Angew. Chem. Int. Ed.* **2017**, *56*, 8144–8148; *Angew. Chem.* **2017**, *129*, 8256–8260; g) G. Sansone, L. Maschio, A. J. Karttunen, *Chem. Eur. J.* **2017**, *23*, 15884–15888; h) D. Wang, P. Yi, L. Wang, L. Zhang, H. Li, M. Lu, X. Xie, L. Huang, W. Huang, *Front. Chem.* **2019**, *7*, 21; i) Y. Liu, Q. Liu, C. Jian, A. Zhang, M. Chen, Z. Li, T. Li, T. Nilges, K. He, Z. Jia, C. Zhou, *Nat. Commun.* **2020**, *11*, 2520; j) J. Zhang, C. Fu, S. Song, H. Du, D. Zhao, H. Huang, L. Zhang, J. Guan, Y. Zhang, X. Zhao, C. Ma, C.-L- Jia, D. Tománek, *Nano Lett.* **2020**, *20*, 1280–1285; k) O. Osters, T. Nilges, F. Bachhuber, F. Pielnhofer, R. Weihrich, M. Schöneich, P. Schmidt, *Angew. Chem. Int. Ed.* **2012**, *51*, 2994–2997; *Angew. Chem.* **2012**, *124*, 3049–3052.

[2] S. Zhang, H.-J. Qian, Z. Liu, H. Ju, Z.-Y. Lu, H. Zhang, L. Chi, S. Cui, *Angew. Chem. Int. Ed.* **2019**, *58*, 1659–1663; *Angew. Chem.* **2019**, *131*, 1673–1677.

[3] a) H. Liu, A. T. Neal, Z. Zhu, Z. Luo, X. Xu, D. Tománek, P. D. Ye, *ACS Nano* **2014**, *8*, 4033–4041; b) M. Köpf, N. Eckstein, D. Pfister, C. Grotz, I. Krüger, M. Greiwe, T. Hansen, H. Kohlmann, T. Nilges, *J. Cryst. Growth* **2014**, *405*, 6–10.

[4] a) M. Engel, M. Steiner, P. Avouris, *Nano Lett.* **2014**, *14*, 6414–6417; b) Q. Guo, A. Pospischil, M. Bhuiyan, H. Jiang, H. Tian, D. Farmer, B. Deng, C. Li, S.-J. Han, H. Wang, Q. Xia, T.-P. Ma, T. Müller, F. Xia, *Nano Lett.* **2016**, *16*, 4648–4655; c) L. Kou, T. Frauenheim, C. Chen, *J. Phys. Chem. Lett.* **2014**, *5*, 2675–2681.

[5] a) S. Das, M. Demarteau, A. Roelofs, *ACS Nano* **2014**, *8*, 11730– 11738; b) L. Li, Y. Yu, G. J. Ye, Q. Ge, X. Ou, H. Wu, D. Feng,

X. H. Chen, Y. Zhang, *Nat. Nanotechnol.* **2014**, *9*, 372–377; c) Z. Yang, J. Hao, S. Yuan, S. Lin, H. M. Yau, J. Dai, S. P. Lau, *Adv. Mater.* **2015**, *27*, 3748–3754; d) W. Zhu, M. N. Yogeesh, S. Yang, S. H. Aldave, J.-S. Kim, S. Sonde, L. Tao, N. Lu, D. Akinwande, *Nano Lett.* **2015**, *15*, 1883–1890.

[6] a) T. H. Lee, S. Y. Kim, H. W. Jang, *Nanomater.* **2016**, *6*, 194; b) J. Liu, *J. Alloys Compd.* **2016**, *672*, 271–276; c) C. Ott, F. Reiter, M. Baumgartner, M. Pielmeier, A. Vogel, P. Walke, S. Burger, M. Ehrenreich, G. Kieslich, D. Daisenberger, J. Armstrong, U. K. Thakur, P. Kumar, S. Chen, D. Donadio, L. S. Walter, R. T. Weitz, K. Shankar, T. Nilges, *Adv. Funct. Mater.* **2019**, *29*, 1900233; d) E. Üzer, P. Kumar, R. Kisslinger, P. Kar, U. K. Thakur, K. Shankar, T. Nilges, *Nanoscale Adv.* **2019**, *1*, 2881– 2890.

[7] a) B. Tian, B. Tian, B. Smith, M. C. Scott, Q. Lei, R. Hua, Y. Tian, Y. Liu, *Proc. Natl. Acad. Sci. USA* **2018**, *115*, 4345–4350; b) W. Li, Y. Yang, G. Zhang, Y.-W. Zhang, *Nano Lett.* **2015**, *15*, 1691– 1697.

[8] J. Guan, Z. Zhu, D. Tománek, *ACS Nano* **2014**, *8*, 12763–12768.

[9] S. Zhao, E. Wang, E. A. Üzer, S. Guo, K. Watanabe, T. Taniguchi, T. Nilges, Y. Zhang, B. Liu, X. Zou, F. Wang, *arXiv* https://arxiv.org/abs/1912.03644v1.

[10] CVD and Vapor deposition: a) C. Li, Y. Wu, B. Deng, Y. Xie, Q. Guo, S. Yuan, X. Chen, M. Bhuiyan, Z. Wu, K. Watanabe, T. Taniguchi, H. Wang, J. J. Cha, M. Snure, Y. Fei, F. Xia, *Adv. Mater.* **2018**, *30*, 1703748; b) J. B. Smith, D. Hagaman, H.-F. Ji, *Nanotechnology* **2016**, *27*, 215602; c) Y. Wang, M. He, S. Ma, C. Yang, M. Yu, G. Yin, P. Zuo, *J. Phys. Chem. Lett.* **2020**, *11*, 2708– 2716.

[11] a) T. Nilges, D. Pfister, C. Ott, K. Schäfer, M. Baumgartner, R. Weihrich (TUM) EP 3 319 903 B1, **2015**; b) D. Pfister, K. Schäfer, C. Ott, B. Gerke, R. Pöttgen, O. Janka, M. Baumgartner, A. Efimova, A. Hohmann, P. Schmidt, S. Venkatachalam, L. van Wüllen, U. Schürmann, L. Kienle, V. Duppel, E. Parzinger, B. Miller, J. Becker, A. Holleitner, R. Weihrich, T. Nilges, *Adv. Mater.* **2016**, *28*, 9783–9791; c) M. Shatruk, K. A. Kovnir, A. V. Shevelkov, I. A. Presniakov, B. A. Popovkin, *Inorg. Chem.* **1999**, *38*, 3455.

[12] a) A. X. Utrap, N. Y. Xiang, T. Nilges, *J. Cryst. Growth* **2017**, *475*, 341–345; b) M. R. P. Pielmeier, A. J. Karttunen, T. Nilges, *J. Phys. Chem. C* **2020**, *124*, 13338–13347.

[13] a) F. Baumer, F. Reiter, T. Nilges, *Z. Anorg. Allg. Chem.* **2017**, *643*, 1444–1450; b) S. Li, X. Liu, X. Fan, Y. Ni, J. Miracle, N. Theodoropoulou, J. Sun, S. Chen, B. Lv, Q. Yu, *Cryst. Growth Des.* **2017**, *17*, 6579–6585.

[14] a) M. J. Frisch, G. W. Trucks, H. B. Schlegel, G. E. Scuseria, M. A. Robb, J. R. Cheeseman, G. Scalmani, V. Barone, G. A. Petersson, H. Nakatsuji, X. Li, M. Caricato, A. V. Marenich, J. Bloino, *Gaussian 09, Revision E.01*, Gaussian Inc. : Wallingford CT, **2013**; b) J. P. Perdew, K. Burke, M. Ernzerhof, *Phys. Rev. Lett.* **1996**, *77*, 3865–3868; c) T. H. Dunning, *J. Chem. Phys.* **1977**, *66*, 1382–1383; d) G. Igel-Mann, H. Stoll, H. Preuss, *Mol. Phys.* **1988**, *65*, 1321–1328; e) R. Dennington, T. Keith, J. Millam, GaussView Version 5, **2013**.

[15] GMIN Version 5.1, Package TRAGMIN for Calculation of Thermodynamic Equilibrium, www.tragmin.de (accessed: September 2020).

[16] S. Lange, P. Schmidt, T. Nilges, *Inorg. Chem.* **2007**, *46*, 4028– 4035.

[17] B. Sundman, Q. Chen, Y. Du, *J. Phase Equilib. Diffus.* **2018**, *39*, 678–693.

[18] J. Jiang, F. Heck, D. M. Hofmann, M. Eickhoff, *Phys. Status Solidi B* **2018**, *255*, 1700426.

[19] W. Reinders, S. de Lange, *Z. Anorg. Allg. Chem.* **1912**, *79*, 230– 238.

[20] U. Müller, *Acta Crystallogr. Sect. B* **2017**, *73*, 443–452.

[21] M. Zhao, X. Niu, L. Guan, H. Qian, W. Wang, J. Sha, Y. Wang, *CrystEngComm* **2016**, *18*, 7737.

[22] B. Liu, M. Köpf, A. N. Abbas, X. Wang, Q. Guo, Y. Jia, F. Xia, R. Weihrich, F. Bachhuber, F. Pielnhofer, H. Wang, R. Dhall, S. B. Cronin, M. Ge, X. Fang, T. Nilges, C. Zhou, *Adv. Mater.* **2015**, *27*, 4423–4429.

[23] a) Seamless steel tubes for oil- and water-hydraulic systems—Calculation rules for pipes and elbows for dynamic loads. DIN 2413:2020-04: Deutsches Institut für Normung e.V.; b) Fused silica knowledge base. Heraeus Holding GmbH: https://www.heraeus.com/en/hca/fused silica quartz knowledge base 1/properties 1/properties hca.html#tabs-608478-6.

Supporting Information

Formation Mechanisms for Phosphorene and SnIP

Markus R. P. Pielmeier and Tom Nilges*

anie_202016257_sm_miscellaneous_information.pdf
anie_202016257_sm_Pblack923.mp4
anie_202016257_sm_SnIP673.mp4

Supplement

*

Computational Methods [14]

Ab initio calculations are carried out using the Gaussian09 code and its default settings unless noted otherwise. All optimizations and frequency calculations are performed on the DFT-GGA-level with the functional from Perdew, Burke and Ernzerhof (PBE). For basis sets the Gaussian09 integrated SDD setting was chosen. This means for phosphorus the Dunning full double zeta basis set[36] was used, while for tin and iodine polarizable effective core pseudopotential (ECP) basis sets[37] were applied. The thermodynamic data was generated with the Gaussian09 thermochemistry analysis tool starting from the corresponding local minimum. All relevant data are deposited as files (cf. Note 2 and Note 5)

Structure models illustrated in this paper were generated with the GaussView5 visualization tool. The default value of 75% of vdW radii is shown on all figures for all atoms except in wireframe representation.

The gas phase composition was calculated with the tragmin5.1 code and its default thermodynamic constants in the respective temperature regimes.[15] 3 solid phases derived from our

experiments and 5 gas phase species were used as input parameters. More detailed data and parameters concerning the gas phase evaluations are summarized in the Supplement Note 5.

Black phosphorus and SnIP Syntheses

Despite obvious structural differences, the synthesis procedures for both compounds are rather similar. In both cases tin, Sn-(IV)-iodide and amorphous red phosphorus (P_{red}) act as starting materials. In the case of P_{black} catalytic amounts of Sn and SnI_4 are used to form P_{black} from P_{red} via a short way transport reaction. Bulk P_{black} can be grown in a temperature range from 923 K to 823 K with a cooling rate of 13.3 K/h.[3b] In an in situ neutron diffraction experiment Pblack showed a reasonable growth rate even at lower temperatures. Within 75 minutes, P_{black} grew to large crystals with edge lengths up to 0.5 cm in evacuated silica ampoules.[3b] During this experiment, a temperature window of 773 to 673 K and using a temperature cooling rate of 100 K/h. For SnIP, equimolar ratios of the elements are used instead, the reaction temperature is lowered to 673 K, and slower cooling with a gradient of 5 K/h is applied. These similarities inspired us to investigate the formation mechanism for both compounds in more detail.

SnIP crystallizes monoclinically, in space group P2/c (No. 13). It contains Z=14 formula units in the unit cell, with lattice parameters of $a = 7.934$ Å, $b = 9.802$ Å, $c = 18.439$ Å and $\beta = 110.06°$.[10]

In 2007, Lange et al. reported on the synthesis of P_{black} and identified the main gas phase species present in the reaction vessel that are P_4 (I) and SnI_2 (II).[16] Minor gas phase components like P_2, SnI_4 (III) and I_2 (IV) were also taken into account, stated here in decreasing order of appearance. No significant impurities like halide containing species were found in the final product which lead to the conclusion that no tin or iodine is incorporated in the final product. Any tin or iodine species

can therefore be present only in the gas phase directing the formation of P_{black} during the short way transport process. In the past few years, several studies were performed to identify a possible reaction mechanism for this P_{red} to P_{black} gas phase transformation reaction in CVD processes.[10a] In solution a reaction mechanism has been evaluated and investigated, featuring a nucleophilic attack of a free lone pair of ethylenediamine (en) to P_{white} (P_4 molecule)[7a] and P_{red}.[10b] Here, the P_4 entity (P_{white}) is opened to a reactive species which tends to rearrange into layers of corrugated P_{black} sheets afterwards. Unfortunately, this solution based synthesis with ethylenediamine leads to P-N bond formation and Nitrogen impurities in P_{black} which has been proven by XPS.[10b] Such impurities which come along in addition to common oxygen impurities caused by oxidation processes in solution and during workup procedures can affect the performance of P_{black} in applications. Using a gas phase-based synthesis route, the solvent influence can fully be suppressed and the oxidation problem can be minimized. Therefore, the gas phase-based synthesis remains a crucial method to grow pure, highly crystalline, large area crystals of P_{black} which then can be used for a top-down fabrication of phosphorene.

A detailed mechanism for the gas phase-based P_{black} synthesis which includes a quantum chemical investigation with local minima structures along the reaction pathway or alternatively the identification of any intermediate species on the reaction pathway are lacking. So far, only assumptions, based on observations during the synthesis, like the occurrence of epitaxial growth of P_{black} on $Sn_{24}Sn_{19.3}I_8$ or the formation of other phosphorus allotropes as precursor states are used to explain or interpret the formation of P_{black}. Two full reaction schemes based on the information from Figure 6 are shown in Figure S1 and S2.
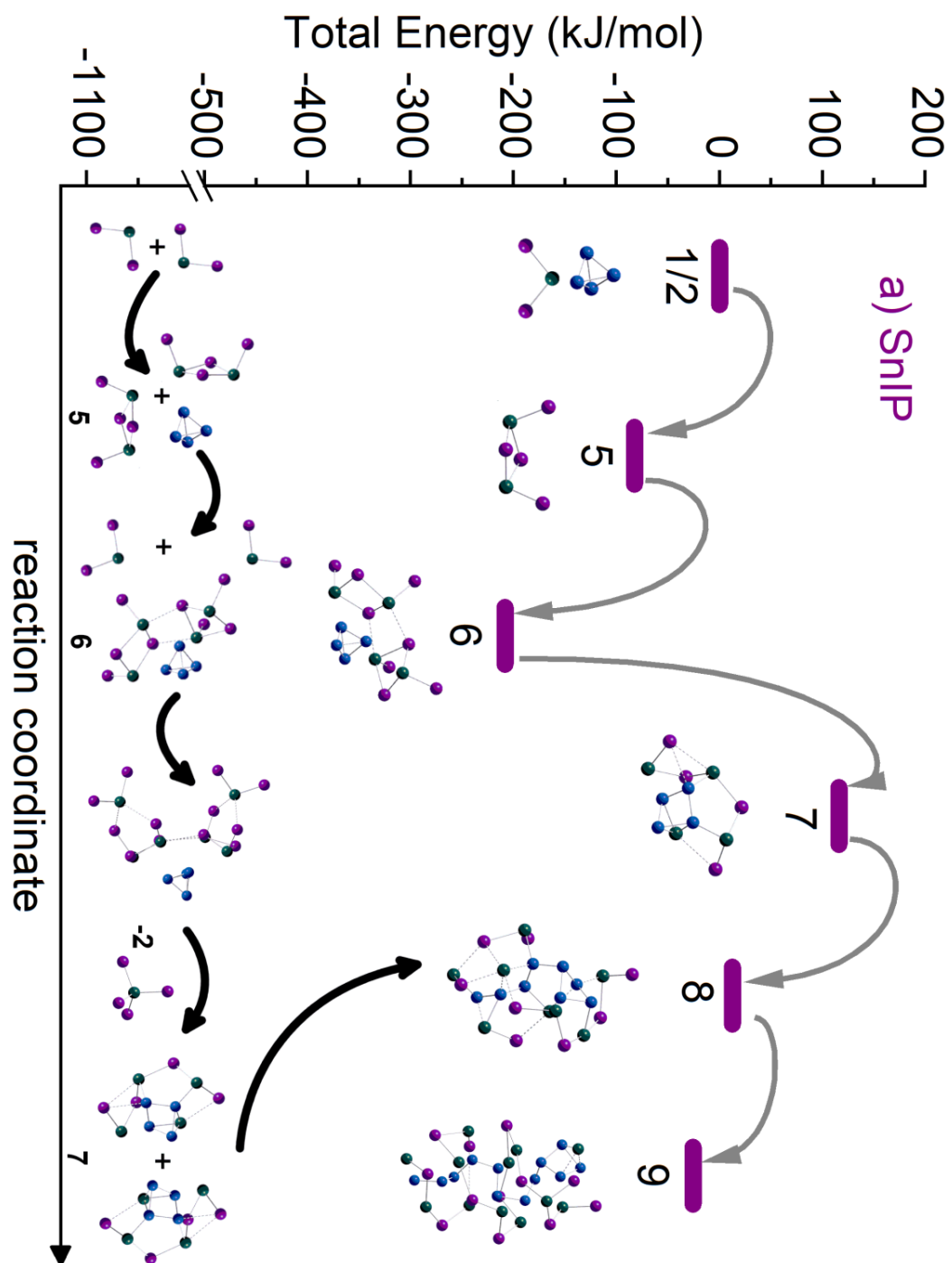
Figure S1. Formation mechanism of SnIP based on total energy calculations (Figure 6). Local mimimum structures are denoted for each step. A rection scheme is shown in the bottom part of the figure for clarity.
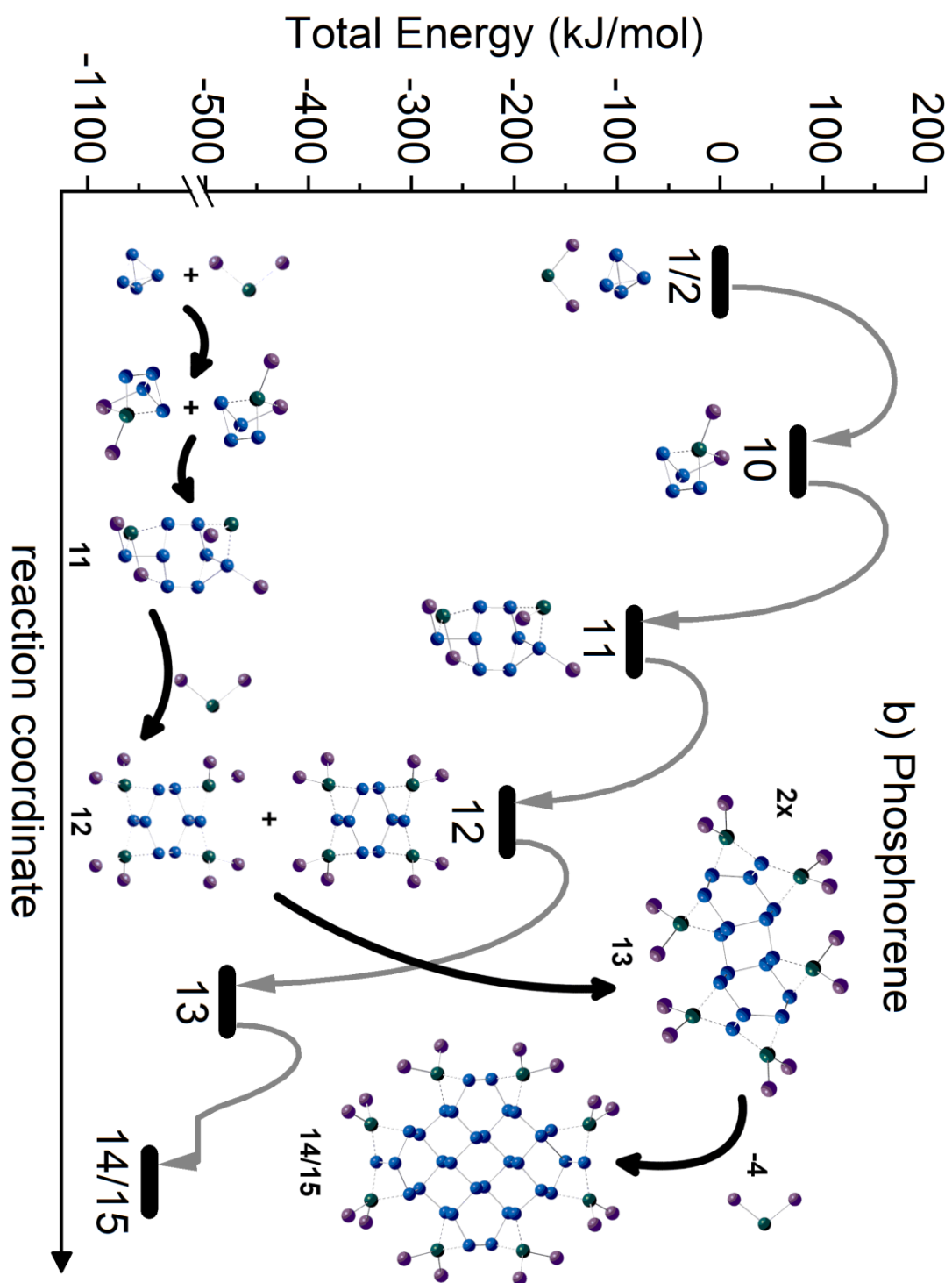
Figure S2. Formation mechanism of P_{black}/phopshorene based on total energy calculations (Figure 6). Local mimimum structures are denoted for each step. A rection scheme is shown in the bottom part of the figure for clarity.

In situ neutron diffraction study on black phosphorus

The formation of formation of black phosphorus was followed in situ in a Neutron diffraction experiment at the ILL, Grenoble, D20 beamline (take off angle 118°; $\lambda = 1.87$ Å; cooling rate 100 K/h, PSD detector; data acquisition time 5 min.[3b] All relevant Neutron data are summarized in Figure S3 and additional experimental data or phase analysis results can be taken from literature.[3b] We found only reflections from black phosphorus in our neutron diffraction experiment and indexed the reflections according structure data[16] from the literature. The evolution of the five strongest P_{black} reflections (040), (151), (023)/(240), (061)/(132), and (261)/(172) are denoted in Figure S3. We found no other crystalline phases than black phosphorus and observed a fast growth within minutes during cooling from 773 K.

Figure S3. In situ Neutron diffraction study on black phosphorus formation. Data are collected at ILL, Grenoble, D20 beamline. We observed fast growth of P_{black} within approx. 100 min from 350 to 450 minutes of total experiment time. Intensities of five observed P_{black} reflections, equivalent to run 72-121 in the lower section, were observed during cooling.

Note 1 - Quasi in situ observation of the synthesis processes
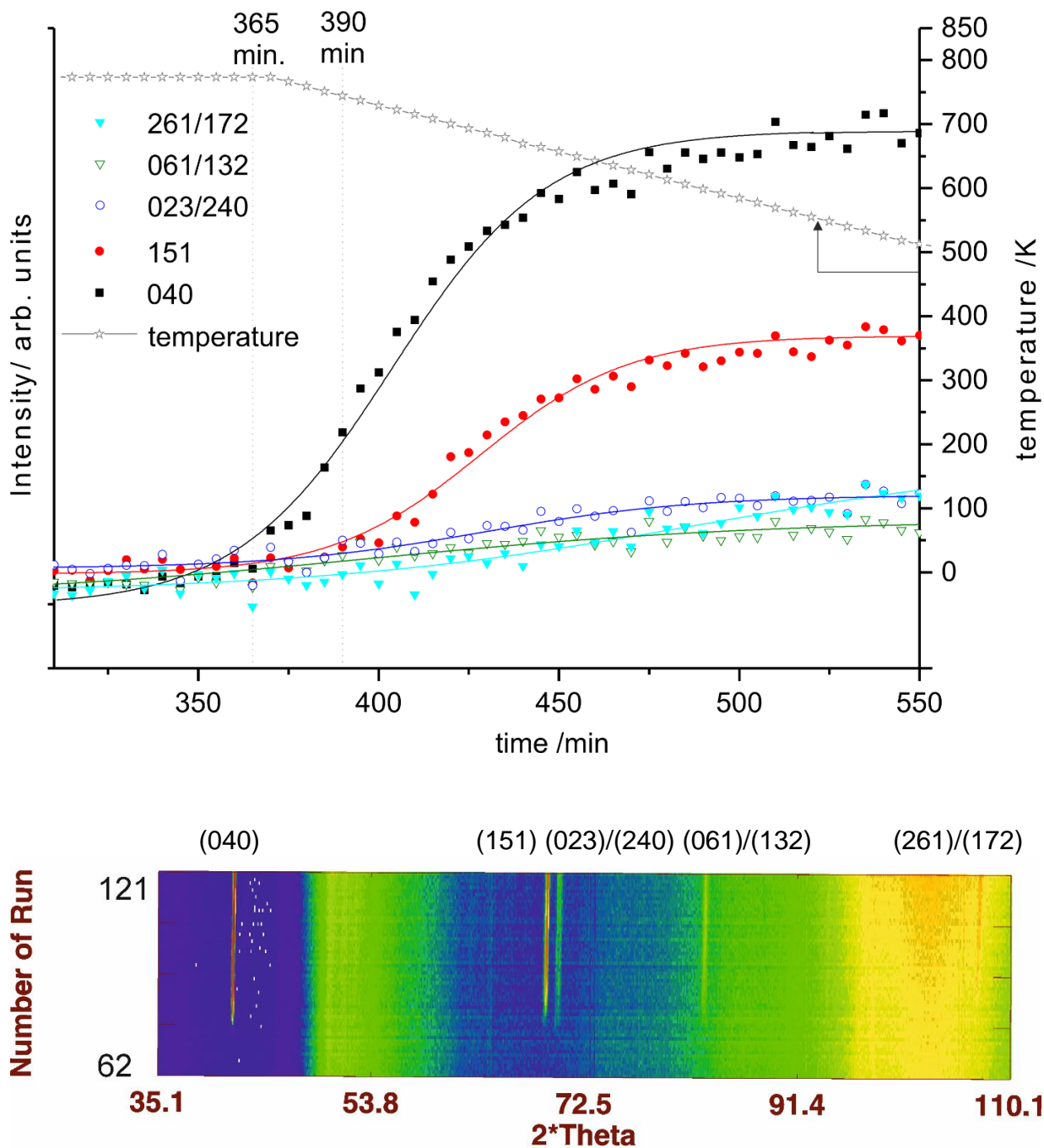
The videos were taken at synthesis temperature (T) directly after the oven was opened. The name of the deposited file indicates the target compound (SnIP or P_{black}) in the ampoules, synthesis temperature T and the file format (.mp4). A dark red condensation product can be noticed on the walls of the P_{black} ampoule while the atmosphere is orange. When opening the oven during SnIP synthesis, there is no obvious condensation process visible on the walls of the ampoule and an orange atmosphere comparable with the one in the P_{black} synthesis is present. Behind the SnIP ampoule shown in the SnIP673K.mp4 file we placed three ampoules containing 25, 50 and 100 mg of iodine (**4**) in order to illustrate the occurrence of significant amounts of iodine in the gas phase. In each iodine ampoule a dark violet/black gas phase is formed which is in significant contrast to the orange gas phase during the P_{black} and SnIP syntheses.

Pblack923K.mp4; SnIP673K.mp4

We therefore conclude that elemental iodine is not present in significant amounts during both syntheses.

Note 2 - Gaussian data sets of DFT calculations

All data sets containing relevant structure data and additional crucial information are deposited in SnIP.zip and Pblack.zip . The names of all files contain a roman numeral (RN) which represents the local minimum structures respective according to Figures 3 and 5. For local minima structure optimization (at 0 K) there is no further extension in the file name. In the case of Gibbs Free Energy calculations, the pressure was set to 50 atm and the respective temperature (T) was added to the name. For example:

RN = II, no T → II.log

RN = II, T = 473 K → II_473K.log

Structures can be visualized directly from the data via the GaussView visualization package. Interested readers can access or download the data directly from the journal.

Note 3 - Barlow's Formula

Barlow's Formula is used to estimate the bursting pressure of a silica glass ampoule.[23a] The pressure *P* represents the estimated maximum internal pressure for a specified tube. *d* and *t* are the diameter and wall thickness. *s* illustrates the tensile strengths which was chosen from the material specifications of Heraeus.[23b] The safety factor *f* is used to ensure a safe working environment in the laboratory.

$$P = 2\frac{t \cdot s}{d \cdot f} \approx 66 \; bar$$

$$d = 0.01 \; m; t = 0.001 \; m; \; s = 5 \cdot 10^7 \; {}^N\!/_{m^2}; \; f = 1.5$$

Taking our ampoule specifications into account we calculated a bursting pressure of approximately 66 bar. For the DFT calculations we used an internal pressure of 50 bar in the ampoule which is a reasonable estimate of the maximum operation conditions during our syntheses.

Note 4 - Thermodynamic calculations in Gaussian

The starting point for all thermodynamic values is the partition function **q** for a given component. Other variables are temperature (**T**), volume (**V**) and pressure (**p**), while the universal gas constant (**R**) is also needed.

$$S = R + R \ln\big(q(V,T)\big) + RT \left(\frac{\delta \, ln \, q}{\delta T}\right)$$

Note 5 - Data summary

In this note we summarize data used in Figures 6 and 7.

Table 1: Energy values in Hartree derived from DFT calculations for all structures at three different temperatures.

	Etot (0 K)	G (473 K)	G (673 K)	G (873 K)
I	-1364.648945	-1364.685663	-1364.709047	-1364.734279
II	-26.342895	-26.394046	-26.420961	-26.449208
III	-49.247987	-	-	-
IV	-22.848169	-22.885933	-22.905297	-22.925518
V	-52.717277	-52.799683	-52.846602	-52.896570
VI	-1470.099776	-1470.264971	-1470.369821	-1470.483381
VII	-1424.279940	-1424.388365	-1424.460196	-1424.538444
VIII	-2848.643500	-2848.831077	-2848.963887	-2849.109908
IX	-4272.982251	-4273.250507	-4273.444899	-4273.659306
X	-1390.963026	-1391.031276	-1391.074728	-1391.121753
XI	-2782.015460	-2782.124826	-2782.201810	-2782.286313
XII	-2834.748296	-2834.911130	-2835.024328	-2835.148469
XIII	-5616.835658	-5617.075676	-5617.253815	-5617.450786
XIV/XV	-11128.330885	-11128.665072	-11128.934059	-11129.234224

Table 2: Differential total energies ΔEtot and ΔG, referenced to the starting materials. ΔEtot and ΔG values in kJ/mol given for all local minimum structures **V** to **XV**.

	ΔEtot	**ΔG (473 K)**	**ΔG (673 K)**	**ΔG (873 K)**
V	-82.7	-30.4	-12.3	4.8
VI	-208.0	-8.2	60.6	125.3
VII	116.1	266.7	320.5	371.8
VIII	12.8	390.8	526.9	656.9
IX	-25.4	576.0	792.7	999.9
X	75.6	127.1	145.1	162.1
XI	-83.4	90.8	152.8	211.7
XII	-206.9	95.5	203.7	306.9
XIII	-479.1	82.0	283.9	476.6
XIV/XV	-1039.9	-71.9	278.3	613.4

Tragmin values

The used parameters in all TRAGMIN evaluations were extracted from the database and summarized in the data file following the program routine for data files.

TragminParameters.dat

3.2 Toward Atomic-Scale Inorganic Double Helices via Carbon Nanotube Matrices - Induction of Chirality to Carbon Nanotubes

Markus R. P. Pielmeier[a], Antti J. Karttunen[b] and Tom Nilges[a]

[a]Technical University of Munich, Department for Chemistry, Lichtenbergstraße 4, 85748 Garching bei München, Germany

[b]Department of Chemistry and Materials Science, Aalto University, P.O. Box 16100, FI-00076 Aalto, Finland

After the details about formation and stereochemistry of SnIP[35] were already discussed, the goal in this project was to understand the perfect racemic mixture in the bulk and to break through the physical threshold to form single double helical rods. The first step was to perform *ab initio* calculations of 1D, pseudo-hexagonal rod packages with different M- and P-SnIP ratios. The comparison of the three devised models showed a preference of the configuration as present in the bulk (alternating chirality around central rod) by at least 8.5 kJ/mol per SnIP strand.

So the racemic mixture seems to be at least partially an energetic effect, which leads to the question, if a single double helix can be stabilized by a bottom-up approach in a matrix. For a first screening the material with the largest versatility of nanotubes and their properties, single walled carbon nanotubes, were chosen. A small range of diameters (13.8 - 15.1 Å) and different electronic properties could be explored simultaneously. CNT (10,10) is metallic, while CNT (18,0) is semimetallic and CNT (15,5) and CNT (19,0) are semiconducting. As SnIP is a very ductile semiconductor, the hybrid structures were all dominated by the properties of the CNTs. The hope of differing results for hybrids of M- and P-SnIP in the chiral CNT (15,5) was disappointed. The analyzed vibrations, which were selected according to Pfister et al.[34], revealed the fact, that "pressuring" the outer helix slightly leads to a relaxation of the inner helix. The energy gained through hybrid formation is in the same order of magnitude as the stabilization energy of a rod package, even though the CNTs are not the best fit for SnIP chemically.

Author contributions: M. R. P. P. supported by A. K. optimized all structures in the framework of DFT, interpreted the vibrational analysis, investigated the electronic structure and depicted the results. M. R. P. P., A. K. and T. N. were involved in discussing the results as well as writing and revising the manuscript.

Article

Toward Atomic-Scale Inorganic Double Helices via Carbon Nanotube Matrices—Induction of Chirality to Carbon Nanotubes

Markus R. P. Pielmeier, Antti J. Karttunen, and Tom Nilges*

Read Online

ACCESS | Metrics & More | Article Recommendations | Supporting Information

ABSTRACT: SnIP, an atomic-scale inorganic double helix compound is composed of a hexagonal rod packing of double helices in the bulk phase. A racemic mixture of *P*- and *M*-SnIP double helices is energetically most favored and present in the solid. In order to evaluate if enantiomer-pure SnIP might be able to realize three different stacking models of seven chiral double helices, an enantiomer-pure, a 2:1, and a racemic 1:1 ratio were investigated according to their energies of formation. While a top-down approach did not lead to single isolated double helices, the development of a bottom-up approach might be beneficial. Motivated by templating strategies in confined geometries we performed first principles density functional theory (DFT) calculations using carbon nanotubes (CNTs) featuring different electronic properties and suitable sizes as matrices to accommodate chiral SnIP double helices. With the aid of DFT, we determined the ideal diameter, stability, and electronic properties of different SnIP@CNT systems. Appropriate molecular starting materials and a feasible formation mechanism are identified based on chemical considerations. An interaction between the CNTs and the SnIP units is evident, causing structure and property modifications of the hybrids. The intercalation of SnIP into a suitable CNT leads to a gain in total energy compared to the isolated systems. Based on our findings, a straightforward way to introduce chirality in suitable CNTs via SnIP@CNT hybrids is feasible.
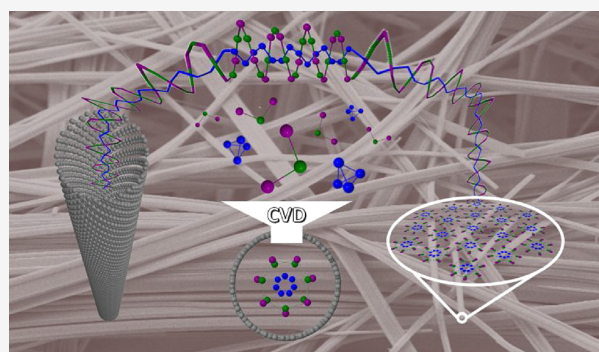
1. INTRODUCTION

Helices and double helices of elements and multinary compounds are subject to intensive scientific research due to their exceptional structural features, intriguing physical properties and stereochemistry.[1,2] Quantum chemistry has recently been used to initiate new ideas for the development of materials ranging from new element allotropes to intriguing composite materials.

Often predicted by first principles calculations like in the case of phosphorus[3−5] or LiP,[6] it became obvious that such materials are interesting but challenging candidates to be synthesized. Especially for solely inorganic materials, the atomic-scale double helix is extremely rare and only very few candidates are known to date. Examples are multiwalled carbon nanotubes containing a phosphorus chain in a helical arrangement[7] or a selenium double helix.[8] In the past few years, the interaction of matter with nanotubes, i.e., by insertion or adsorption of materials[9] was evaluated and selenium or phosphorus@CNTs resulted in efficient battery materials[10−12] or nanotube-stabilized nanowires.[13] Also, the stabilization of metastable compounds consisting of nonhelical structures like polymerized white phosphorus[14] or yellow arsenic,[15] the encapsulation of metals,[16] or simply the band gap change by the application of bending stress to the nanotubes[17] was investigated.

Pfister et al.[18,19] synthesized SnIP, the first inorganic atomic-scale double helix, in 2016. It consists of an inner helix made up of a $[P]^-$ chain and an outer helix made up of $[SnI]^+$ units. Due to its double helical structure, either a left- or a right-handed helix is obtained, which are called *M*- and *P*-helix, respectively. In independent computational studies, the existence of structure homologues of SnIP has been predicted[20−22] where the formation of group 15 element phosphide iodides and bromides are more favored than the lighter homologues. Fluorides are the least likely halides with the SnXP structure.

In order to use the full potential of an inorganic double helical semiconductor, including the chirality of isolated single strands, either the separation after the double helix bundle synthesis of the racemic bulk phase (only realized down to 6–7 shells or 15 nm wide bundles[18]) or a bottom-up synthesis of double helices is needed.

SnIP, as a 1.8 eV semiconductor, was successfully used to fabricate composites in inorganic matrices and 2D materials. Electrochemically etched nanotubular TiO_2 membranes, being a prominent photocatalyst,[23−29] and layered C_3N_4 were used as effective matrices to accommodate SnIP. Heterojunction formation occurred in such hybrid systems resulting in effective water splitting catalysts.[30−32] Motivated by the heterostructure formation we therefore decided to evaluate if the formation of SnIP@CNT heterostructures might be possible.

Carbon nanotubes (CNTs) as such are ideal candidates to act as templates, nanocontainers,[33−36] or nanoreactors[37−42] due to their structural variety and adjustable physical properties (e.g., by functionalization, intercalation, or bending; a recent example for a nanoreactor-mediated synthesis is SnSe).

The structure and inner diameter of a CNT can be varied by the way how graphite layers are formally cut and reconnected. Such resulting nanotubes can be classified by a descriptor composed by two integer numbers. They are multiples of the graphitic hexagonal lattice vectors and define the translational area and thus the entire nanotube. There are known to be three classes of nanotubes called armchair, zigzag, or chiral nanotubes,[43] which is determined by the direction of their propagation vector. Their electronic structures are well examined and can be drastically changed from metallic to semiconducting by slight modifications in their diameter and wrapping angle.[44,45] Three different kinds of nanotubes result: metallic, semimetallic, and semiconducting. The metallic ones all have the descriptor (n,m) with $n = m$ (e.g., $(10,10)$), while for semimetallic systems the descriptor is (n,m) with $n − m$ equals an integer multiple of 3, e.g., $(3,0)$, $(4,1)$, $(18,0)$, and lots of other possibilities. The rest of the nanotubes result in semiconducting systems, e.g., $(4,0)$, $(5,0)$, $(19,0)$, and many more. All of these are promising for tuning band gaps[17,35] in a hybrid system. This scheme is graphically summarized by the company QuantumWise on their "periodic table of carbon nanotubes".[46] As SnIP is a chiral, inorganic, and highly flexible material, the aim of this study is to evaluate the possibility of synthesizing single inorganic SnIP double helix strands in suitable templates/containers. Ideally, such an approach will induce chirality to CNT hosts due to the given chirality of the guest and may lead to a nonracemic formation of SnIP or even an effective separation of the *M*- and *P*-helices.

2. METHODS

Ab initio calculations are carried out using the Crystal17 code[47] and its default settings unless noted otherwise. Due to the size of the studied periodic one-dimensional systems and their low symmetry ($P1$), all optimizations and frequency calculations are performed on the DFT-GGA-level with the functional from Perdew-Burke-Ernzerhof (PBE).[48,49] All-electron LCAO basis sets were applied for C and P, while effective core potential (ECP) and LCAO valence basis set were used for Sn and I (used basis sets are listed in the Supporting Information in CRYSTAL format). Eight Monkhorst-Pack-type *k*-points were used for sampling the reciprocal space (a double-density Gilat net of 16 points was used in the calculation of the Fermi energy).[50] The structures were optimized using Grimme's DFT-D3 dispersion correction scheme as implemented in Crystal17.[51,52] A Fermi smearing of 0.001 Hartree was applied whenever carbon nanotubes were involved. This yields sufficient accuracy for the identification of

crucial changes in the electronic structures of the hybrids, though we are aware that the PBE functional might underestimate the bandgaps.[53] The convergence threshold for the maximum gradient is 0.00045 and for the maximum displacement it is 0.0018. For the visualization of the structures, the JMOL package[54,55] was used. The properties (band structure, DOS, COHP, and vibrational analysis) were calculated with the Crystal17 properties code,[47] and the number of *k*-points increased to 32 and 64 (for the Fermi energy). The plotted densities of states were expanded with 15 Legendre polynomials as implemented in CRYSTAL software. The graphs were generated with the program Origin.

3. RESULTS AND DISCUSSION

After SnIP's discovery and characterization by Pfister et al,[18] the question arose, if a single double helix strand can be realized by a top-down approach. Efforts to delaminate SnIP down to a single double helix strand were not successful. The smallest systems we achieved by mechanical and soft-chemical delamination techniques in our lab still showed six to eight shells of double helices resulting in rod diameters between 10 and 20 nm.[18] Each chiral SnIP double helical strand (see Figure 1a) has a diameter of 0.98 nm and shows either left-
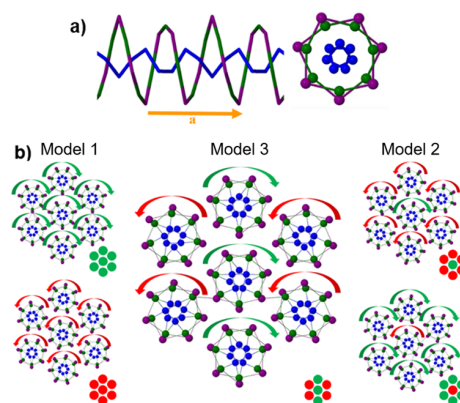
Figure 1. (a) Single strand of double helical *P*-SnIP (sticks representation). The translation unit of the double helix is marked with the orange arrow. On the right side the view along the *a*-axis is given (ball and sticks representation). (b) Simulated 1D-models of SnIP rods with a center rod and one surrounding shell of additional double helices. The screwing direction of each double helix is marked in red (*M*-SnIP enantiomeric form) or green (*P*-SnIP enantiomer). Model 1: center and shell consist of the same SnIP enantiomer; Model 2: the shell is built by only one enantiomer, while the central double helix is of the other enantiomer; and Model 3: central double helix surrounding as realized in bulk SnIP. At the right bottom of each representation a Scheme is given, where the double helices are symbolized by colored dots. Sn atoms: green spheres; I atoms: violet spheres; P atoms: blue spheres.

(*M*-helix) or right-handed (*P*-helix) chirality.[18] Seven SnIP units and two chain windings are needed to form the repetition unit in each rod, to form a right- and left-handed helix pair. Every single rod consists of two separately winding helices, one made up of a phosphorus chain and the other of alternating Sn and I atoms. Defined by the stoichiometry of 1:1:1 (Sn:I:P), the winding of the phosphorus chain has seven atoms in the repetition unit, while the outer chain consists of 14 atoms for the same length. Following the Hermann−Mauguin notation, the symmetry of a single *M*-helix is $p7_32$, while the *P*-helix

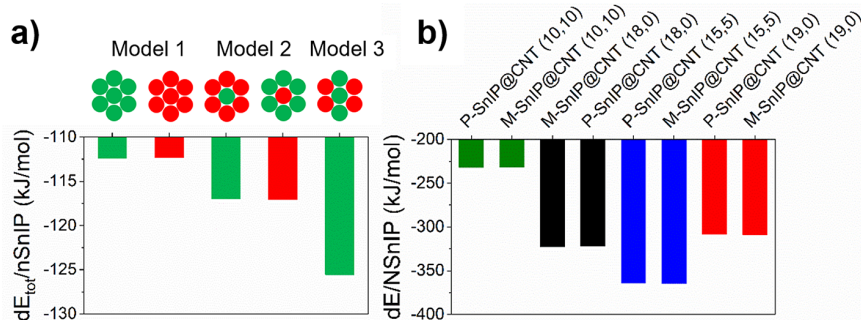**Figure 2.** (a) Total energy differences for three different SnIP models varying the central and neighboring double helix strands. Model 1 is an enantiomer-pure one of either M (red) or P (green) helices, Model 2 represents a 2:1 ratio of double helix strands, and Model 3 represents the realized situation in bulk SnIP (1:1 ratio of double helices). All values are normalized to the number of single SnIP double helices in the repetition unit (NSnIP). (b) Energy difference (dE) for SnIP@CNT hybrid systems in relation to separate components, referenced to a SnIP repetition unit (NSnIP).

corresponds to p7$_4$2, as already described in detail using crystallographic approaches by Müller.[56] Due to the prominent structure, SnIP exhibits high flexibility and compressibility for an inorganic semiconductor and thus qualifies for electronic, optical, and sensor applications.[32,57]

3.1. Formation and Stereochemistry of SnIP. In the first set of calculations, the influence of the stacking order of SnIP double helices is explored by varying the neighboring shell, which surrounds a center strand.

We intend to evaluate why SnIP crystallizes as a racemic mixture of M- and P-double helices and how much this is energetically favored compared to an enantiomeric pure SnIP. In Figure 1b, the three different model systems analyzed in this study are shown, where the colored arrows indicate the rotation symmetry relative to the helix axis perpendicular to the paper layer and a vector pointing into the paper. Every model system consists of a central rod surrounded by one complete shell of six other helices in a hexagonal rod array. The hexagonal rod array of Model 3 is a direct cut-out of the realized SnIP structure.[18] Three different model systems, which differ in the surrounding shell of the central double helix, are analyzed. Model 1 represents the enantiomeric pure systems, where the shell and the central double helices are of the same kind. In Model 2 we investigate a P- and M-central double helix with an entire shell of the other enantiomer. This results in a 2:1 ratio of the different P- and M-double helices for the bulk material. It is important to emphasize the nonracemic nature of the first two models. In Model 3 the shell for the central double helix corresponds to the surrounding in the racemic bulk, resulting in a 1:1 ratio of double helices.

The comparison of the total energy values derived from DFT calculations after geometry optimization are shown in Figure 2a. The racemic mixture of SnIP is already known since its discovery in 2016,[18] but now we can show the differences in energy for other stacking orders. For a single double helix with only one shell (diameter of the entire system approximately 2.8 nm), the gain in total energy compared to that in a single double helix is already 126 kJ/mol for each double helix, if the realized Model 3 is applied. Meaning, for the whole system there is a gain of total energy of 879 kJ/mol when seven double helices are attached to each other. In the case of Model 2 (2:1 ratio of double helix strands) the energy gain per SnIP strand (117.0 kJ/mol) is smaller than that for the racemic Model 3, resulting in an energy difference of 8.5 kJ/mol.

The less-favored models are the enantiomeric pure ones with a difference of 13.2 kJ/mol compared to the realized racemic one. It is evident that both nonracemic Models 1 and 2 are slightly disfavored; however, the entropy of mixing is not included.

Nonetheless, it is obvious that SnIP greatly prefers to aggregate in larger systems with several shells rather than forming single double helices. Thus, the stabilization of single strands is an essential step to atomic scale "nano-rods". Therefore, a matrix, which should also be versatile concerning its size and electronic structure, is needed. Carbon nanotubes are chosen to support the stabilization of single strand SnIP and to enable electronic property tuning.

3.2. DFT Evaluation on Formation and Stability of SnIP@CNT Hybrids. In order realize single SnIP double helices we followed the idea of a template-assisted route and selected CNTs as possible reaction containers or matrices for a bottom-up process. Due to our experience with short way transport reactions of polypnictides and polychalcogenides,[58−61] our successful incorporation of phosphorus and SnIP inside TiO$_2$ nanotube arrays,[30,31] and the self-assembly of SnIP and the 2D material C$_3$N$_4$,[32] we are confident that such a procedure will most probably lead to success. At the moment, we are working on a gas phase transport or the CVD process adapted from the original SnIP synthesis.

In the first step, we identified and selected suitable CNTs from all existing classes considering their electronic structure (metallic, semimetallic, or semiconducting) and the inner CNT diameter, which is supposed to be capable of hosting a single double helix strand. Based on structure considerations, we identified a metallic CNT (10,10), a semiconducting, chiral CNT (15,5), a semimetallic CNT (18,0), and a semiconducting CNT (19,0) as matrices for SnIP and therefore suitable candidates for our DFT calculations (see Table 1). The inner diameters between 13.8 and 15.1 Å fit well to the SnIP double helix space demand of 9.8 Å in the bulk[18] taking also the required distance to the CNTs into account. In Figure 3, the SnIP@CNT hybrid materials are shown. Each set of the structure section used in the DFT calculations is given in Figure 3b,c. Dependent on the CNT structure, a symmetry-optimized structure section was chosen for the model calculations. In the case of the (10,10), (18,0), and (19,0) CNTs, a single repetition unit of the SnIP double helix was sufficient, while for the chiral (15,5) one, a doubled

Table 1. Single-Walled CNTs (SWCNTs) Ordered by an Increasing Diameter (D_t)[a]

CNT (n,m)	D_t [Å]	T [Å]	ratio T/a	N/unit cell	type of CNT
(10,10)	13.8	7.48	3	141	metallic
(15,5)	14.3	15.4	0.5	302	semiconducting
(18,0)	14.3	8.64	2	165	semimetallic
(19,0)	15.1	8.64	2	173	semiconducting

[a]The propagation vector T of the SnIP@CNT hybrid, T/a ratio (with a = the translational period of the bare CNT), total number of atoms (N) per structure model (CNT + SnIP), and the electronic type of the CNT is summarized.
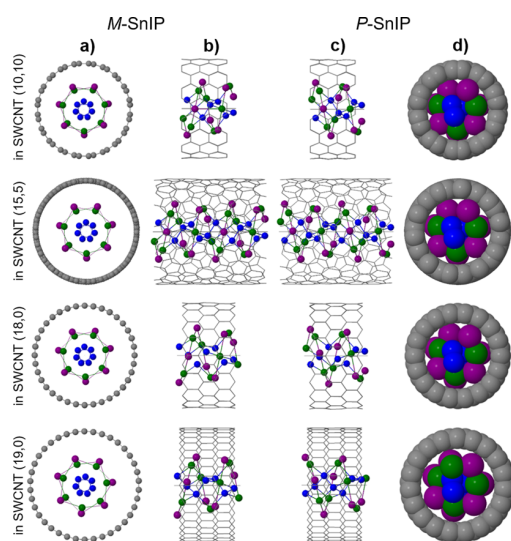

Figure 3. Geometry-optimized structure models of SnIP@CNT hybrids viewed (a), (d) along and (b), (c) perpendicular the CNT propagation axis, featuring (a, b) M-SnIP helix and (c, d) P-SnIP helix, respectively. Furthermore, in (d), a space filling model with van der Waals radii (Sn: 2.17 Å; I: 2.15 Å; and P: 2.08 Å) for SnIP is given. Sn: green spheres; I: violet spheres; and P: blue spheres.

representation was necessary due to the symmetry constrains of the CNT matrix.

For each CNT, we implemented a M- and P-SnIP double helix and performed a DFT structure optimization with full relaxation. Initial 1D geometries are provided with the length of the respective symmetry-optimized CNT section and an

assimilated SnIP substructure because of the flexibility of SnIP.[32]

As shown in Figure 3d for structure-optimized data, each SnIP double helix attaches well to the surrounding CNT matrix. In the space filling representations (Figure 3d), the fit between the two substructures are illustrated. Due to the achiral nature of the (10,10), (18,0), and (19,0) CNTs, no differences in structure parameters are expected for an inserted M- or P-SnIP double helix, while in the case of a chiral (15,5) CNT, differences may occur for the enantiomeric forms.

In general, each successfully realized SnIP@CNT system, independent of the CNT nature, will become chiral because chirality will be induced by the implemented SnIP double helix. This feature might be of interest for the stereochemistry of the hybrids, its usage in light-driven applications, and the separation of the chiral SnIP enantiomers.

In Table 2, a selection of structural parameters, derived from DFT calculations, are summarized. Data are given for the M-SnIP case except for the (15,5) CNT (P-SnIP helix data are given in Table S3). The structure of the CNTs are literally unaffected by the SnIP double helix (see C−C bond lengths in Table 2). Incorporation of a SnIP double helix into CNTs only affects the less rigid, highly compressible, and flexible SnIP substructure. Within the covalently bonded [SnI] and [P] helices, the Sn−I and P−P bond lengths are only slightly affected by the CNT matrix.

All Sn−I bond lengths are found in the same range that we determined for bulk SnIP. The P−P bond lengths are enlarged to 2.21−2.25 Å as compared with bulk SnIP where 2.17−2.21 Å bond lengths are found.

In the dative ionic regime between the two helices, represented by the Sn−P interactions, a little effect is present. In the case of the (10,10) and (15,5) SnIP@CNT hybrids, we found Sn−P bond lengths in the same range as for bulk SnIP, while for the (18,0) and (19,0) CNT, the bond lengths are slightly enlarged to 2.74 and 2.75 Å.

The most prominent and obvious effect is present in the bond angles. Especially the I−Sn−I bond angles of the outer [SnI]$^+$ helix are continuously increased from the (10,10) CNT toward the (19,0) CNT, which directly correlates with the increasing inner CNT diameter. Due to the fact that the shortest distance between the CNT matrix and the SnIP double helix is the C−I contact, the structural 'pressure' affects the outer [SnI]$^+$ chain significantly. According to Mulliken population analysis data,[18] Sn shows a charge from +0.47 to

Table 2. Geometrical Parameters of SnIP@CNT Hybrids Derived from DFT Data after Geometry Optimization Compared with a 1D SnIP Double Helical Strand (1D) and Experimental Values Derived from Single Crystal Structure Determination[a]

	M-SnIP				P-SnIP		
	@ CNT (10,10)	@ CNT (18,0)	@ CNT (19,0)	@ CNT (15,5)	@ CNT (15,5)	1D	experimental
P−P	2.21	2.25	2.25	2.22	2.22	2.22	2.17−2.21
P−P−P	93.3−93.4	97.7−97.8	97.8	94.4−94.5	94.4−94.5	95.1	94.8−96.3
Sn−I	3.07−3.08	3.09−3.10	3.15−3.16	3.12−3.13	3.12−3.13	3.18−3.19	3.06−3.28
I−Sn−I	147.8−148.0	153.1−153.7	155.7−155.8	151.0−151.1	151.0−151.1	154.8−154.9	152.6−153.8
Sn−I−Sn	110.9−111.1	106.0−106.1	103.6	107.9−108.0	107.9	104.1	104.8−106.3
Sn−P	2.65	2.74	2.75	2.68	2.68	2.69	2.66−2.71
I−C	3.22−3.26	3.39−3.53	3.62−3.69	3.35−3.41	3.39−3.42		
C−C	1.43−1.44	1.42−1.43	1.42	1.42−1.43	1.42−1.43		
C−C−C	119.3−120.1	119.4−120.0	119.3−120.1	119.3−120.1	119.4−120.1		

[a]All distances and angles are given in Angstrom (Å) and degrees (°), respectively. For experimental data, the standard deviations are smaller than the last given digit. More P-SnIP data are given in Table S3.
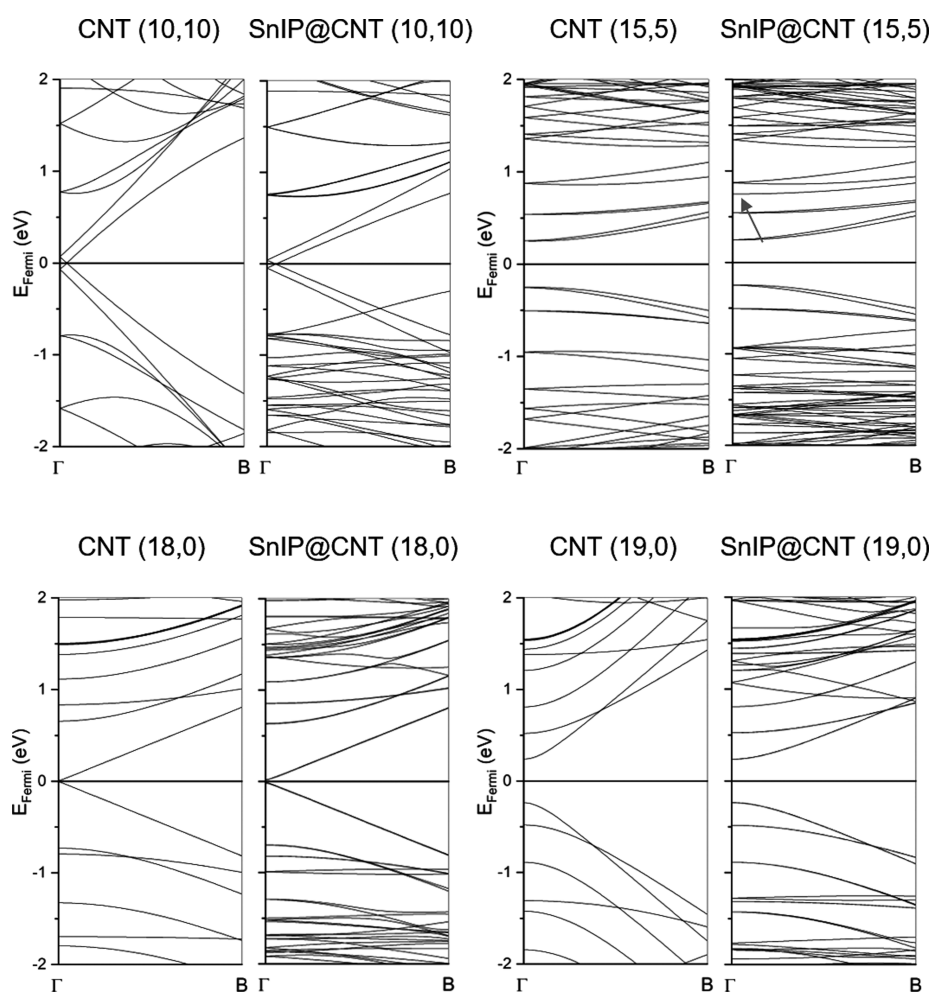
Figure 4. Band structures of pure carbon nanotubes (left) and SnIP-filled nanotubes (right).

+0.51, I from −0.31 to −0.33, and P between −0.16 and −0.17. An electrostatic repulsive interaction between negatively charged I and the electron cloud of the CNTs may cause the flattening of the I−Sn−I angle. On the other hand, the Sn−I−Sn angle is significantly reduced, which is equivalent to a shift of positively charged Sn toward the CNT electron cloud.

The question arises quickly if there are attractive interactions or driving forces present to allow the preparation of such SnIP@CNT systems, so we further investigate the hybrids. The hybrid systems are sorted by the diameter of the CNTs starting with CNT (10,10) featuring a diameter of 13.8 Å. CNT (18,0), CNT (15,5), and CNT (5,15) have a diameter of 14.3 Å, while CNT (19,0) shows the largest diameter of 15.1 Å. A stabilization can be identified in the total energy plot shown in Figure 2b, which is referenced to the number of SnIP repetitions per unit cell (NSnIP in Figure 2b). Here, it is evident that the two enantiomers of SnIP yield energetically equivalent systems (dE < 0.1%, see Supporting Information, Chapter 1, Figure S1 and Tables S1 and S2), even with a chiral nanotube (15,5). In the same moment, the energy gain in comparison to the nonchiral CNTs becomes obvious. This might be explained by the better match of the CNT diameter to the SnIP strand, but the (15,5) CNT with a diameter of 14.31 Å is very close to the (18,0) one with 14.29 Å and a

difference of approximately 44 kJ/mol seems too large to be explained by the slight change in the diameter.

The comparison of the band structures of pure CNTs to the filled hybrids (see Figure 4) indicates almost no changes for bands in the vicinity of the Fermi level. At a closer look, the band gaps stay practically the same as in pure CNTs, but the slope of some bands decreases significantly. The steepness of the bands in these materials correlates directly with the Fermi velocity, as the CNTs are Dirac materials.[62] Here, the decreasing slopes can be interpreted as less dispersion in the bands, which imply less strain in our SnIP@CNT hybrids. This effect is the most prominent in the cases of the metallic CNT (10,10) and the semiconducting CNT (19,0) hybrids, which feature the minimum and the maximum diameter of the considered CNTs.

All examined hybrids have no bands inside a range of 1 eV above the Fermi energy provided by SnIP except SnIP@CNT (15,5) at ∼0.75 eV (black arrow, Figure 4). Though it is known that the PBE functional underestimates the band gap of SnIP a little,[18,20] the lowering of the states compared to other hybrids and the separated components is apparent. This hints to a better interaction in the case of the chiral nanotube compared to the achiral ones, which must be further investigated.
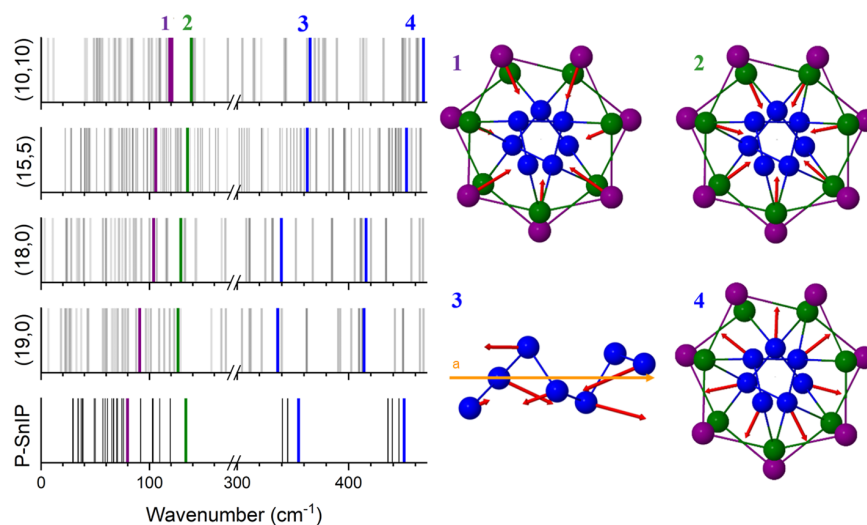
Figure 5. Vibrational analysis of hybrids with respective CNTs and a 1D *P*-SnIP strand. 1: I-breathing mode; 2: Sn-breathing mode; 3: P-stretching (<400 cm^{-1}), and 4: P-breathing (>400 cm^{-1}) modes. Movies of the modes are given in the Supporting Information (Chapter 4).

Crystal orbital Hamilton population (COHP)[63] analysis is a powerful tool, which differentiates bonding (negative) and antibonding (positive) states of selected kinds of atoms with each other. The most important part of CNT-SnIP interactions is localized between the outer SnI helix and the CNT.

Therefore, C−I and C−Sn interactions might occur. COHP analysis is useful to identify, which kind of interactions are present between the chosen atom species (see Supporting Information, Figure S3a). To check the bonding situation, the final geometries are restarted as single point (sp) calculations without the D3 correction. This yields the respective differences in total energies between 295 and 470 kJ/mol per SnIP repetition unit compared to the D3 corrected ones. The result can be interpreted as a mixture of dispersion and covalency, but the form of the graphs suggest that dispersion always plays an important role in this system (see Supporting Information, Figure S1 on the right.). By comparing the integrated densities of the COHPs in the same manner (see Supporting Information Figure S3b), it becomes apparent that the Sn−P interactions are mainly dispersive in nature, which is in good agreement with the experimental data.[18] For further details and results, please refer to Chapters 1 to 3 in the Supporting Information.

3.3. Identification and Characterization of SnIP@CNT Hybrids via Vibrational Spectroscopy.
Bulk SnIP is already well characterized and Raman spectroscopy has proven to be a powerful and quick tool to identify and investigate SnIP after formation. Calculated and measured Raman modes can therefore be used to identify synthesized SnIP@CNT hybrids and to monitor the bonding situation in the double helices. Vibrational modes were derived from DFT data using our hybrid models (see Section 2). These modes are all situated in the fingerprint area of the spectra (∼50−500 cm^{-1}). All selected modes for the bonding analysis are shown as an indicative illustration in Figure 5 (1−4) and provided as movies in the supporting information. The selection was made according to the investigations of Baumgartner,[20] where characteristic breathing modes of Sn (green), I (magenta), and P (blue; >400 cm^{-1}) as well as a stretching mode of P (blue, <400 cm^{-1}) were chosen in the bulk material. These vibrations were compared to a 1D *P*-SnIP strand as referenced at the bottom in Figure 5. The iodine vibrations show the expected behavior of consistently increasing wavenumbers with decreasing diameters of the CNTs (from the bottom upward), equivalent to rising pressure applied to bulk SnIP, as reported in the work of Ott et al.[32] The other selected modes show an equivalent behavior, meaning that first all of them lower the vibrational frequency compared to pure SnIP. By the looks of it, "pressuring" the iodine atoms just a little on the outer perimeter first releases some strain from the rest of the SnIP helices in the CNT (19,0). A Sn−I−Sn angle (see Table 2) of 103.6° in SnIP@CNT (19,0) is the only one smaller than the experimental angle 104.8°, which equals a slight shift of iodine toward the CNT. This is confirmed by the longest Sn−I bond (3.16 Å) in SnIP@CNT (19,0) for all hybrids. This also impacts the total energy landscape and leads to the minimum-like distribution of the total energies, as shown in Figure 2b.

3.4. Realization and Routes to SnIP@CNT Hybrids.
Several semiconductors have been successfully incorporated into CNTs that have selenium as an atomic-scale double helix,[8] phosphorus as coil-like helical chains,[3] SnSe as chains or rods,[37] and columnar or black phoshorus sheets.[40] For the latter it has been shown via calculations and experiments that the diameter of the CNT plays a certain role for allotrope formation and that unusual and unexpected structures can be stabilized in such matrices. Obviously, the combination of helical arrangements and CNTs as matrices or reaction containers is beneficial and leads to a formation of hybrid materials. For a helical coil allotrope of phosphorus, as reported by the Tománek group recently, the interaction between the phosphorus allotrope and a neighboring graphene layer is in the same order as the interlayer interaction between two phosphorene sheets in the black phosphorus allotrope.[3] They observed lone-pair electron states in the isolated phosphorus chain that contributes significantly to the electronic interchain coupling, which modified the band structure for the hybrid material in relation to the pure chain. Consequently, this allotrope has been synthesized and characterized 1 year later in a CNT.[7] It has also been shown in this nice work that DFT as a method can only approximate the bonding situation for such weak interactions. As shown herein, PBE will underestimate and LDA will overestimate these

interactions independent of the fact, if Grimme corrections are applied or not. Due to our own experiences with the description of weak interactions in phosphorus allotropes by quantum chemical calcualtions,[64,65] we decided to use PBE and Grimme-D3 corrections in our investigations to get a first impression of the probability to realize the title compounds.

In all cases like Se@CNT or Phosphorus@CNT, the shortest contacts between the guests and the host matrix are defined by an extensive lone-pair system of the guest pointing toward the surrounding host matrix. Interactions therefore occur between the lone pairs and the π-system of the sp^2-hybridized carbon skeleton of the CNT. If SnIP is considered as a guest, we find a rather comparable situation where lone pairs of tin and strongly polarized electron clouds of iodide define the surface of the SnIP double helices. The bonding situation between the double helix strands in SnIP and the covalent interactions within the single helices were reported elsewhere.[18] According to our DFT calculations, exactly such weak but important interactions occur for SnIP incorporated in a CNT of suitable size. A plausible formation mechanism is postulated in the Supporting Information (Chapter 5).

As stated before, the best possible synthesis route to incorporate SnIP into CNTs might be via the gas phase using highly volatile starting materials like phosphorus and tin iodide at elevated temperatures. Now, the question arises quicky, if such starting materials can be supplied effectively into CNTs to allow the formation of SnIP. At least 50% of 100 nm wide and several micrometers long channels in a TiO$_2$ membrane were successfully filled by this approach,[31] and nanosized SnIP (diameter of SnIP rods approximately 30–50 nm) were successfully formed inside the channels. Red phosphorus was also effectively incorporated into multiwalled CNTs via the gas phase at 550° to 600 °C, leading to a significant loading of red phosphorus inside the CNT.[66] During a conversion reaction with Na to Na$_3$P along with a volume increase of several hundred percents, it became evident that incorporated red phosphorus is transformed to white phosphorus during this reaction. Such a highly reactive phosphorus allotrope is also needed to form SnIP with SnI$_2$ as the second gaseous component.

In a detailed ab initio DFT study it was shown that volatile niobium chlorides are suitable candidates to be incorporated as molecular species into CNTs via the gas phase. Species like NbCl$_3$ can be physisorbed to the walls with a gain in physisorption energy approaching the surface, and they can fulfill a reasonable electron transfer to the carbon matrix upon adsorption.[67] A charge transfer of approximately 0.5 electrons per molecule was predicted in this case. The final postulated products after heat treatment and disproportionation at elevated temperatures were Nb metal nanotubes and NbCl$_5$. It has been shown herein that CNTs can be catalytically active for such a transformation and that they can act as electron acceptors for donating species. Therefore, SnI$_2$ can be a suitable candidate to be incorporated via the open ends of CNTs as a necessary second starting material beside the aforementioned phosphorus.

In recent studies it has been reported that doping of the CNT with cations like platinum or phosphorus and phosphorus-containing species under mild conditions (in contrast to the harsh conditions for a direct doping of CNTs with nitrogen or boron during the synthesis process[68]) may increase the Lewis acidity of a given CNT.[69,70] Due to the temperature treatment of CNTs with possible starting compounds like Sn/SnI$_4$ (which comproportionate to SnI$_2$ at elevated temperatures) and phosphorus during hybrid formation via the gas phase at temperatures <600 °C, a certain modification by doping of the CNT cannot be fully ruled out. Any doping by cations to the CNT would be beneficial in enhancing the interaction to the Lewis basic core of SnIP double helices. SnIP with its Sn lone pairs and the polarized iodide electron cloud pointing outward the SnIP double helix tends to be Lewis basic in nature.

3.5. Chirality in SnIP@CNT Hybrids. Finally, a successful stabilization of a single chiral SnIP double helix (either a M- or P-SnIP double helix) in a CNT will directly lead to a chiral product. This is independent of the nature of the SnIP helix and the surrounding CNT and includes achiral CNTs. A chiral CNT like for instance the (15,5) one used in our calculations is not mandatory to create chirality but it will directly create enantiomer pairs. Unfortunately, we could not detect any significant energetic differences when the two different SnIP enantiomers are embedded in the same enantiomeric form of a (15,5) CNT. Nevertheless, once the modification of CNTs by incorporating chiral and semiconducting entities is realized it will have a huge impact on the (stereo)chemistry of the CNT backbone in terms of functionalization[71−73] and doping.[68] Such hybrids may have a certain potential in energy conversion applications due to the combination of different semiconductors or concerning the efficiency and the selectivity in catalysis.

4. CONCLUSIONS

DFT-based quantum chemical calculations were successfully used to evaluate early nucleation steps with different stereochemistries during SnIP formation and the occurrence of SnIP@CNT hybrids. For pure SnIP, the stability differences concerning the vicinity of a single rod are determined in terms of total energy. Three different models, each consisting of a center double helix strand neighbored by six additional ones in a hexagonal rod array, were compared featuring a racemic mixture of right- and left-handed double helices, a 2:1 excess, and finally the enantiomeric pure models with the same rotation direction for all double helices. It turned out that the realized racemic mixture (Model 1) is energetically favored by 8.5 kJ/mol compared with the excess Model 2 (2:1 ratio of double helices), and the enantiomeric pure SnIP seems to be the least favored one by another 4.7 kJ/mol relative to the previous case. Single SnIP double helices need to be stabilized either by themselves via agglomeration or by a surrounding matrix. An energy gain of 879 kJ/mol, if one shell consisting of six double helix strands is coordinated to a single SnIP double helix substantiates this aspect, explains the difficulty to generate single double helices and renders a matrix approach necessary.

The simulation of a stable SnIP single double helical rod in a SWCNT was successful in different types of suitable CNTs. Four different CNTs, (10,10), (15,5), (18,0), and (19,0) were identified as suitable candidates to accommodate single SnIP double helix strands due to geometric constraints. In all cases we found no significant energy differences for the two incorporated enantiomeric forms of SnIP double helices, the M- and P-SnIP double helix, in the respective CNTs. There is no computational evidence that an incorporation of a given enantiomeric form of a SnIP double helix is favored when a chiral CNT is present. The geometrical adjustments and structural changes after incorporation are fully performed

within the SnIP substructure, as expected for the less ridged and flexible counterpart. The CNT host matrix remains almost unchanged. Compared to independently calculated SWCNT and SnIP double helix strands, only the very soft and flexible SnIP part is adjusted and reorganized slightly.

All three types of CNTs according to its electronic properties (metallic, semimetallic, and semiconducting) are capable to host a single SnIP double helix strand without significant changes in their electronic properties. In each case, the electronic structure of the CNT is decisive for the resulting electronic structure of the hybrid SnIP@CNT system. The best candidate for a successful synthesis should be the SnIP@ CNT (15,5) system because it is energetically favored compared to the other hybrids, though its diameter is very close to the SnIP@CNT (18,0) structure.

The comparison of the stabilization energy ΔE of a seven SnIP double helix arrangement with a free-standing one in a CNT matrix (SnIP@CNT) gives a hint to the reason for the problematic delamination down to a single SnIP double helix by a top-down approach. Though the hybrids show no mentionable amount of bonding states, the energy gain is in the same order of magnitude as in the pure SnIP needle for a single shell rendering a successful synthesis possible. A shielding of electrons and electron pairs pointing outward from the helix and the dispersion interactions between SnIP and the CNT are plausible features and very important in these hybrids.

■ ASSOCIATED CONTENT

ⓢ Supporting Information

The Supporting Information is available free of charge at https://pubs.acs.org/doi/10.1021/acs.jpcc.0c02079.

Details concerning the total energies, density of states, crystal orbital Hamilton population, and vibrational modes of SnIP@CNT hybrids (PDF)

Quantum chemical basis sets and data (TXT)

pSnIP1D80I (MP4)

pSnIP1D132Sn (MP4)

pSnIP1D350P (MP4)

pSnIP1D437P (MP4)

■ AUTHOR INFORMATION

Corresponding Author

Tom Nilges − *Technical University of Munich, 85748 Garching, Germany;* ⦿ orcid.org/0000-0003-1415-4265; Email: tom.nilges@tum.de

Authors

Markus R. P. Pielmeier − *Technical University of Munich, 85748 Garching, Germany*

Antti J. Karttunen − *Department of Chemistry and Materials Science, Aalto University, FI-00076 Aalto, Finland*

Complete contact information is available at: https://pubs.acs.org/10.1021/acs.jpcc.0c02079

Author Contributions

M.R.P.P. conducted the DFT investigations with the aid of A.J.K. under the supervision of T.N. The manuscript was written by contributions from all the authors.

Notes

The authors declare no competing financial interest.

■ REFERENCES

(1) Ouhajji, S.; van Ravensteijn, B. G. P.; Fernández-Rico, C.; Lacina, K. S.; Philipse, A. P.; Petukhov, A. V. Wet-Chemical Synthesis of Chiral Colloids. *ACS Nano* **2018**, *12*, 12089−12095.

(2) Zhou, C.; Ren, Y.; Han, J.; Xu, Q.; Guo, R. Chiral Polyaniline Hollow Nanotwists toward Efficient Enantioselective Separation of Amino Acids. *ACS Nano* **2019**, *13*, 3534−3544.

(3) Liu, D.; Guan, J.; Jiang, J.; Tománek, D. Unusually Stable Helical Coil Allotrope of Phosphorus. *Nano Lett.* **2016**, *16*, 7865−7869.

(4) Sansone, G.; Maschio, L.; Karttunen, A. J. One-Dimensional Phosphorus Nanostructures: from Nanorings to Nanohelices. *Chem. — Eur. J.* **2017**, *23*, 15884−15888.

(5) Liu, J. Effect of phosphorus doping on electronic structure and photocatalytic performance of g-C$_3$N$_4$: Insights from hybrid density functional calculation. *J. Alloy. Compd.* **2016**, *672*, 271−276.

(6) Ivanov, A. S.; Morris, A. J.; Bozhenko, K. V.; Pickard, C. J.; Boldyrev, A. I. Inorganic double-helix structures of unusually simple lithium-phosphorus species. *Angew. Chem., Int. Ed.* **2012**, *51*, 8330−8333.

(7) Zhang, J.; Zhao, D.; Xiao, D.; Ma, C.; Du, H.; Li, X.; Zhang, L.; Huang, J.; Huang, H.; Jia, C. L.; et al. Assembly of Ring-Shaped Phosphorus within Carbon Nanotube Nanoreactors. *Angew. Chem., Int. Ed.* **2017**, *56*, 1850−1854.

(8) Fujimori, T.; dos Santos, R. B.; Hayashi, T.; Endo, M.; Kaneko, K.; Tománek, D. Formation and properties of selenium double-helices inside double-wall carbon nanotubes: experiment and theory. *ACS Nano* **2013**, *7*, 5607−5613.

(9) Khazaei, M.; Farajian, A. A.; Jeong, G.-H.; Mizuseki, H.; Hirata, T.; Hatakeyama, R.; Kawazoe, Y. Dynamical Criteria for Cs Ion Insertion and Adsorption at Cap and Stem of Carbon Nanotubes: Ab Initio Study and Comparison with Experiment. *J. Phys. Chem. B* **2004**, *108*, 15529−15535.

(10) Balakumar, K.; Kalaiselvi, N. Selenium containing Tube-in-Tube carbon: A one dimensional carbon frame work for selenium cathode in Li-Se battery. *Carbon* **2017**, *112*, 79−90.

(11) Han, K.; Liu, Z.; Ye, H.; Dai, F. Flexible self-standing graphene−Se@CNT composite film as a binder-free cathode for rechargeable Li−Se batteries. *J. Power Sources* **2014**, *263*, 85−89.

(12) Zeng, L.; Wei, X.; Wang, J.; Jiang, Y.; Li, W.; Yu, Y. Flexible one-dimensional carbon−selenium composite nanofibers with superior electrochemical performance for Li−Se/Na−Se batteries. *J. Power Sources* **2015**, *281*, 461−469.

(13) Li, W.; Zhao, M.; Xia, Y.; He, T.; Song, C.; Lin, X.; Liu, X.; Mei, L. Silver-filled single-walled carbon nanotubes: Atomic and electronic structures from first-principles calculations. *Phys. Rev. B* **2006**, *74*, 195421.

(14) Hart, M.; White, E. R.; Chen, J.; McGilvery, C. M.; Pickard, C. J.; Michaelides, A.; Sella, A.; Shaffer, M. S. P.; Salzmann, C. G. Encapsulation and Polymerization of White Phosphorus Inside Single-Wall Carbon Nanotubes. *Angew. Chem., Int. Ed.* **2017**, *56*, 8144−8148.

(15) Hart, M.; Chen, J.; Michaelides, A.; Sella, A.; Shaffer, M. S. P.; Salzmann, C. G. One-Dimensional Arsenic Allotropes: Polymerization of Yellow Arsenic Inside Single-Wall Carbon Nanotubes. *Angew. Chem., Int. Ed.* **2018**, *57*, 11649.

(16) Manzetti, S. Molecular and crystal assembly inside the carbon nanotube: encapsulation and manufacturing approaches. *Adv. Manuf.* **2013**, *1*, 198−210.

(17) Minot, E. D.; Yaish, Y.; Sazonova, V.; Park, J.-Y.; Brink, M.; McEuen, P. L. Tuning Carbon Nanotube Band Gaps with Strain. *Phys. Rev. Lett.* **2003**, *90*, 156401.

(18) Pfister, D.; Schäfer, K.; Ott, C.; Gerke, B.; Pöttgen, R.; Janka, O.; Baumgartner, M.; Efimova, A.; Hohmann, A.; Schmidt, P.; et al. Inorganic Double Helices in Semiconducting SnIP. *Adv. Mater.* **2016**, *28*, 9783−9791.

(19) Utrap, A.; Xiang, N. Y.; Nilges, T. A yield-optimized access to double-helical SnIP via a Sn/SnI$_2$ approach. *J. Cryst. Growth* **2017**, *475*, 341−345.

(20) Baumgartner, M.; Weihrich, R.; Nilges, T. Inorganic SnIP-Type Double Helices in Main-Group Chemistry. *Chem. − Eur. J.* **2017**, *23*, 6452−6457.

(21) Li, X.; Dai, Y.; Ma, Y.; Li, M.; Yu, L.; Huang, B. Landscape of DNA-like inorganic metal free double helical semiconductors and potential applications in photocatalytic water splitting. *J. Mater. Chem. A* **2017**, *5*, 8484−8492.

(22) Bijoy, T. K.; Murugan, P.; Kumar, V. Atomic structure and electronic properties of A$_2$B$_2$XY (A = Si-Pb, B = Cl-I, and XY = PN and SiS) inorganic double helices: first principles calculations. *Phys. Chem. Chem. Phys.* **2018**, *20*, 10060−10068.

(23) Schneider, J.; Matsuoka, M.; Takeuchi, M.; Zhang, J.; Horiuchi, Y.; Anpo, M.; Bahnemann, D. W. Understanding TiO$_2$ Photocatalysis: Mechanisms and Materials. *Chem. Rev.* **2014**, *114*, 9919−9986.

(24) Tang, J.; Durrant, J. R.; Klug, D. R. Mechanism of Photocatalytic Water Splitting in TiO$_2$. Reaction of Water with Photoholes, Importance of Charge Carrier Dynamics, and Evidence for Four-Hole Chemistry. *J. Am. Chem. Soc.* **2008**, *130*, 13885−13891.

(25) Ma, Y.; Wang, X.; Jia, Y.; Chen, X.; Han, H.; Li, C. Titanium Dioxide-Based Nanomaterials for Photocatalytic Fuel Generations. *Chem. Rev.* **2014**, *114*, 9987−10043.

(26) Suhadolnik, L.; Marinko, Ž.; Ponikvar-Svet, M.; Tavčar, G.; Kovač, J.; Čeh, M. Influence of Anodization-Electrolyte Aging on the Photocatalytic Activity of TiO$_2$ Nanotube Arrays. *J. Phys. Chem. C* **2020**, *124*, 4073−4080.

(27) Shiraishi, Y.; Toi, S.; Ichikawa, S.; Hirai, T. Photocatalytic NH3 Splitting on TiO$_2$ Particles Decorated with Pt−Au Bimetallic Alloy Nanoparticles. *ACS Appl. Nano Mater.* **2020**, 1612.

(28) Jang, M.; Lee, H.; Lee, W. Large Area Honeycomb-Structured TiO$_2$ Film for Photocatalytic Water Splitting. *ACS Appl. Nano Mater.* **2019**, *3*, 131−137.

(29) Williams, G.; Seger, B.; Kamat, P. V. TiO$_2$-Graphene Nanocomposites. UV-Assisted Photocatalytic Reduction of Graphene Oxide. *ACS Nano* **2008**, *2*, 1487−1491.

(30) Üzer, E.; Kumar, P.; Kisslinger, R.; Kar, P.; Thakur, U. K.; Shankar, K.; Nilges, T. Vapor growth of binary and ternary phosphorus-based semiconductors into TiO$_2$ nanotube arrays and application in visible light driven water splitting. *Nanoscale Adv.* **2019**, *1*, 2881−2890.

(31) Üzer, E.; Kumar, P.; Kisslinger, R.; Kar, P.; Thakur, U. K.; Zeng, S.; Shankar, K.; Nilges, T. Vapor Deposition of Semiconducting Phosphorus Allotropes into TiO$_2$ Nanotube Arrays for Photoelectrocatalytic Water Splitting. *ACS Appl. Nano Mater.* **2019**, *2*, 3358−3367.

(32) Ott, C.; Reiter, F.; Baumgartner, M.; Pielmeier, M.; Vogel, A.; Walke, P.; Burger, S.; Ehrenreich, M.; Kieslich, G.; Daisenberger, D.; et al. Flexible and Ultrasoft Inorganic 1D Semiconductor and Heterostructure Systems Based on SnIP. *Adv. Funct. Mater.* **2019**, *29*, 1900233.

(33) Zaporotskova, I. V.; Boroznina, N. P.; Parkhomenko, Y. N.; Kozhitov, L. V. Carbon nanotubes: Sensor properties. A review. *Modern Electronic Materials* **2016**, *2*, 95−105.

(34) Balasubramanian, K.; Lee, E. J. H.; Weitz, R. T.; Burghard, M.; Kern, K. Carbon nanotube transistors − chemical functionalization and device characterization. *Phys. Stat. Sol. A* **2008**, *205*, 633−646.

(35) Kumar, U.; Sikarwar, S.; Sonker, R. K.; Yadav, B. C. Carbon Nanotube: Synthesis and Application in Solar Cell. *J. Inorg. Organomet. Polym.* **2016**, *26*, 1231−1242.

(36) Rao, R.; Pint, C. L.; Islam, A. E.; Weatherup, R. S.; Hofmann, S.; Meshot, E. R.; Wu, F.; Zhou, C.; Dee, N.; Amama, P. B.; et al. Carbon Nanotubes and Related Nanomaterials: Critical Advances and Challenges for Synthesis toward Mainstream Commercial Applications. *ACS Nano* **2018**, *12*, 11756−11784.

(37) Slade, C. A.; Sanchez, A. M.; Sloan, J. Unprecedented New Crystalline Forms of SnSe in Narrow to Medium Diameter Carbon Nanotubes. *Nano Lett.* **2019**, *19*, 2979−2984.

(38) Agasti, N.; Astle, M. A.; Rance, G. A.; Alves Fernandes, J.; Dupont, J.; Khlobystov, A. N. Cerium Oxide Nanoparticles Inside Carbon Nanoreactors for Selective Allylic Oxidation of Cyclohexene. *Nano Lett.* **2019**, *20*, 1161−1171.

(39) Fedoseeva, Y. V.; Orekhov, A. S.; Chekhova, G. N.; Koroteev, V. O.; Kanygin, M. A.; Senkovskiy, B. V.; Chuvilin, A.; Pontiroli, D.; Riccò, M.; Bulusheva, L. G.; et al. Single-Walled Carbon Nanotube Reactor for Redox Transformation of Mercury Dichloride. *ACS Nano* **2017**, *11*, 8643−8649.

(40) Zhang, J.; Fu, C.; Song, S.; Du, H.; Zhao, D.; Huang, H.; Zhang, L.; Guan, J.; Zhang, Y.; Zhao, X.; et al. Changing the Phosphorus Allotrope from a Square Columnar Structure to a Planar Zigzag Nanoribbon by Increasing the Diameter of Carbon Nanotube Nanoreactors. *Nano Lett.* **2019**, *20*, 1280−1285.

(41) Astle, M. A.; Rance, G. A.; Loughlin, H. J.; Peters, T. D.; Khlobystov, A. N. Molybdenum Dioxide in Carbon Nanoreactors as a Catalytic Nanosponge for the Efficient Desulfurization of Liquid Fuels. *Adv. Funct. Mater.* **2019**, *29*, 1808092.

(42) Aygün, M.; Chamberlain, T. W.; Gimenez-Lopez, M. D. C.; Khlobystov, A. N. Magnetically Recyclable Catalytic Carbon Nanoreactors. *Adv. Funct. Mater.* **2018**, *28*, 1802869.

(43) Krüger, A., *Neue Kohlenstoffmaterialien - Eine Einführung.* Teubner: 2007; pp 125−286.

(44) Wilder, J. W. G.; Venema, L. C.; Rinzler, A. G.; Smalley, R. E.; Dekker, C. Electronic structure of atomically resolved carbon nanotubes. *Nature* **1998**, *391*, 59.

(45) Malik, S. R.; Maqbool, M. A.; Hussain, S.; Irfan, H. Carbon Nano-Tubes: Description, Properties and Applications. *J. Pak. Mater. Soc.* **2008**, *1*, 21−26.

(46) *Periodic Table of Carbon Nanotubes.* https://quantumwise.com/documents/CNT_PeriodicTable.pdf (accessed 30.01.2020).

(47) Dovesi, R.; Saunders, V. R.; Roetti, C.; Orlando, R.; Zicovich-Wilson, C. M.; Pascale, F.; Civalleri, B.; Doll, K.; Harrison, N. M.; Bush, I. J. et al. *CRYSTAL 17 User's Manual*, University of Torino, 2017.

(48) Perdew, J. P.; Burke, K.; Ernzerhof, M. Generalized Gradient Approximation Made Simple. *Phys. Rev. Lett.* **1996**, *77*, 3865−3868.

(49) Paier, J.; Hirschl, R.; Marsman, M.; Kresse, G. The Perdew−Burke−Ernzerhof exchange-correlation functional applied to the G2-1 test set using a plane-wave basis set. *J. Chem. Phys.* **2005**, *122*, 234102.

(50) Monkhorst, H. J.; Pack, J. D. Special points for Brillouin-zone integrations. *Phys. Rev. B* **1976**, *13*, 5188−5192.

(51) Grimme, S. Semiempirical GGA-type density functional constructed with a long-range dispersion correction. *J. Comput. Chem.* **2006**, *27*, 1787−1799.

(52) Moellmann, J.; Grimme, S. DFT-D3 Study of Some Molecular Crystals. *J. Phys. Chem. C* **2014**, *118*, 7615−7621.

(53) Matsuda, Y.; Tahir-Kheli, J.; Goddard, W. A., III Definitive Band Gaps for Single-Wall Carbon Nanotubes. *J. Phys. Chem. Lett.* **2010**, *1*, 2946−2950.

(54) *Jmol: an open-source Java viewer for chemical structures in 3D.* http://www.jmol.org/

(55) McMahon, B.; Hanson, R. M. A toolkit for publishing enhanced figures. *J. Appl. Crystallogr.* **2008**, *41*, 811−814.

(56) Müller, U. Die Symmetrie von Spiralketten. *Acta Crystallogr., Sect. B: Struct. Sci., Cryst. Eng. Mater.* **2017**, *73*, 443−452.

(57) Nilges, T.; Pfister, D.; Ott, C.; Schäfer, K.; Baumgartner, M.; Weihrich, R. Inorganic Semiconducting Compounds. EP Patent EP3319903 B1, 2016.

(58) Lange, S.; Bawohl, M.; Weihrich, R.; Nilges, T. Mineralization routes to polyphosphides: Cu$_2$P$_{20}$ and Cu$_5$InP$_{16}$. *Angew. Chem., Int. Ed.* **2008**, *47*, 5654−5657.

(59) Nilges, T.; Kersting, M.; Pfeifer, T. A fast low-pressure transport route to large black phosphorus single crystals. *J. Solid State Chem.* **2008**, *181*, 1707−1711.

(60) Osters, O.; Nilges, T.; Bachhuber, F.; Pielnhofer, F.; Weihrich, R.; Schöneich, M.; Schmidt, P. Synthesis and Identification of Metastable Compounds: Black Arsenic-Science or Fiction? *Angew. Chem., Int. Ed.* **2012**, *51*, 2994−2997.

(61) Nilges, T.; Osters, O.; Schmidt, P.; Schöneich, M.; Weihrich, R.; Bachhuber, F. Untersuchungen zur Bildung von schwarzem Arsen. *Z. Anorg. Allg. Chem.* **2010**, *636*, 2046.

(62) Díaz-Fernández, A.; Chico, L.; González, J. W.; Domínguez-Adame, F. Tuning the Fermi velocity in Dirac materials with an electric field. *Sci. Rep.* **2017**, *7*, 8058.

(63) Ruggiero, M. T.; Erba, A.; Orlando, R.; Korter, T. M. Origins of contrasting copper coordination geometries in crystalline copper sulfate pentahydrate. *Phys. Chem. Chem. Phys.* **2015**, *17*, 31023−31029.

(64) Bachhuber, F.; von Appen, J.; Dronskowski, R.; Schmidt, P.; Nilges, T.; Pfitzner, A.; Weihrich, R. The Extended Stability Range of Phosphorus Allotropes. *Angew. Chem., Int. Ed.* **2014**, *53*, 11629−11633.

(65) Bachhuber, F.; von Appen, J.; Dronskowski, R.; Schmidt, P.; Nilges, T.; Pfitzner, A.; Weihrich, R. Van der Waals interactions in selected allotropes of phosphorus. *Z. Krist.-Cryst. Mater.* **2015**, *230*, 107−115.

(66) Zhou, X.; Park, J.-Y.; Huang, S.; Liu, J.; McEuen, P. L. Band Structure, Phonon Scattering, and the Performance Limit of Single-Walled Carbon Nanotube Transistors. *Phys. Rev. Lett.* **2005**, *95*, 146805.

(67) Liu, D.; Tománek, D. Catalytic formation of narrow Nb nanowires inside carbon nanotubes. *Carbon* **2020**, *159*, 195−200.

(68) Terrones, M.; Jorio, A.; Endo, M.; Rao, A. M.; Kim, Y. A.; Hayashi, T.; Terrones, H.; Charlier, J. C.; Dresselhaus, G.; Dresselhaus, M. S. New direction in nanotube science. *Mater. Today* **2004**, *7*, 30−45.

(69) Chen, X.; Shen, Q.; Li, Z.; Wan, W.; Chen, J.; Zhang, J. Metal-Free H_2 Activation for Highly Selective Hydrogenation of Nitro-aromatics Using Phosphorus-Doped Carbon Nanotubes. *ACS Appl. Mater. Interfaces* **2019**, *12*, 654−666.

(70) Yeung, C. S.; Wang, Y. A. Lewis Acidity of Pt-Doped Buckybowls, Fullerenes, and Single-Walled Carbon Nanotubes. *J. Phys. Chem. C* **2011**, *115*, 7153−7163.

(71) Meng, L.; Fu, C.; Lu, Q. Advanced technology for functionalization of carbon nanotubes. *Prog. Nat. Sci.* **2009**, *19*, 801−810.

(72) Zhao, J.; Park, H.; Han, J.; Lu, J. P. Electronic Properties of Carbon Nanotubes with Covalent Sidewall Functionalization. *J. Phys. Chem. B* **2004**, *108*, 4227−4230.

(73) Lu, X.; Chen, Z. Curved Pi-Conjugation, Aromaticity, and the Related Chemistry of Small Fullerenes ($<C_{60}$) and Single-Walled Carbon Nanotubes. *Chem. Rev.* **2005**, *105*, 3643−3696.

Supplementary Information

Towards Atomic-Scale Inorganic Double Helices via Carbon Nanotube Matrices – Induction of Chirality to Carbon Nanotubes

Markus R. P. Pielmeier[a], Antti J. Karttunen[b], Tom Nilges[a],*

a) Technical University of Munich, Lichtenbergstraße 4, 85748 Garching (Germany).

b) Department of Chemistry and Materials Science, Aalto University, P.O. Box 16100, FI-00076 Aalto (Finland).

1. Total Energies for SnIP@CNT hybrids and crystallographic data of SnIP

In SnIP two different enantiomeric rods appear as a racemic mixture arranged in a pseudo-hexagonal rod-packing along the *a*-axis. SnIP crystallizes monoclinically, in space group *P*2/*c* (No. 13). It contains *Z*=14 formula units in the unit cell, with lattice parameters of *a* = 7.934 Å, *b* = 9.802 Å, *c* = 18.439 Å and *β* = 110.06°.
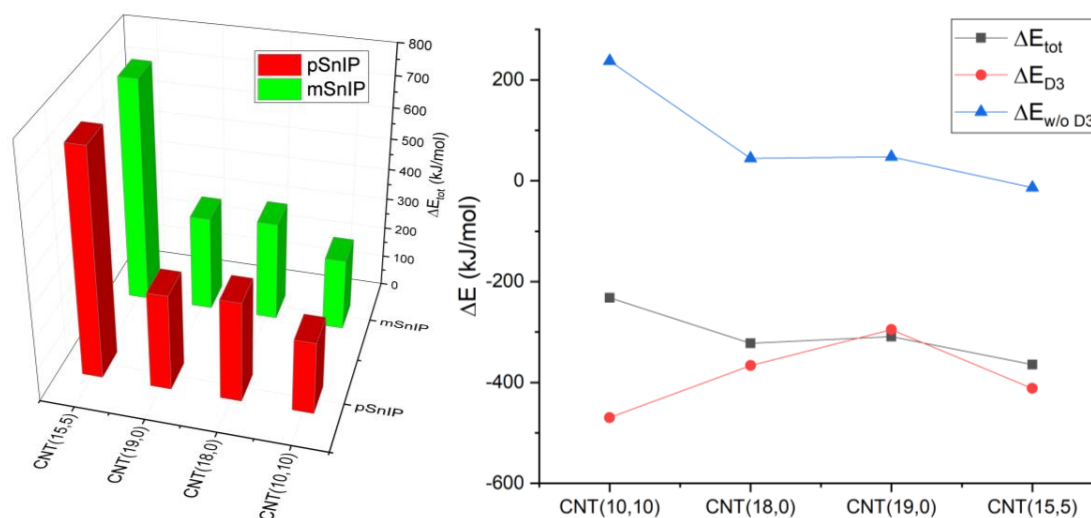
Figure S 1. Left: Total energies diagram of hybrids compared to the separate components. Four different CNT are investigated as matrices for M- and P-SnIP double helices. CNT(15,5) hybrid has doubled unit cell length. Right: Plot of total energy (E_{tot}) vs dispersion correction energy (E_{D3}) vs total energy without a dispersion correction ($E_{w/oD3}$) showing that there is neither pure dispersion nor pure covalency present. The energy values are normalized for one SnIP repetition unit.

The right hand side of Figure S 1 shows the plot of the total energy vs the empirical dispersion correction and the total energy without dispersion correction. The general concordance between the total energy and the total energy without dispersion correction is revealing of a general covalency in the system, but it is also evident, that dispersion plays an important role for these hybrids.

Table S 1. Total energies table per SnIP strand repetition unit with Grimme-D3 dispersion correction (D3) using geometry-optimized data.

CNT (n,m)	E_{tot} SnIP@CNT	E_{tot} CNT	E_{tot} SnIP	ΔE_{tot}
M-helix	(a.u.)	(a.u.)	(a.u.)	(kJ/mol)
10,10	-10524.43011	-4565.62497		-231.93
18,0	-11437.60480	-5478.76526	-5958.71679	-322.22
19,0	-11742.00085	-5783.16642		-308.81
15,5	-21809.93431	-9892.22305	-11917.43358	-364.45
P-helix				
10,10	-10524.43016	-4565.62497		-232.08
18,0	-11437.60476	-5478.76526	-5958.71678	-322.14
19,0	-11742.00073	-5783.16642		-308.52
15,5	-21809.93407	-9892.22305	-11917.43356	-364.16

Table S 2. Total energies table per SnIP strand repetition unit without dispersion (calculated as a single point calculation, sp) correction (D3 correction) ΔE_{tot} (D3 – sp) for different SnIP@CNT hybrids and using geometry-optimized data in all cases.

CNT (n,m)	E_{tot} SnIP@CNT	E_{tot} CNT	E_{tot} SnIP	ΔE_{tot}	ΔE_{tot} (D3 - sp)
M-helix	(a.u.)	(a.u.)	(a.u.)	(kJ/mol)	(kJ/mol)
10,10	-10523.67142	-4565.21960		237.65	-469.58
18,0	-11436.81323	-5478.28778	-5958.54235	44.36	-366.58
19,0	-11741.21330	-5782.66571		-13.75	-295.06
15,5	-21808.40830	-9891.35975	-11917.08470	47.45	-411.90
P-helix					
10,10	-10523.67141	-4565.21960		237.65	-469.73
18,0	-11436.81323	-5478.28778	-5958.54235	44.36	-366.50
19,0	-11741.21320	-5782.66571		-13.47	-295.05
15,5	-21808.40555	-9891.35975	-11917.08470	51.06	-415.22

Table S 3. Geometrical parameters of SnIP@CNT hybrids derived from DFT data after geometry optimization. All distances and angles are given in Angstrom (Å) and degrees (°), respectively. For experimental data the standard deviations are smaller than the last given digit.

	P-SnIP			
	@ CNT (10,10)	@ CNT (15,5)	@ CNT (18,0)	@ CNT (19,0)
P-P	2.21	2.22	2.26	2.25-2.26
P-P-P	93.3	94.4-94.5	97.8	97.8
Sn-I	3.08	3.12-3.13	3.09-3.10	3.14-3.15
I-Sn-I	147.8-148.0	151.0-151.1	153.2-153.4	155.7-155.8
Sn-I-Sn	110.9-111.1	107.9	106.1-106.2	103.6-103.7
Sn-P	2.65	2.68	2.74	2.75
I-C	3.20-3.26	3.39-3.42	3.38-3.49	3.63-3.72
C-C	1.42-1.43	1.42-1.43	1.42-1.43	1.42
C-C-C	119.3-120.2	119.4-120.1	119.4-120.1	119.3-120.0

2. Density of states for SnIP@CNT hybrids
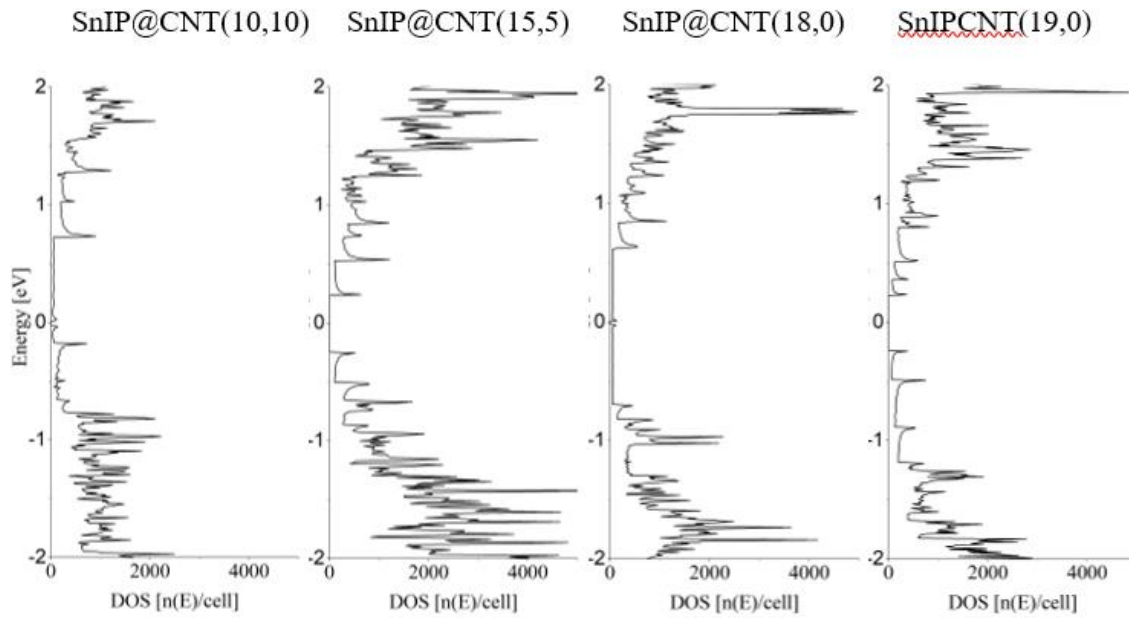
Figure S 2. Density of states schemes for different SnIP@CNT hybrids.

3. Crystal Orbital Hamilton Population for SnIP@CNT hybrids

COHP representations derived from the variational Hamiltonian matrix. Calculations were performed with geometry optimized data.

SnIP@CNT (18,0)   SnIP@CNT (19,0)

Figure S 3a. Crystal Orbital Hamilton Population plotted for the most interesting interactions of atomic species next to the corresponding DOS. In this plot negative values mean bonding and positive values correspond to antibonding.

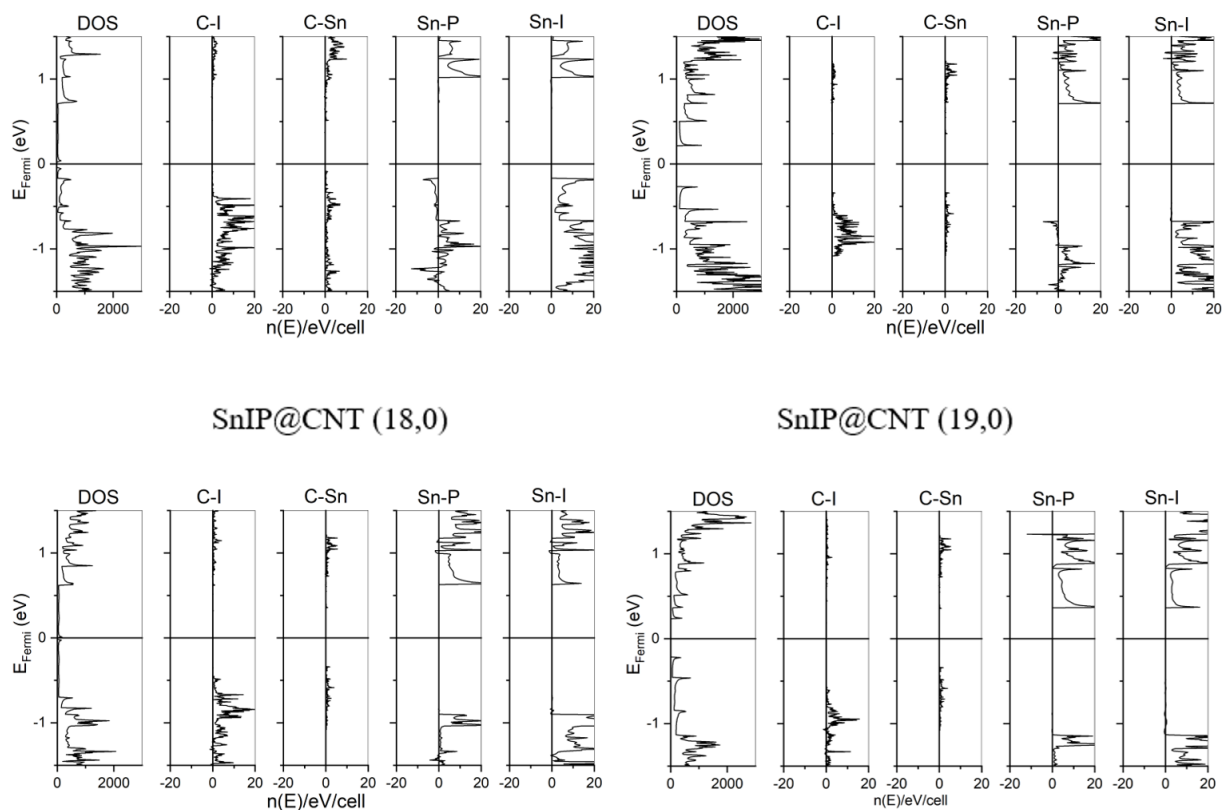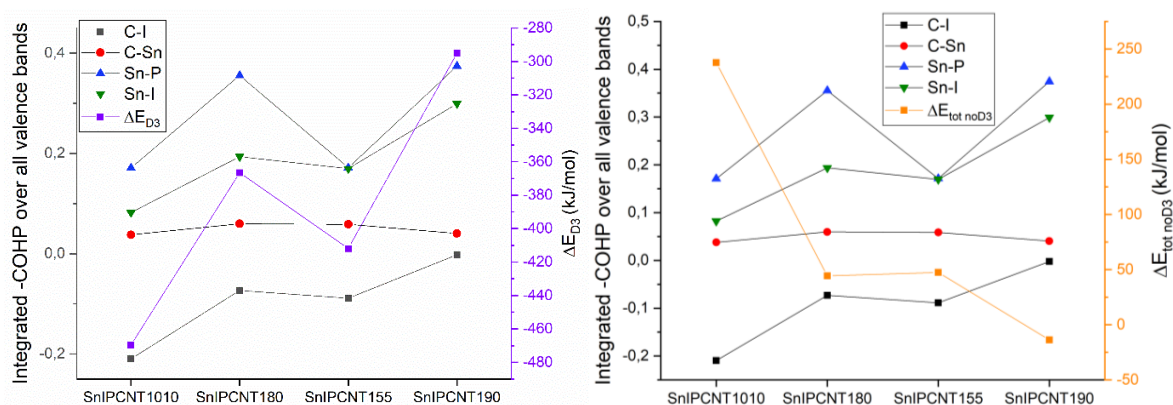**Figure S 3b.** Integrated negative COHPs for the whole valence plotted with the empirical dispersion correction energy (ΔE_{D3}, left) and the total energy without dispersion energy ($\Delta E_{Dtot\ noD3}$, right). As we used the negative COHP here, positive values correspond to bonding and negative values mean antibonding.

The integrated negative COHP in Figure 3b are used to search for mainly dispersive or mainly covalent interactions between important atom groups. The general form of the purple graph on the left can be found in the Sn-P interactions (blue), which is in perfect agreement with experimental data. There seems to be no interaction pictured, that can be named as mainly convalent, as the orange graph on the right is quite different than all others. As all interactions sum up to a positive number (except C-I), the order of stability of the bonds between atoms is Sn-P as the most stable, then Sn-I, C-Sn and finally C-I.

4. Representation of selected vibrational modes of SnIP

All vibrations are given as additional videos with the respective filename. The vibration was scaled consistently with the factor 5 in the Jmol visualization interface.
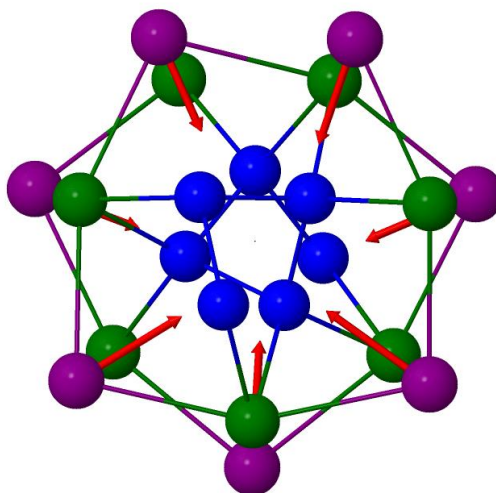

Figure S 4. Iodine breathing mode (view along repetition axis) pSnIP1D80I.mp4.
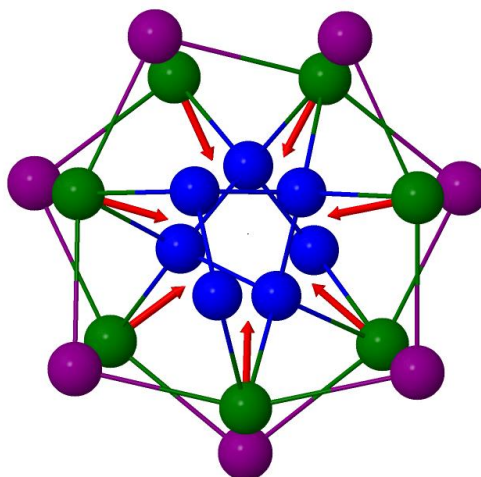

Figure S 5. Tin breathing mode (view along repetition axis) pSnIP1D132Sn.mp4.
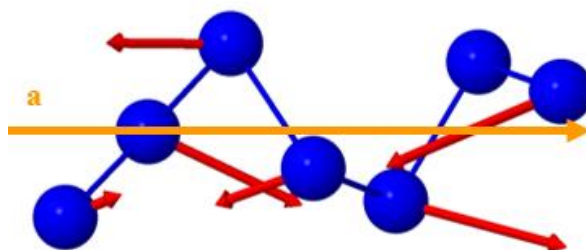
Figure S 6. Phosphorus stretching mode (view along b axis without the SnI helix)
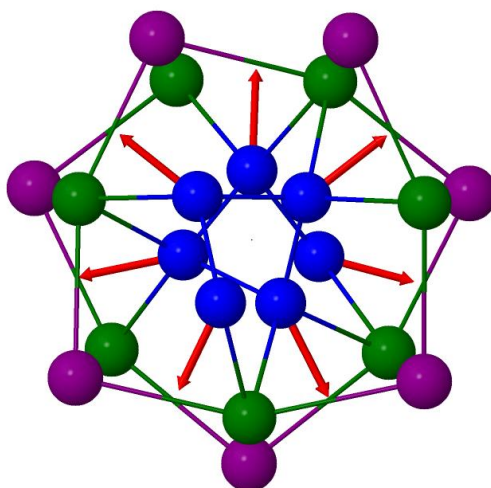
pSnIP1D350P.mp4.

Figure S 7. Phosphorus breathing mode (view along repetition axis) pSnIP1D437P.mp4.

5. Formation mechanism of SnIP in CNT

Based on a successful incorporation of double helical Se chain fragments in CNT we predict a plausible formation mechanism for SnIP in a suitable CNT. Assuming comparable structural, electronic and mechanical properties for a Se and SnIP double helix, that are the flexibility due to the prominent and comparable structure and its surface determination by lone pairs, we believe that Se double helices are a good model system to be used for this discussion.

For the Se@CNT hybrid reported (Citation 8 in main article) also attractive but very weak electronic interactions between the guest and the host were found, nevertheless the hybrid was successfully synthesized. An interesting formation mechanism was postulated for the Se double helix inside the CNT, where the authors could show, that the realized Se double helix is compressed inside the matrix compared to their calculations. The incorporated Se double helix showed a much smaller diameter than a free-standing one after structure optimization and without significant compression caused by an external force. Therefore, the authors concluded that the formation of the double helix occurred within the CNT by reorganization of Se fragments or even atoms after encapsulation. The formation of the double helices can be regarded as an energetic compromise between minimizing the Se-CNT repulsion and the radial compression energy of the double-helix. Coming back to the title compounds the question now arises, if the formation of SnIP double helices might also be realized via short fragments and might be accelerated by compression of the surrounding matrix. If we now go back to SnIP as a potential host, the synthesis of bulk-SnIP is realized by a vapor transport mechanism, which might be very beneficial for a formation within the confined space of a suitable CNT. All components needed for the synthesis, that are SnI_2 and P_4, are highly volatile and available under suitable synthesis conditions with reasonable partial pressures (See Cit. 18 and 19 in main article). We predict, that SnIP double helices will

form in a comparable mechanism than observed for the selenium case, when suitable CNTs are applied for the reaction. At least the transport of molecular components into the CNT is likely. In our calculations we also verified the effect of compression (and excess space) of the CNT matrix to SnIP as a driving force for the double helix formation within the CNT by using much smaller (and larger) diameters of the CNTs during our investigations. For instance, a (8,8) CNT with a diameter of 11.0 Å or a (25,0) CNT with 19.8 Å were also investigated. It was not possible to compress a SnIP double helix (diameter of a free-standing SnIP double helix is 9.8 Å) to fit them into a CNT with significantly smaller diameters than the ones we reported in Table 1. If more space is available like in the case of a (25,0) CNT, a non-distorted SnIP double helix is attached to a certain area of the CNT without significant differences compared to a free standing one. Therefore, we believe that compression of the host matrix will not play a significant role and deformation of the SnIP double helix will not occur during the formation of SnIP inside CNTs.

3.3 Nanotube Matrices for flexible SnIP Nanowires

Markus R. P. Pielmeier[a], Annabelle Degg[a], Kathrin Vosseler[a] and Tom Nilges[a]

[a]Technical University of Munich, Department for Chemistry, Lichtenbergstraße 4, 85748 Garching bei München, Germany

This project is a subsequent work to 3.2, in which interesting 2D materials were rolled-up to nanotubes and tested as matrix for single strand SnIP formation. The chosen materials were hot topics in literature and exhibit several thinkable features for a better SnIP stabilization. Nanotubes were generated from MoS_2, P_{grey}, P_{black}, C_3N_4, C_6N_8 and hBN. The focus was shifted from purely energetic considerations to a more detailed analysis of the bonding situation around the Fermi level between matrix and host using the COHP method. Besides the calculated details of the hybrids, a first core-shell particle formation in the SnIP@hBN system was reported.

For better comparison to the previous work, the SnIP@CNT (10,10) hybrid was analyzed in the same way. It shows hardly any bonding states near the Fermi level between outer helix and matrix, but still shows a gain in total energy of 232 kJ/mol. In the COHP of the corrugated, electron-rich interaction area in the SnIP@MoS_2 hybrid were mainly antibonding states between S and I and consequently the total energy gain is the second lowest with 116 kJ/mol. With both phosphorus modifications the hybrids showed a significant number of bonding states between matrix and outer helix, but surprisingly SnIP@P_{grey} had the smallest (109 kJ/mol) and SnIP@P_{black} hybrid had the largest gain (328 kJ/mol) in total energy. There already exists a work about a water splitting hybrid of SnIP and carbon nitride[98]. Here, the melamine-based C_3N_4 and the tri-s-triazine-based C_6N_8 modifications, which both show the known corrugation also in the nanotube configuration, were examined[99]. Even though the matrix of the SnIP@C_6N_8 hybrid is achiral, the M-enantiomer is energetically favored by 31 kJ/mol compared to the P-enantiomer. A differential COHP shows, that this discrepancy is located primarily in the N-I interactions below the Fermi level. The SnIP@hBN hybrid also presents a low number of states altogether in the proximity, but even more so above the Fermi level, which still results in a gain in total energy of 202 kJ/mol. First results for core-shell particles of this composition are presented with experimental data of Raman, DR-UVVis and TEM images.

Author contributions: M. R. P. P. optimized all structures in the framework of DFT, interpreted the vibrational analysis, investigated the electronic structure and depicted the results. K. V. under the supervision of A. D. synthesized the SnIP@hBN hybrid and conducted all examinations thereof. M. R. P. P., A. D., K. V. and T. N. were involved in discussing the results as well as writing and revising the manuscript.

Article

Nanotube Matrices for Flexible SnIP Nanowires

Markus R. P. Pielmeier, Annabelle Degg, Kathrin Vosseler, and Tom Nilges*

Cite This: https://doi.org/10.1021/acs.jpcc.2c03017

Read Online

ACCESS | Metrics & More | Article Recommendations | SI Supporting Information

ABSTRACT: A detailed density functional theory (DFT) study on 1D-SnIP@2D-material hybrids was conducted. Selected two-dimensional (2D) materials like carbon nanotubes (CNTs), MoS_2, phosphorus allotropes (gray and black P), carbon nitrides, and boron nitride were tested as potential 2D hosts or matrices for a highly flexible, pseudo one-dimensional semiconductor SnIP. For a matrix, we selected sheets of the 2D materials rolled-up to nanotubes of 13.1 to 13.8 Å in diameter to accommodate one enantiomeric form of double helical SnIP. SnIP, an atomic-scale inorganic double helix compound, is composed of a racemic mixture of M- and P-double helices that form a pseudo-hexagonal rod packing in the bulk phase. Hybrid materials investigated in this study were classified based on total energy, the internal diameter of the matrix, and bonding interactions. Less-probable and most-probable hybrids were identified. With the hybrid SnIP@C_6N_8 (8,4), the first example was identified, which seems to allow separation of the M- and P-SnIP enantiomers due to significant differences in bonding interactions and overall fit. Differential crystal orbital Hamilton population analysis shows clear preference of M-SnIP over P-SnIP with a 31 kJ/mol stabilization in total energy for M-SnIP@C_6N_8. A vibrational mode analysis of all hybrids illustrates that the length of the propagation vector of the SnIP double helix directly correlates with a red shift of the SnIP phosphorus modes. As a proof of principle, a core−shell particle consisting of SnIP and hBN was successfully prepared and investigated.
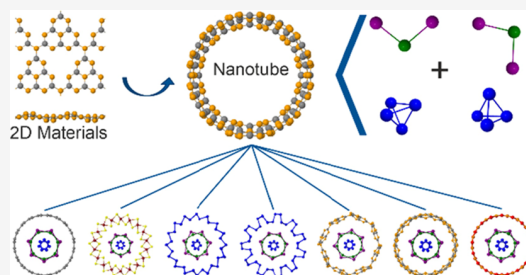
■ INTRODUCTION

For many years, the double helix structure is well known due to its discovery in the human deoxyribonucleic acid (DNA). However, in recent years, this structural motif has gained a new boost of interest in the inorganic chemistry community due to its exceptional structural features, intriguing physical properties, and stereochemistry. Nowadays, the scientific interest is not limited to stable compounds like SnIP,[1−3] but it also treads in the fields of metastable compounds, reaction mechanisms, and structure prediction.[4−9] The possibilities within the framework of density functional theory (DFT) to contribute to materials development and optimization are continuously increasing.[10−15] Therein, the formation of one-dimensional (1D) structures with tunable properties can be predicted even before a synthesis route is established and evaluated. This resource efficient and saving procedure, which avoids a considerable amount of lab work, functions well with any quasi 1D nanotube (e.g., carbon nanotubes) acting as a matrix and arbitrary units that are added as guests (e.g., white phosphorus).[16] The results are sometimes surprising sub-structure motifs (e.g., a selenium double helix inside a double walled carbon nanotube),[17] which could not be witnessed before. Quantum mechanical first-principles calculations also allow detailed investigations on the properties of intriguing composite materials that could easily be overlooked otherwise (e.g., self-healing in the Li_nP_n double helix).[18] Even though inorganic helices are showing interesting properties, they are

challenging candidates to be synthesized and are therefore extremely rare to date. The encapsulation of metals and semiconductors like phosphorus, selenium, or polymers by hosts like nanotubes is not only gaining interest in academic research but also yields very efficient battery materials.[19,20] Very promising candidates for battery research can also be found in the huge field of two-dimensional (2D) materials (e.g., phosphorus allotropes,[21−23] transition metal dichalcogenides,[24] and MXenes[25]). Intensive research is conducted to verify possible additional applications and to address numerous conceivable 2D material classes like MXenes.[25,26] Combining the intriguing properties of 1D structures like SnIP with well-known 2D sheets to achieve core−shell particles (1D@2D) already delivered intriguing results.[7,27]

In 2016, the first inorganic atomic-scale double helix was published by Pfister and co-workers, featuring a left- (M-SnIP) and right-handed (P-SnIP) helix in the bulk.[1] The unit cell possesses $P2/c$ symmetry (space group No. 13) and comprises one helix of each chirality. It crystallizes in needles with a pseudo-hexagonal arrangement of rods along the a axis in a perfect racemic mixture. For this study, the important lattice parameter is a = 7.934 Å, which corresponds to the only repetition direction in the 1D simulation of a single SnIP

A

strand and is parallel to the propagation direction of the helices. The formation mechanism and stacking motives have been published recently,[8,28] while the effect on intra- and interhelical bonding relations and their influence on each other after hybrid material formation are still somewhat uncertain. Recently, time-resolved terahertz spectroscopy was used to investigate the transient photoconductivity and charge carrier mobility in SnIP.[29] An electron mobility of 280 cm^2 V^{-1} s^{-2} along and a hole mobility of 238 cm^2 V^{-1} s^{-2} perpendicular to the SnIP double helices were detected.

Since its introduction in 1993, crystal orbital Hamilton population (COHP) analysis has been a powerful tool for obtaining energy-resolved visualization of chemical bonding in solids.[30] The recognition of such bond properties in composite materials is of fundamental interest to understand more about their structural arrangement and their existence in reality. Nice examples for the utilization of COHP in solid-state science are, e.g., the chemical bonding in group IV chalcogenides[31] and the mechanistic exploration in Li-rich transition-metal carbodiimides.[32] However, the idea of localized bonds in repeating systems was counterintuitive because solid-state theory focused on metallic structures at first.[33] Nonetheless, there were other methods like the crystal orbital overlap population already pioneering in this domain with obvious drawbacks, for instance the heavy basis set dependency.[34] Today, there are many compounds that cannot be categorized with classic concepts (e.g., projecting the Zintl formalism[35] on intermetallic phases), which proves the need for a more differentiated view on the bonding circumstances. Especially in cases like SnIP, where minor alterations can significantly influence its formation, the COHP method is suitable to assess the changes in the double helix hybrids.

■ METHODS

Ab initio calculations are carried out using the Crystal17 code[36] and its default settings unless noted otherwise. Due to the size of the studied periodic 1D systems and the low symmetry ($P1$), all optimizations and frequency calculations are performed on the DFT-GGA-level with the Perdew, Burke, and Ernzerhof (PBE) functional.[37] All-electron LCAO basis sets were applied for B, C, N, S, and P, while effective core pseudopotential and LCAO valence basis sets were used for Mo, Sn, and I (the used basis sets are listed in the Supporting Information in the Crystal17 format). Six Monkhorst-Pack-type k-points were used for sampling the reciprocal space (a double-density Gilat net of 12 points was used in the calculation of the Fermi energy).[38] The structures were optimized using Grimme's DFT-D3 dispersion correction scheme as implemented in Crystal17.[39,40] A Fermi smearing of 0.001 Hartree was applied, whenever carbon nanotubes were involved. This yields sufficient accuracy for the identification of crucial changes in the electronic structures of the hybrids, though we are aware that the PBE functional might underestimate the bandgaps.[41] The convergence threshold for the maximum gradient is 0.00045, and for the maximum displacement, it is 0.0018. For the visualization of the structures, the JMOL package was used.[42] The properties (band structure, DOS, COHP, and vibrational analysis) were calculated with the Crystal17 properties code, and the number of k-points was doubled using the NEWK keyword. The plotted densities of states were expanded with 15 Legendre polynomials as implemented in the CRYSTAL software. The graphs were generated with the program Origin, version 2021,

OriginLab Corporation, Northampton, MA, USA. All experimental methods can be found in the Supporting Information in Chapters 5−7.

■ RESULTS AND DISCUSSION

The motivation to investigate different matrices and their capability to accommodate SnIP is originated by the intriguing material properties of SnIP, the formation of effective heterojunctions after combination of different semiconductors, and finally the hope to utilize or induce (pro)chirality during the synthesis process of the hybrids to achieve enantiomer-pure SnIP double helices. In addition, we suppose that this general process can be the nucleus to discover even more feasible nanomaterials by transferring this screening method to other 2D materials. The range of materials used in this work covers the following monolayer-based nanotubes: carbon nanotubes (CNTs), molybdenum disulfide (MoS_2), hexagonal boron nitride (hBN), gray (sometimes called blue in the literature) phosphorus (P_{gray}), black phosphorus (P_{black}), and the two most frequently applied and discussed graphitic carbon nitride entities C_3N_4 and C_6N_8.[43] The effects of different matrices in the 1D@2D or better SnIP@2D material hybrids on electronic density, coverage, morphology, and rigidity of the nanotube encapsulating the double helix should be identified. The nanotubes used in the following hybrid structures show a diameter of 13.1−13.8 Å and have a repetition unit length between 6 and 10 Å. The empty nanotubes cover bandgaps from 0 to 4.95 eV, feature single-atom to few-atom layer (MoS_2) wall structures, and even allow one to explore different vacancy distributions within the graphitic carbon nitride nanotubes, based on the s-triazine (C_3N_4) and the tri-s-triazine (C_6N_8) isomers. In all cases, the matrix is achiral, which we can combine with two enantiomeric forms of SnIP in our calculations. A chiral matrix was not taken into account in this study because we tried to investigate prominent and available state-of-the-art 2D materials, which offer a certain possibility to be reacted or transformed to 1D@2D hybrids in the future. In the case of chiral CNTs, we found no preference of a SnIP enantiomer upon hybrid formation,[28] so in this work, all the discussions hold true for M- and P-SnIP hybrids unless stated otherwise.

SnIP@CNT (10,10). The first hybrid structure SnIP@CNT (10,10) serves as a starting point for comparison and as a connecting segment to our previous work, where we evaluated the total energies of M- and P-SnIP in combination with a hexagonal shell consisting of six double helices and CNTs in the vicinity. It was reported earlier on,[28] that the stabilization energies of carbon nanotubes and SnIP rods were in the same energy range and we aim for more detailed investigations in this field. The total energy aspect is still important for estimating the stacking effect (interpreted as hexagonal shells on a central SnIP rod). However, here we would like to emphasize more on the bonding situation between a single SnIP strand and the nanotubes, in order to comprehend the needs of a bottom-up synthesized flexible nanomaterial containing single double helices. For this, we use the COHP analysis to get a deeper insight into the bonding situation, especially up to the Fermi level. Furthermore, the main interest here is not the stability of the whole system, but the nature and distributions of interactions between the matrix and host, leading to the possibility of profound, chemically reasonable and feasible adjustments. Further information about geometry, basis sets, etc. can be found in the Supporting Information.

Figure 1. (a) Representation of the *M*-SnIP hybrid with CNT (10,10) with view along *a* (left) and *c* (middle) axes. The energy value in the box (d*E*) is the total energy in kJ/mol (right). (b) DOS and -COHP of the SnIP@CNT (10,10) hybrid. Bonding levels to the right, antibonding levels to the left.

Figure 2. (a) Representation of the *M*-SnIP hybrid with MoS_2 (9,9) with view along *a* (left) and *c* (middle) axes. The energy value in the box (d*E*) is the total energy in kJ/mol (right). (b) DOS and -COHP of the SnIP@MoS_2 (9,9) hybrid. Bonding levels to the right, antibonding levels to the left.

The SnIP@CNT (10,10) hybrid, as shown in Figure 1, has a diameter of 13.8 Å and an extensive π-system distributed across the entire nanotube. This feature is probably the reason for its rigidity (no change in bond lengths or angles).
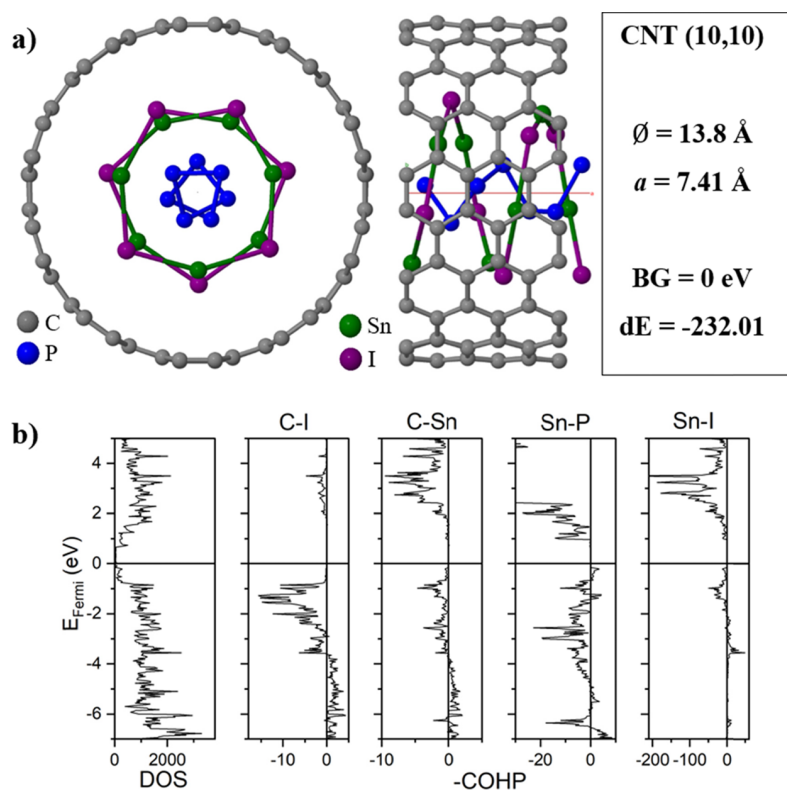
Figure 3. (a) Representation of the *M*-SnIP hybrid with P_{gray} (16,8) with view along *a* (left) and *c* (middle) axes. The energy value in the box (d*E*) is the total energy in kJ/mol (right). (b) DOS and -COHP of the SnIP@P_{gray} (16,8) hybrid. B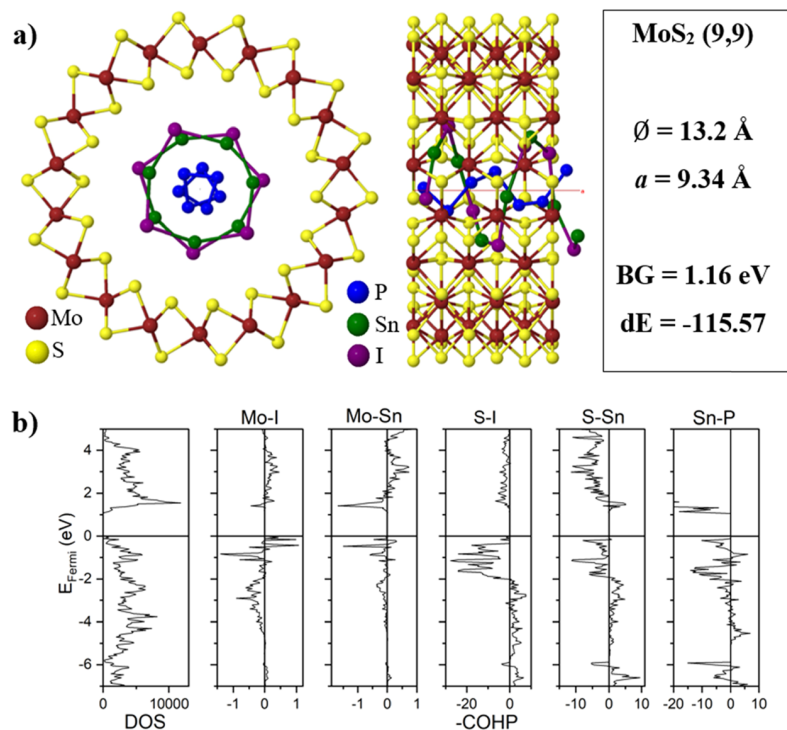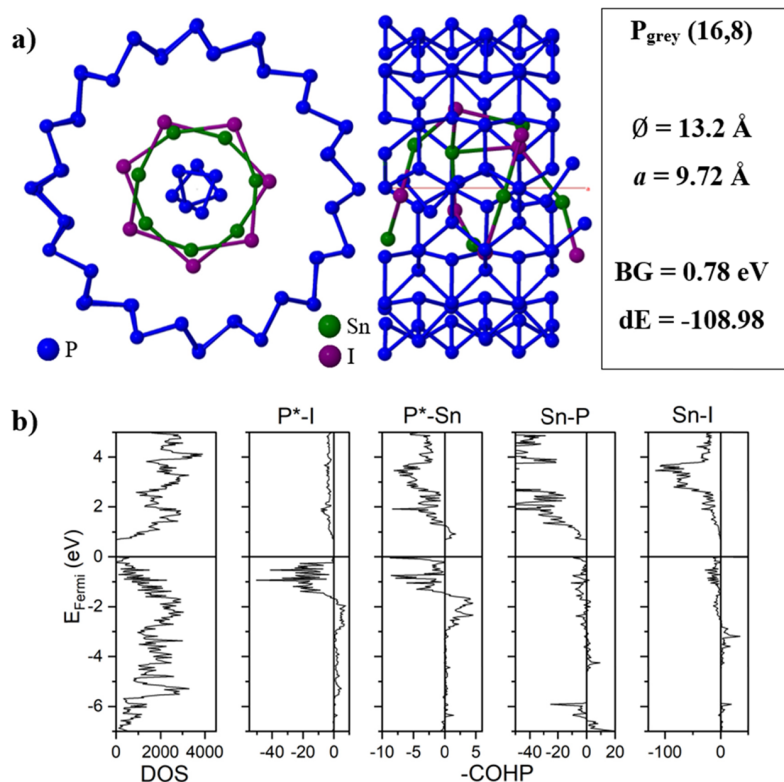onding levels to the right, antibonding levels to the left. P* stands for nanotube phosphorus atoms, while P refers to atoms of the inner helix.

Consequently, SnIP tends to compensate the change of the 1D@2D hybrid *a*-vector (7.41 Å, red line in Figure 1) relative to the stand-alone 1D SnIP vector of 7.84 Å within the hybrid by more acute P−P−P and I−Sn−I angles, shorter Sn−I bond lengths, and a shorter inner to outer helix distance (represented by the Sn−P distance). The rolled-up graphite structure has a spacing of 3.20 Å to the outer helix, and it seems to be the determining factor for the length of the *a*-vector and the diameter.

The bonding situation of this metallic hybrid near the Fermi level (Figure 1b) shows a majority of antibonding states, even though the total energy has a considerable gain compared to the bare components. The amount of bonding states below −3 eV increases significantly. It should be noted that there are exclusively antibonding states above the Fermi level between carbon and the outer helix (C−I and C−Sn). This fact indicates that chemical adaptions like electron doping would not have a significant effect on the hybrid. The integrated -COHP value of this nanotube with the outer SnIP helix (C−Sn/I) is −4.70 eV.

SnIP@MoS₂ (9,9). The first new SnIP@2D hybrid is composed of a rolled-up sheet of MoS_2, yielding the SnIP@MoS_2 (9,9) hybrid (Figure 2a). Due to the heavily bent structure of a MoS_2 sheet in the nanotube, it exhibits more "strain" and a more localized electron density within the inner sulfur substructure than in the outer counterpart. The diameter (13.2 Å) of this hybrid is smaller than that of SnIP@CNT (10,10), while its repetition vector *a* (9.34 Å, red line in Figure 2a) is significantly larger. The phosphorus helix shows peculiarly elongated bonds (2.29 Å) and blunter angles

(101.5), while the outer helix moves farther away (up to 2.87 Å) with shorter Sn−I distances (down to 2.97 Å).

While looking at the -COHPs (Figure 2b), it becomes evident that this nanotube does have some bonding states with the outer SnIP helix close to the Fermi level. However, there are only negative COHP values to be found between S and [SnI]⁺, which is almost completely reversed below ∼ −2 eV. Another substantial number of bonding states is situated between the two helices at about −0.8 to −1.2 eV, which was not as pronounced in the previous case. The large accumulated electron density of the S substructure in the neighborhood to the [SnI]⁺ helix is somehow analogous to the situation in the previous case, where the π-electron system interacts with the SnIP helix. However, the -ICOHP of the MoS_2 nanotube interactions with the outer SnIP helix shows a value of −8.84 eV, which indicates a more antibonding scenario than in the CNT hybrid.

SnIP@Phosphorus. The next two hybrid materials contain phosphorus nanotubes with different surfaces. In general, the change of morphology as the only parameter should provide significant insight into the bonding situation for different element allotrope hybrids. Even though we are aware that the high-pressure phase of phosphorus is unlikely to form a monolayer nanotube, this experiment can contribute to the fundamental understanding of these systems.

SnIP@P_{gray} (16,8). The first hybrid SnIP@P_{gray} (16,8) consists of a nanotube of the high-pressure phase of elemental phosphorus (P_{gray}) and SnIP (Figure 3). This results in a chemically akin inner surface as in the MoS_2 case, where two lone pairs from each atom point toward the SnIP double helix. Though the diameter is almost identical, the *a*-vector is the
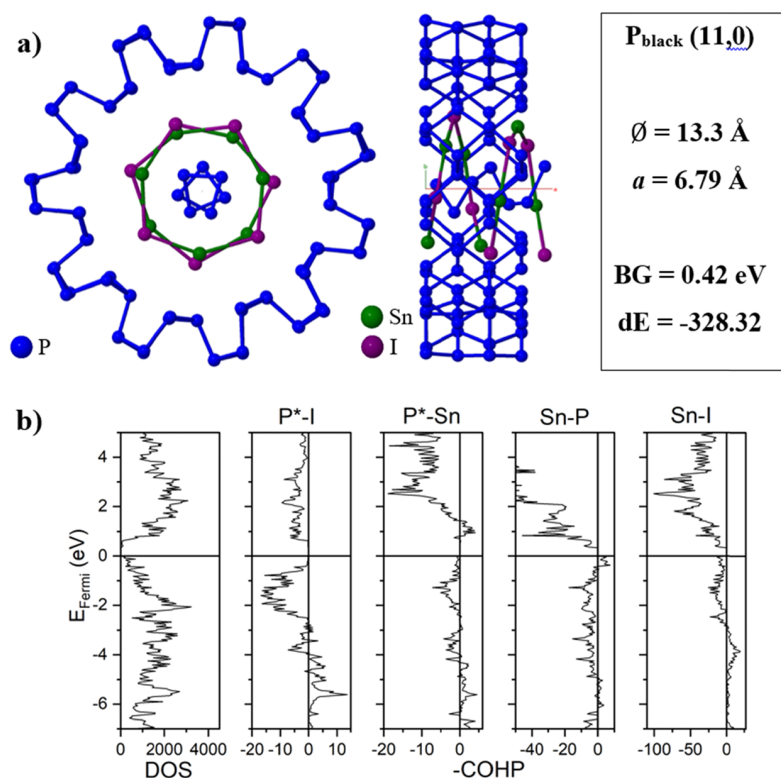
Figure 4. (a) Representation of the *M*-SnIP hybrid with P_{black} (11,0) with view along *a* (left) and *c* (middle) axes. The energy value in the box (d*E*) is the total energy in kJ/mol (right). (b) DOS and -COHP of the SnIP@P_{black} (11,0) hybrid. Bonding levels to the right, antibonding levels to the left. P* stands for nanotube phosphorus atoms, while P refers to atoms of the inner helix.

longest and the total energy difference is the lowest of all tested hybrids. The bond lengths in the helices for this system show some dispersion, e.g., P–P (2.28–2.33 Å) and Sn–I (2.96–3.46 Å). Especially peculiar in this system is the dispersion of angles observed for the inner helix, which stays within a 1° corridor in all other examples but exceeds 9° in this case. While this might be partially attributed to the elongation of the *a*-vector, the influence of phosphorus on the outer helix, more precisely the dative attractive Sn–P interaction within the SnIP double helix and the interaction of Sn with the P* (phosphorus of the nanotube) lone pairs of the outer P_{gray} shell, is the key point here. The confirmation for this hypothesis can likewise be found in the geometric parameters, where the [SnI]$^+$ helix behaves in a contrastable manner and widens the range of its angles (151–156° for I–Sn–I angle). This translates to a somewhat opposing effect to the formerly discussed "pressured" SnIP structure, meaning that the angles at the iodine atoms in the outer shell become more acute. The picture (Figure 3a) shows that iodine atoms of the SnIP outer helix are localized slightly closer to the P_{gray} nanotube relative to the tin atoms. This is perceivable intuitively by the small gaps between the green tin atoms and the violet iodine atoms, which are missing in the former depictions.

After the geometric considerations, the COHP analysis substantiates this finding (Figure 3b). Though right below the Fermi level the states are mainly antibonding, there is a remarkable number of bonding states reaching up to about −1.5 eV between the nanotube and the outer helix (P*–I and P*–Sn). Moreover, this hybrid is the first to show bonding states above the bandgap in the P*–Sn -COHP, a feature that could be beneficial for electron doping experiments. Even though this is undeniably one of the interesting systems when

focusing on the interaction between the nanotube matrix and outer helix, the total energy gain (−109 kJ/mol) is the lowest found in this study. The -ICOHP value between the outer SnIP helix and the nanotube amounts to −10.10 eV for this system.

SnIP@P_{black} (11,0). The second phosphorus-comprising hybrid SnIP@P_{black} (11,0) is composed of a black phosphorus single sheet nanotube, which is corrugated perpendicular to the propagation vector (Figure 4a). Considering the strain after the formation of the matrix nanotube, the bond length of the P−P bonds does overcome 2.31 Å, which is larger than the known values in the literature of 2.24 Å in single layer P_{black}. The bond lengths and angles in the SnIP double helix are comparable to the ones in SnIP@CNT(10,10), but they are distributed over a slightly wider range. Major deviations thereof are the elongated Sn−I distance (3.14–3.26 Å) and the more acute P−P−P angle (90.6–90.8). In contrast to the P_{gray} nanotube, the *a*-vector is considerably shorter and with 6.79 Å the shortest one in all systems evaluated in this work. The diameter (13.3 Å) and bandgap (0.42 eV) show no meaningful difference to the previous case, but the gain in total energy for the P_{black} hybrid (−328.32 kJ/mol) is the largest one found in this study. In the light of this result, a combination of electronic interactions between the double helix and nanotube and the decreasing *a*-vector could go hand in hand for the significant gain in total energy.

The bonding in this hybrid (Figure 4b) shows bonding states of Sn−P right below the Fermi level. While this system is energetically favored, the mainly bonding states turn into antibonding ones in the energy interval between −5 and −2 eV for all interactions. This is a hint to a more complex correlation than we initially anticipated, especially because the -ICOHP

value between the P_{black} nanotube and the SnI helix is −16.35 eV but can obviously still entail a substantial gain in total energy (−328 kJ/mol).

SnIP@Carbonnitride. Two graphitic carbon nitride matrices are investigated in this study[43,44] because the vacancy density within the layer formed either by C_3N_4 or C_6N_8 moieties is different, which can therefore cause a variable attachment to the double helix (Figure 5). We used two
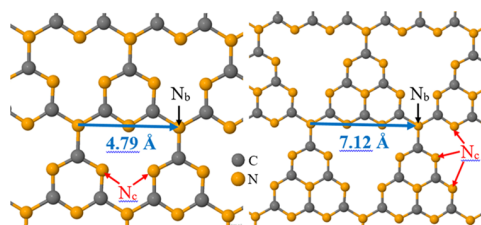

Figure 5. Structure sections of C_3N_4 (left) and C_6N_8 (right) with the respective repetition vectors for comparison. In both pictures, examples for the bridging (N_b) and cyclic (N_c) nitrogen atoms are indicated.

prominent and well-established carbon nitride structure motifs to simulate different vacancy densities and vary the matrix structure accordingly. The vacancy density of a carbon nitride layer can be derived from a graphite layer, alternatively replacing half of the positions of C by N and introducing regular defects on C positions afterward. In a detailed structure study on aforementioned carbon nitride layers, it was found that the lowest energy configuration is a slightly corrugated form instead of a planar one.[45] In the case of hexagonal carbon nitride nanotubes (see Figures 6 and 7), we expect that the

defect distribution within the 2D sheets and therefore the nanotubes can play a certain role.

SnIP@C_3N_4 (9,0). The melamine-based nanotube C_3N_4 (9,0) (Figure 6a) is the best candidate to accommodate SnIP with respect to the *a*-vector (8.00 Å) in this work. The diameter (13.1 Å) of the SnIP@C_3N_4 (9,0) hybrid and the distance to the double helix (3.02 Å) are the smallest. We calculated a band gap of 1.51 eV, which is the biggest one observed in our study. The nanotube in this hybrid displays hardly any change compared to the empty one, where only the angle on the cyclic nitrogen (see N_c in Figure 5) gets a little wider. The double helix in this system is similar to 1D SnIP, but the Sn−I bond length (3.05−3.10 Å) is shorter and the angle I−Sn−I (149.0−151.5) is more acute than that in the freestanding SnIP double helix.

In the SnIP@C_3N_4 (9,0) bonding analysis (Figure 6b), there are few bonding states located between C and Sn below the Fermi level. Apparently, the -COHP in this region is otherwise dominated by antibonding states between −3 and 0 eV. Also, the -ICOHP values between the C_3N_4 nanotube and outer helix sum up to −6.50 eV. This leads to the conclusion that attractive bonding cannot be the driving force for formation. Nevertheless, a gain in total energy of −211 kJ/mol is large for this hybrid, which renders a formation at least feasible. The delamination of SnIP, as far as we observed in our lab, can only be performed down to multi-SnIP bundles of approximately 6−8 shells of attached SnIP double helix strands.[2] We never observed a delamination down to single strands or arrangements with less than the stated number of attached shells. It is likely that the surface to bulk ratio needs to have a certain value due to the optimization of inter strand interactions, which avoids a full delamination to a single strand. In the case

Figure 6. (a) Representation of the *M*-SnIP hybrid with C_3N_4 (9,0) with view along *a* (left) and *c* (middle) axes. The energy value in the box (d*E*) is the total energy in kJ/mol (right). (b) DOS and -COHPs of the SnIP@C_3N_4 (9,0) hybrid. Bonding levels to the right, antibonding levels to the left.
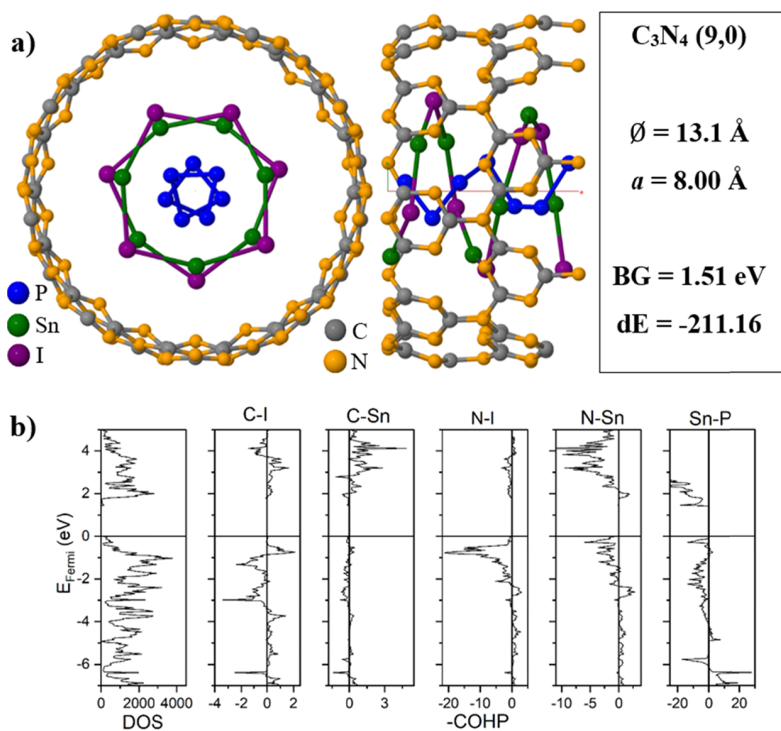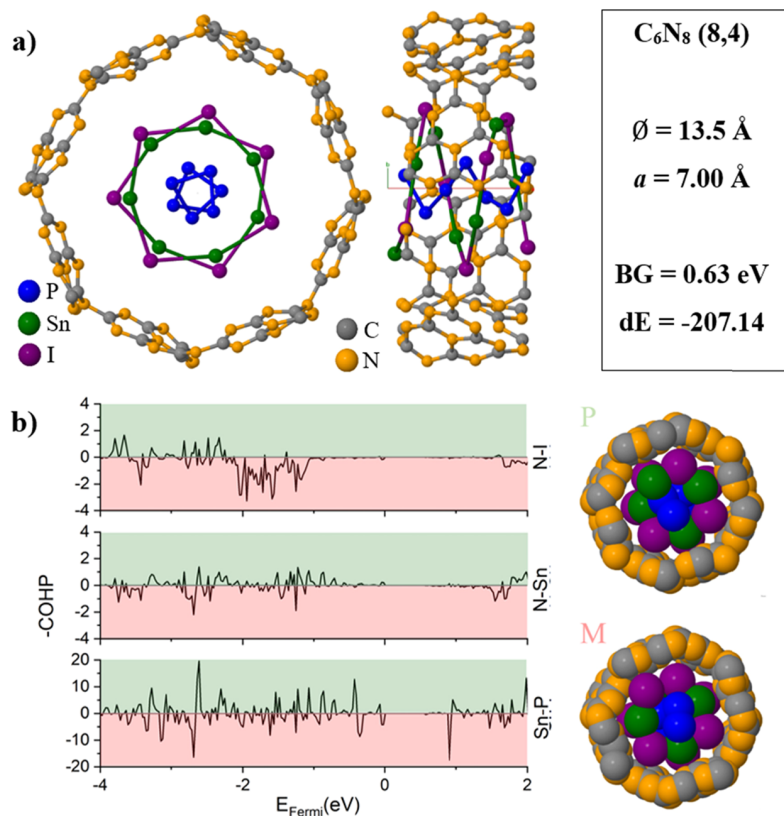
Figure 7. (a) Representation of the *M*-SnIP hybrid with C_6N_8 (8,4) with view along *a* (left) and *c* (middle) axes. The energy value in the box (d*E*) is the total energy in kJ/mol (right). (b) Differential COHPs of *M*- and *P*-SnIP@C_6N_8(8,4) hybrids by subtracting *P*-SnIP COHP values from the *M*-SnIP ones. Positive (or green section) values are an indicator for more bonding or less antibonding states for the *P*-SnIP hybrid, while negative values (or red section) illustrate the same for the *M*-enantiomer. On the right side, the space filling representations of the *P*-(top) and *M*-(bottom)SnIP hybrids are visualized with default vdW radii (provided in a separate file in the Supporting Information).[42,46]

of SnIP@C_3N_4 (9,0), the reason for the large energy gain might be that a bigger quotient of vacancy to coverage in the hybrid is needed. From these facts, we infer that an optimum in energy could be reached by optimizing these two parameters.

A top-down synthesis of a SnIP single strand 2D material hybrid is hindered by the aforementioned aspects (top-down hybrid formation). As a consequence, we see only the formation of larger entities in core−shell particles via delamination and a self-assembly process. For a successful top-down approach, the aforementioned delamination needs to be overcome. In order to realize SnIP hybrids as shown earlier[27] and later on in this manuscript, the formation of SnIP@2D materials is possible only down to 6−8 shells around a central rod. A suitable bottom-up approach might be useful to synthesize a single-strand SnIP@2D hybrid in a gas-phase reaction, where the 2D material is already present and acts as a template. Another option might be the usage of suitable 2D material nanotubes and the formation of SnIP in a gas- or solution-based process. A prerequisite for this is the realization of such 2D material nanotubes.

SnIP@C_6N_8 (8,4). In the tri-*s*-triazine-based nanotube (Figure 7a), the diameter is 13.5 Å, which represents an intermediate range of all examples, and the *a*-vector (7.00 Å) is the second smallest in this study. Overall, the bond lengths stay exactly the same in the hybrid than in the empty nanotube, but the angles in the condensed six-membered ring part become more acute by approximately 1° when the double helix is

inserted. This is attributed to the corrugation of the three condensed rings toward SnIP, which tends to be more bendable than in the melamine-based system. The total energy gain is only slightly (∼4 kJ/mol) inferior to the aforementioned graphitic carbon nitride hybrid for *M*-SnIP. However, in SnIP@C_6N_8 (8,4), for the first time, appears a significant deviation between *P*- (−176 kJ/mol) and *M*-SnIP (−207 kJ/mol) in total energy, which should not originate from a metastable state because the vibrational analysis shows no imaginary frequencies. As usual and applied for all experiments, we cross-checked the outcome by variation of starting conditions. After a closer look, the structure parameters in SnIP, especially in the outer helix and between the helices, seem to differ systematically. The bond lengths and angles for *P*-SnIP in this area are slightly longer and more obtuse compared to the *M*-SnIP hybrid. However, the most evident change can be found in the distance between iodine and the nanotube, which shrinks from 3.73 Å in the *M*-SnIP hybrid to 3.47 Å for the other enantiomer.

As there are larger vacancies in the C_6N_8 nanotube, the hybrids show less number of states altogether (see the Supporting Information, Chapter 3). While the qualitative distribution of the states for both enantiomers shows big resemblances, the number of antibonding N−I states in the *M*-helix is reduced. The fact that there is a significant gain in total energy leads to the assumption that also some kind of encapsulation effect with remarkably low bonding contributions favors the *M*-enantiomer. To illustrate the differences
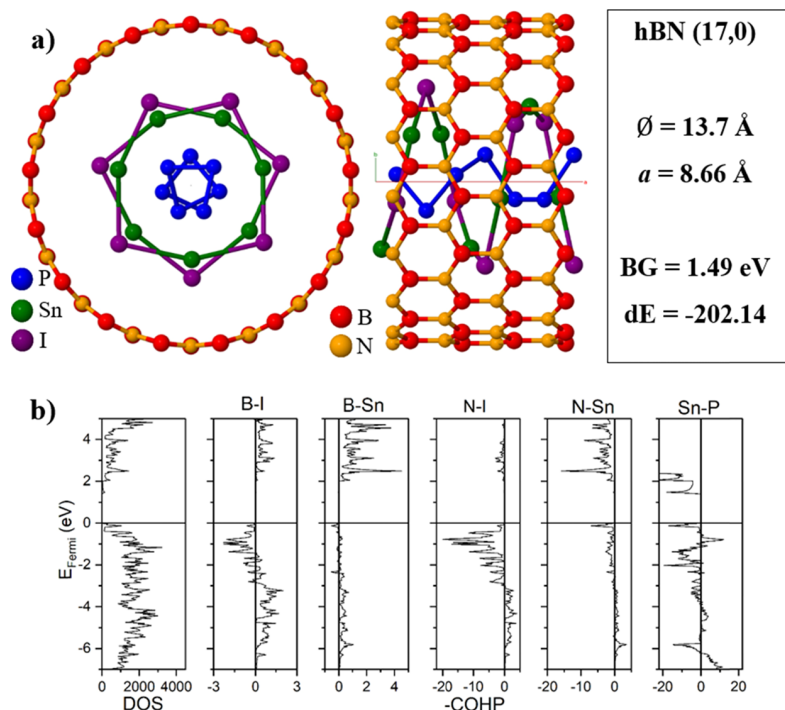
Figure 8. (a) Representation of the *M*-SnIP hybrid with hBN (17,0) with view along *a* (left) and *c* (middle) axes. The energy value in the box (d*E*) is the total energy in kJ/mol (right). (b) DOS and -COHPs of the SnIP@hBN(17,0) hybrid. Bonding levels to the right, antibonding levels to the left.

between the two enantiomers, we calculated a differential COHP by subtraction of the *P*-COHP from the *M*-COHP (Figure 7b). In that case, negative differential COHP values (or red areas in Figure 7b) indicate that more bonding or less antibonding states occur for *M*-SnIP, while positive values (or green areas in Figure 7b) depict the same for *P*-SnIP. Differential COHPs are shown for N−I, N−Sn, and Sn−P. We selected these distances because N−I and N−Sn represent direct matrix−guest contacts, while the Sn−P distances represent outer to inner helix interactions. The most striking feature supporting the preference of *M*-SnIP can be found in the N−I interactions (see the graph in Figure 7b), where *M*-SnIP dominates almost the entire investigated energy range. The N−Sn and Sn−P differential COHPs show no such clear trend or preference for any of the two enantiomers. This translates to a preferred arrangement of iodine atoms in *M*-SnIP relative to the nitrogen atoms of the nanotube, while the rest seems comparable to the *P*-SnIP hybrid. The −ICOHP value for the *M*-SnIP hybrid is 0.85 eV, while it is −0.12 eV for the other chirality, what fits the general picture up until now.

SnIP@hBN (17,0). The final hybrid to be presented here is SnIP@hBN (17,0) featuring a diameter of 13.7 Å and an *a*-axis length of 8.66 Å. The hBN (17,0) nanotube can be obtained from the positions of an isoelectronic CNT, which are occupied by alternating boron and nitrogen atoms. The band gap of the empty nanotube (4.95 eV) is reduced significantly to only 1.49 eV in the hybrid (Figure 8a), which shows a gain in total energy of 202 kJ/mol in comparison to the separated structures. The shortest distance from the outer helix to the hBN (3.2 Å) and the bond lengths and angles in the nanotube lead to the assumption that this nanotube behaves almost as rigid as its carbon predecessor. However, in this hybrid, a conspicuous difference occurs, which can be summarized in the bond length Sn−P (2.75 Å). This relatively large distance

between the inner and outer helices is depicted in elongated P−P and shortened Sn−I bonds, while the obtuse angles P−P−P and Sn−I−Sn become even wider (see the Supporting Information, Table S2).

In the -COHPs (Figure 8b), the formally positively charged boron atoms show quite a few bonding states and also a number of antibonding states near the Fermi level. In the case of nitrogen, there are considerably more repulsive interactions visible. However, there is a huge fraction of binding states in the section below −3 eV. The geometric features include the prolonged Sn−P bond length and hint at a stabilized outer helix. In the -ICOHP analysis, the contributions of B−Sn and B−I are 1.14 and 1.56 eV, but the total value for all interactions between *M*-SnIP and hBN nanotubes sums up to −5.78 eV. As you can see in Table 1, all systems have only one -ICOHP interaction, which pushes the value a great deal to the antibonding (negative) direction. Those are marked with blue

Table 1. Overview of the Contemplated Hybrid Systems, Their -ICOHP Values between the Outer SnIP Helix and Nanotube, and ΔE_{tot} (D3-Corrected)[a]

-ICOHP	C−Sn (eV)	C−I (eV)	N−Sn (eV)	N−I (eV)	ΔE_{tot} (kJ/mol)
SnIP@C3N4	0.31	0.30	−0.27	−6.85	−211.16
M-SnIP@C6N8	0.06	0.48	0.53	−0.22	−207.14
P-SnIP@C6N8	0.12	0.66	0.39	−1.30	−176.16
	B−Sn (eV)	B−I (eV)	N−Sn (eV)	N−I (eV)	
SnIP@hBN	1.14	1.56	−0.78	−7.68	−202.14
	Mo−Sn (eV)	Mo−I (eV)	S−Sn (eV)	S−I (eV)	
SnIP@MoS2	−0.42	−0.73	1.51	−9.20	−115.57
	P*−Sn (eV)	P*−I (eV)			
SnIP@Pblack	−2.27	−14.08			−328.32
SnIP@Pgrey	1.14	−11.25			−108.98
	C−Sn (eV)	C−I (eV)			
SnIP@CNT	1.03	−5.73			−232.01

[a]P* describes phosphorus atoms of the nanotubes. Blue-highlighted values illustrate the main components of antibonding contributions.

in Table 1 and are always situated on the formally anionic iodine.

Attempts to synthesize 1D@2D hybrids are ongoing in our group, and we succeeded in preparing 1D-SnIP@hBN hybrids with more than one single SnIP double helix as self-assembled core—shell particles (see later on) in this study. 1D-SnIP@carbonnitride hybrids were successfully synthesized and tested as water splitting catalysts with a fourfold increase of performance compared with the bare materials.[28] A total energy gain of >150 kJ mol^{-1} as observed for the carbon nitrides and hBN might be a first indicator for the existence of such hybrids. Hence, the most probable candidate for new hybrid formation with SnIP following these results is supposed to be P$_{black}$. Experiments in this direction are currently underway.

Vibrational Analysis. An easy and noninvasive analytic procedure to analyze materials is IR/Raman spectroscopy, especially when there are known vibrational modes for comparison. In Figure 9, all of the *P*-SnIP hybrids together
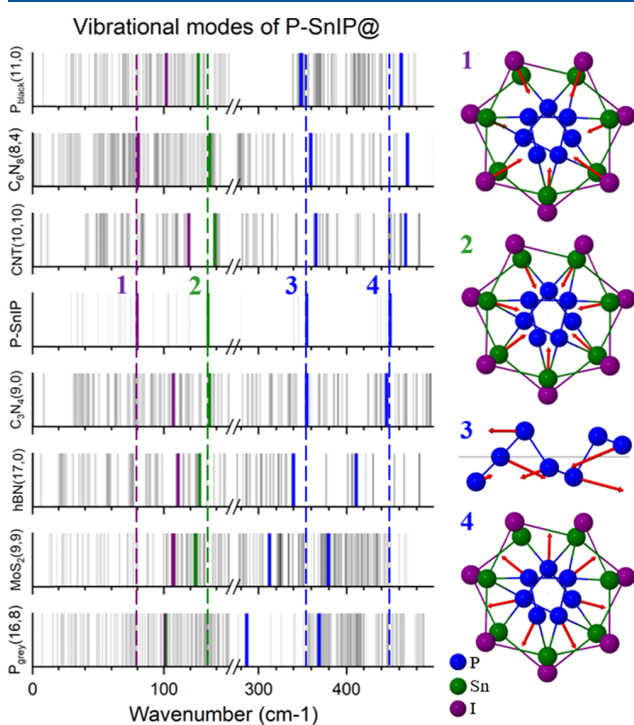

Figure 9. Characteristic vibrational modes of *P*-SnIP and all investigated hybrids sorted by their *a*-vector length (see the Supporting Information, Table S5). Violet (1) and green (2) represent the breathing modes of iodine and tin atoms in the outer helix, respectively. For the inner helix, the stretching (3) and breathing (4) modes are depicted in blue, respectively. All contemplated vibrational modes are illustrated on the right hand side and are equivalent with the ones chosen in our previous work.[28]

with a freestanding *P*-SnIP double helix and the designated modes are shown. Although these calculations might only be a first estimate, they can be used to analyze trends in the materials. The vibrations were chosen according to the investigations of Pfister et al.[2] in the bulk material and compared to the freestanding 1D *P*-SnIP double helix.[28] We identified similar modes representing characteristic breathing and stretching modes for each hybrid, which we marked with

different colors in Figure 9. Each mode is given beside the calculated spectra.

The emphasized mode with the lowest energy in all systems is the iodine-breathing mode (1 in Figure 9), which shifts blue in all cases except for SnIP@C$_6$N$_8$. The iodine atoms are located at the outermost perimeter of the double helix and thus are the first atoms to be influenced by the nanotube electron vicinity. From the formal negative charge of iodine in the [SnI]$^+$ helix and the electron precise hosts, it can be deduced that this influence should be antibonding in most cases. For tin (2 in Figure 9), the effect is reversed, which can be explained by the release of strain in the outer helix and the attraction from the surrounding electron density. When looking at the phosphorus vibrations, a more complex pattern arises, ranging from light blue shifts to deep red shifts. For the stretching mode (3 in Figure 9) of the inner helix, a correlation with the *a*-vector is evident. The elongation in this direction compared to the freestanding SnIP double helix provokes a substantial red shift for the hybrids with hBN, MoS$_2$, and P$_{gray}$. Logically, this also applies to the P-breathing mode (4 in Figure 9) because phosphorus and tin atoms are moving away from each other, which triggers a slight but systematical decrease in the number of interactions. This trend can be reconfirmed qualitatively in the ICOHPs (Table 1), where the antibonding portion rises in the same pattern.

In our previous work, we analyzed the influence of various CNT matrices on SnIP in SnIP@CNT hybrid materials.[28] We varied the size (or diameter) of the CNT and correlated it with the changes in the vibrational spectra. We hypothesized a certain influence of the matrix on the guest, which caused a blue shift of the iodine breathing modes dependent on the diameter of the CNT and a red shift of most of other modes. The interactions in the SnIP@CNT materials resulted in a strain release of the two helices and a slight "pressuring" effect on iodine atoms of the outer helix, which led to a rearrangement (or movement) of atoms and variation of bond lengths in SnIP. Here, the size of the CNT and the Sn—I—Sn angles were identified as the most influencing structure parameters, which caused the spectral answer. In the present study, we tried to keep the diameter of the matrix with 13.1 to 13.8 Å as constant as possible and varied the type of matrix material. This also leads to a completely different electronic situation within the matrix but minimizes the "size" effect as much as possible. Now, the electronic structure will play the dominant role in initiating interactions within the system.

Our present data concerning the phosphorus modes illustrate that the *a*-vector and the shift of modes 3 and 4 in Figure 9 are directly correlated to each other. The larger the *a*-vector is in a given material compared to the vector in the freestanding SnIP strand (7.84 Å), the more red shifted the modes are. This trend is visible in Figure 9, where the hybrids are sorted by their *a*-vector lengths from the longest (P$_{black}$) to shortest (P$_{gray}$). For the I (1 in Figure 9) and Sn (2 in Figure 9) breathing modes, we observe that in most cases a blue shift of the I mode causes a red shift of the Sn mode. Only in the case where almost no interaction between the matrix and the guest occurs, like in SnIP@C$_6$N$_8$ (8,4), we see no effect on the modes. For SnIP@C$_3$N$_4$ (9,0) and SnIP@CNT (10,10), we found almost no effect on the Sn mode but a significant blue shift for I. The two systems, of which one was taken from our previous study, seem to behave equivalent and in accordance to each other. Obviously, the substitution of C by N and the introduction of defects into the matrix seem not to have a

drastic influence on the vibrational spectrum of SnIP, but all modes are slightly red shifted. We interpret this red shift as a certain relaxation of the entire system and a certain energy gain.

More attention is needed for $SnIP@P_{gray}$, where the high number of bonding states can be found between the nanotube and the outer helix. From a geometrical point of view, there is the longest a-vector (9.72 Å) and the maximum distance between inner and outer helices (3.10 Å). Furthermore, the Sn−I and P−P bond lengths and angles reach maximum values in this structure. Heeding the fact that the distance from I of the double helix to P of the matrix (3.25 Å) is rather average compared to the other I−NT distances, the only conclusion explaining its properties is a dominating adaption of the outer helix to the concavities of the matrix structure. The dative bonding in SnIP between the P lone pairs of the inner helix and Sn of the outer one can now also take place between Sn and the matrix itself. This causes a slight but notable rearrangement and reorientation of the $[SnI]^+$ helix, which is more pronounced than in all other examples in this study.

Core−Shell Particles. The $SnIP@C_3N_4(F,Cl)$[27] hybrid is the first example of a 1D-SnIP@2D hybrid material. It showed reasonable good performance in water splitting experiments with an almost fourfold increase of the splitting ability compared with the bare materials. In first attempts to synthesize more of these interesting hybrid materials, we were able to prepare core−shell particles of SnIP and hBN. In Figure 10, we see a representative sample where a SnIP bundle
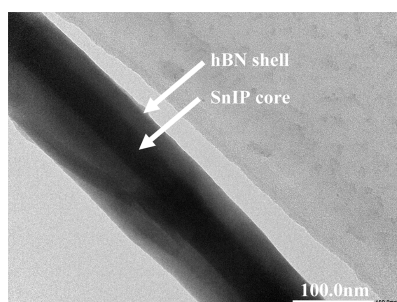

Figure 10. TEM image of the SnIP@hBN 1:240 hybrid at 200,000× magnification, scale bar 100 nm.

is encapsulated by an hBN shell. A diameter of ~30 nm of SnIP is equivalent to ~14−15 shells of SnIP around a central rod. Raman spectra were recorded (see the Supporting Information, Chapter 4), which illustrate the core−shell character of the hybrid. Neither new bands nor a significant shift in Raman modes have been detected, which substantiates the DFT findings and the core−shell particle character.

The experimentally determined band gap of the hybrid changes slightly from 1.80 eV in pristine SnIP[1] to 1.81 eV for the direct bandgap and 1.82 eV for the indirect one. The calculated band gaps of a single 1D-SnIP strand (1.57 eV) and of the hybrid (1.49 eV) are both underestimated, as expected for the PBE functional used in our DFT calculations. Additional measurements and the experimental data are provided in the Supporting Information (Chapters 5−7). In further studies, we intend to measure the water splitting activity of this hybrid in order to evaluate the efficiency of heterojunction formation for this material. The Raman analysis supports our core−shell particle theory with purely ionic/van-der-Waals interactions (no new bonds) between the two

materials and qualitatively implies the correct vibrational modes we predicted for this system.

CONCLUSIONS

Ab initio DFT-based quantum chemical calculations were successfully used to evaluate the electronic and structural parameters, like change in energy, geometry, and bonding situation for hybrids of different 2D materials and pseudo 1D-SnIP. An isotropic pressure-like behavior of the 2D matrix to the 1D guest could be identified, complemented with an anisotropic effect along the SnIP repetition vector and an additional stabilizing feature, originating from the interaction between the nanotube matrix and the outer $[SnI]^+$ helix of SnIP. It should be noted that the last point leads to a delicate equilibrium between the inner helix and nanotube, which should be influenced by, e.g., structural features or electron doping. Furthermore, for the first time, a significant deviation in total energy was found if the two chiral M- and P-SnIP double helices are accommodated in the same matrix. We observed a 31 kJ/mol preference of the M-SnIP enantiomer in the $SnIP@C_6N_8$ (8,4) hybrid. The N−I interactions of the matrix (N) to the outer $[SnI]^+$ helix (I) were identified as the main driving force for this effect. Consequently, the M-SnIP enantiomer fits better to the selected matrix than the counterpart. In the future, a thorough investigation of this phenomenon is planned.

Structure parameters in the SnIP guest, as well as between the matrix and the guest, were subject to brief investigations. The P−P−P angle in SnIP apparently depends heavily on the length of the a-vector and does not seem to be influenced significantly by any interactions arising from embedding the double helix into a matrix. The bond length in the phosphorus helix scatters constantly around ~2.2 Å until the repetition vector gets larger than in freestanding 1D SnIP and reaches a maximum of 2.33 Å in the P_{gray} hybrid. For the outer helix, the interaction with the nanotube, its diameter, and the a-vector of the hybrid collaborate to dictate the result. The largest a-axis (P_{gray} hybrid) can generate the shortest Sn−I distance (2.96 Å), and the smallest one (P_{black} hybrid) produces a bond length in the outer helix of up to 3.26 Å. The longest distance between the nanotube matrix and the double helix guest ($SnIP@C_6N_8$) is attributed to the vacancies of the C_6N_8 nanotube, which is also indicated by the COHP analysis showing a low number of states in this region.

Future projects will focus on the optimization of the 2D materials, which are used as the 2D-matrix for the hybrids. In order to enhance the possibility to realize such 1D@2D hybrids, the material should show more attractive bonding interaction states just below the Fermi level, which might be realized by, e.g., doping. Also choosing other suitable 2D structures like silicon phosphide (SiP) or phosphorus-doped porous carbon nanosheets might lead to a better encapsulation effect.

ASSOCIATED CONTENT

Ⓢⓘ Supporting Information

The Supporting Information is available free of charge at https://pubs.acs.org/doi/10.1021/acs.jpcc.2c03017.

> Total energy data for SnIP@2D material hybrids; geometric data for SnIP@2D material hybrids; COHP of $SnIP@C_6N_8$; Raman data; DR-UV/vis data; and experimental data (PDF)

Used basis sets in the Crystal17 format (TXT)

Further information on geometries (TXT)

Element van der Waals radii used in different packages (XLS)

Vibrational modes (pSnIP1D80I) (MP4)

Vibrational modes (pSnIP1D132Sn) (MP4)

Vibrational modes (pSnIP1D350P) (MP4)

Vibrational modes (pSnIP1D437P) (MP4)

■ AUTHOR INFORMATION

Corresponding Author

Tom Nilges − *Technical University of Munich, Garching 85748, Germany;* ⊙ orcid.org/0000-0003-1415-4265; Email: tom.nilges@tum.de

Authors

Markus R. P. Pielmeier − *Technical University of Munich, Garching 85748, Germany*

Annabelle Degg − *Technical University of Munich, Garching 85748, Germany*

Kathrin Vosseler − *Technical University of Munich, Garching 85748, Germany*

Complete contact information is available at:
https://pubs.acs.org/10.1021/acs.jpcc.2c03017

Author Contributions

M.R.P.P. conducted the DFT investigations under the supervision of T.N. A.D. and K.V. conducted the synthesis and characterization experiments under the supervision of T.N. The manuscript was written by contributions from all authors.

Notes

The authors declare no competing financial interest.

■ REFERENCES

(1) Nilges, T.; Pfister, D.; Ott, C.; Schäfer, K.; Baumgartner, M.; Weihrich, R. Inorganic Semiconducting Compounds patent. WO/2017/008979, 2015.

(2) Pfister, D.; Schäfer, K.; Ott, C.; Gerke, B.; Pöttgen, R.; Janka, O.; Baumgartner, M.; Efimova, A.; Hohmann, A.; Schmidt, P.; Venkatachalam, S.; van Wüllen, L.; Schürmann, U.; Kienle, L.; Duppel, V.; Parzinger, E.; Miller, B.; Becker, J.; Holleitner, A.; Weihrich, R.; Nilges, T. Inorganic Double Helices in Semiconducting SnIP. *Adv. Mater.* **2016**, *28*, 9783−9791.

(3) Utrap, A. X.; Ng, Y.; Nilges, T. A yield-optimized access to double-helical SnIP via a Sn/SnI2 approach. *J. Cryst. Growth* **2017**, *475*, 341−345.

(4) Bachhuber, F.; von Appen, J.; Dronskowski, R.; Schmidt, P.; Nilges, T.; Pfitzner, A.; Weihrich, R. The Extended Stability Range of Phosphorus Allotropes. *Angew. Chem., Int. Ed.* **2014**, *53*, 11629−11633.

(5) Baumgartner, M.; Weihrich, R.; Nilges, T. Inorganic SnIP-Type Double Helices in Main-Group Chemistry. *Chem. − Eur. J.* **2017**, *23*, 6452−6457.

(6) Liu, D.; Tománek, D. Catalytic formation of narrow Nb nanowires inside carbon nanotubes. *Carbon* **2020**, *159*, 195−200.

(7) Ivanov, A. S.; Kar, T.; Boldyrev, A. I. Nanoscale stabilization of zintl compounds: 1D ionic Li-P double helix confined inside a carbon nanotube. *Nanoscale* **2016**, *8*, 3454−3460.

(8) Pielmeier, M. R. P.; Nilges, T. Formation Mechanisms for Phosphorene and SnIP. *Angew. Chem., Int. Ed.* **2021**, *60*, 6816−6823.

(9) Kyrylchuk, A.; Tománek, D. Flow of polar and nonpolar liquids through nanotubes: A computational study. *Phys. Rev. Mater.* **2021**, *5*, No. 076001.

(10) Neumann, M. A.; Leusen, F. J. J.; Kendrick, J. A Major Advance in Crystal Structure Prediction. *Angew. Chem., Int. Ed.* **2008**, *47*, 2427−2430.

(11) Jain, A.; Shin, Y.; Persson, K. A. Computational predictions of energy materials using density functional theory. *Nat. Rev. Mater.* **2016**, *1*, 15004.

(12) Zandi, P.; Ghasemy, E.; Khedri, M.; Rashidi, A.; Maleki, R.; Miri Jahromi, A. Shedding Light on Miniaturized Dialysis Using MXene 2D Materials: A Computational Chemistry Approach. *ACS Omega* **2021**, *6*, 6312−6325.

(13) Lau, V. W.-h.; Klose, D.; Kasap, H.; Podjaski, F.; Pignié, M.-C.; Reisner, E.; Jeschke, G.; Lotsch, B. V. Dark Photocatalysis: Storage of Solar Energy in Carbon Nitride for Time-Delayed Hydrogen Generation. *Angew. Chem., Int. Ed.* **2017**, *56*, 510−514.

(14) Stavila, V.; Li, S.; Dun, C.; Marple, M. A. T.; Mason, H. E.; Snider, J. L.; Reynolds, J. E., III; El Gabaly, F.; Sugar, J. D.; Spataru, C. D.; et al. Defying Thermodynamics: Stabilization of Alane Within Covalent Triazine Frameworks for Reversible Hydrogen Storage. *Angew. Chem., Int. Ed.* **2021**, *60*, 25815−25824.

(15) Banerjee, T.; Podjaski, F.; Kröger, J.; Biswal, B. P.; Lotsch, B. V. Polymer photocatalysts for solar-to-chemical energy conversion. *Nat. Rev. Mater.* **2021**, *6*, 168−190.

(16) Hart, M.; White, E. R.; Chen, J.; McGilvery, C. M.; Pickard, C. J.; Michaelides, A.; Sella, A.; Shaffer, M. S. P.; Salzmann, C. G. Encapsulation and Polymerization of White Phosphorus Inside Single-Wall Carbon Nanotubes. *Angew. Chem., Int. Ed.* **2017**, *56*, 8144−8148.

(17) Fujimori, T.; dos Santos, R. B.; Hayashi, T.; Endo, M.; Kaneko, K.; Tomanek, D. Formation and properties of selenium double-helices inside double-wall carbon nanotubes: experiment and theory. *ACS Nano* **2013**, *7*, 5607−5613.

(18) Jissy, A. K.; Datta, A. What Stabilizes the Li_nP_n Inorganic Double Helices? *J. Phys. Chem. Lett.* **2013**, *4*, 1018−1022.

(19) Balakumar, K.; Kalaiselvi, N. Selenium containing Tube-in-Tube carbon: A one dimensional carbon frame work for selenium cathode in Li-Se battery. *Carbon* **2017**, *112*, 79−90.

(20) Wu, C.-G.; Bein, T. Conducting Polyaniline Filaments in a Mesoporous Channel Host. *Science* **1994**, *264*, 1757−1759.

(21) Li, W.; Yang, Y.; Zhang, G.; Zhang, Y.-W. Ultrafast and Directional Diffusion of Lithium in Phosphorene for High-Performance Lithium-Ion Battery. *Nano Lett.* **2015**, *15*, 1691−1697.

(22) Wang, Y.; He, M.; Ma, S.; Yang, C.; Yu, M.; Yin, G.; Zuo, P. Low-Temperature Solution Synthesis of Black Phosphorus from Red Phosphorus: Crystallization Mechanism and Lithium Ion Battery Applications. *J. Phys. Chem. Lett.* **2020**, *11*, 2708−2716.

(23) Liu, B.; Köpf, M.; Abbas, A. N.; Wang, X.; Guo, Q.; Jia, Y.; Xia, F.; Weihrich, R.; Bachhuber, F.; Pielnhofer, F.; Wang, H.; Dhall, R.; Cronin, S. B.; Ge, M.; Fang, X.; Nilges, T.; Zhou, C. Black Arsenic-Phosphorus: Layered Anisotropic Infrared Semiconductors with Highly Tunable Compositions and Properties. *Adv. Mater.* **2015**, *27*, 4423−4429.

(24) Pallecchi, I.; Manca, N.; Patil, B.; Pellegrino, L.; Marré, D. Review on thermoelectric properties of transition metal dichalcogenides. *Nano Futures* **2020**, *4*, No. 032008.

(25) Zhang, X.; Ma, Z.; Zhao, X.; Tang, Q.; Zhou, Z. Computational studies on structural and electronic properties of functionalized

MXene monolayers and nanotubes. *J. Mater. Chem. A* **2015**, *3*, 4960−4966.

(26) Zhu, J.; Chroneos, A.; Schwingenschlögl, U. Nb-based MXenes for Li-ion battery applications. *Phys. Status Solidi RRL* **2015**, *9*, 726−729.

(27) Ott, C.; Reiter, F.; Baumgartner, M.; Pielmeier, M.; Vogel, A.; Walke, P.; Burger, S.; Ehrenreich, M.; Kieslich, G.; Daisenberger, D.; Armstrong, J.; Thakur, U. K.; Kumar, P.; Chen, S.; Donadio, D.; Walter, L. S.; Weitz, R. T.; Shankar, K.; Nilges, T. Flexible and Ultrasoft Inorganic 1D Semiconductor and Heterostructure Systems Based on SnIP. *Adv. Funct. Mater.* **2019**, *29*, No. 1900233.

(28) Pielmeier, M. R. P.; Karttunen, A. J.; Nilges, T. Toward Atomic-Scale Inorganic Double Helices via Carbon Nanotube Matrices - Induction of Chirality to Carbon Nanotubes. *J. Phys. Chem. C* **2020**, *124*, 13338−13347.

(29) Purschke, D. N.; Pielmeier, M. R. P.; Üzer, E.; Ott, C.; Jensen, C.; Degg, A.; Vogel, A.; Amer, N.; Nilges, T.; Hegmann, F. A. Ultrafast Photoconductivity and Terahertz Vibrational Dynamics in Double-Helix SnIP Nanowires. *Adv. Mater.* **2021**, *33*, No. 2100978.

(30) Dronskowski, R.; Bloechl, P. E. Crystal orbital Hamilton populations (COHP): energy-resolved visualization of chemical bonding in solids based on density-functional calculations. *J. Phys. Chem.* **1993**, *97*, 8617−8624.

(31) Hempelmann, J.; Müller, P. C.; Konze, P. M.; Stoffel, R. P.; Steinberg, S.; Dronskowski, R. Long-Range Forces in Rock-Salt-Type Tellurides and How they Mirror the Underlying Chemical Bonding. *Adv. Mater.* **2021**, *33*, No. 2100163.

(32) Chen, K.; Luo, D.; Dronskowski, R. Exploring the Possible Anionic Redox Mechanism in Li-Rich Transition-Metal Carbodiimides. *J. Phys. Chem. C* **2021**, *125*, 8479−8487.

(33) Steinberg, S.; Dronskowski, R. The Crystal Orbital Hamilton Population (COHP) Method as a Tool to Visualize and Analyze Chemical Bonding in Intermetallic Compounds. *Crystals* **2018**, *8*, 225.

(34) Hoffmann, R. A chemical and theoretical way to look at bonding on surfaces. *Rev. Mod. Phys.* **1988**, *60*, 601−628.

(35) Zintl, E. Intermetallische Verbindungen. *Angew. Chem.* **1939**, *52*, 1−6.

(36) Dovesi, R.; Saunders, V. R.; Roetti, C.; Orlando, R.; Zicovich-Wilson, C. M.; Pascale, F.; Civalleri, B.; Doll, K.; Harrison, N. M.; Bush, I. J.; Arco, D.; Llunel, M.; Causà, M.; Noël, Y.; Maschio, L.; Erba, A.; Rérat, M.; Casassa, S. *CRYSTAL 17 User's Manual*; University of Torino, 2017.

(37) Perdew, J. P.; Burke, K.; Ernzerhof, M. Generalized Gradient Approximation Made Simple. *Phys. Rev. Lett.* **1996**, *77*, 3865−3868.

(38) Monkhorst, H. J.; Pack, J. D. Special points for Brillouin-zone integrations. *Phys. Rev. B* **1976**, *13*, 5188−5192.

(39) Grimme, S. Semiempirical GGA-type density functional constructed with a long-range dispersion correction. *J. Comput. Chem.* **2006**, *27*, 1787−1799.

(40) Moellmann, J.; Grimme, S. DFT-D3 Study of Some Molecular Crystals. *J. Phys. Chem. C* **2014**, *118*, 7615−7621.

(41) Paier, J.; Hirschl, R.; Marsman, M.; Kresse, G. The Perdew-Burke-Ernzerhof exchange-correlation functional applied to the G2-1 test set using a plane-wave basis set. *J. Chem. Phys.* **2005**, *122*, 234102.

(42) Jmol: an open-source Java viewer for chemical structures in 3D. http://www.jmol.org/ (accessed April 19, 2022)

(43) Azofra, L. M.; MacFarlane, D. R.; Sun, C. A DFT study of planar vs. corrugated graphene-like carbon nitride (g-C_3N_4) and its role in the catalytic performance of CO_2 conversion. *Phys. Chem. Chem. Phys.* **2016**, *18*, 18507−18514.

(44) Mukhopadhyay, T. K.; Leherte, L.; Datta, A. Molecular Mechanism for the Self-Supported Synthesis of Graphitic Carbon Nitride from Urea Pyrolysis. *J. Phys. Chem. Lett.* **2021**, *12*, 1396−1406.

(45) Gracia, J.; Kroll, P. Corrugated layered heptazine-based carbon nitride: the lowest energy modifications of C_3N_4 ground state. *J. Mater. Chem.* **2009**, *19*, 3013−3019.

(46) McMahon, B.; Hanson, R. M. A toolkit for publishing enhanced figures. *J. Appl. Crystallogr.* **2008**, *41*, 811−814.

Supplementary Information

Nanotube Matrices for flexible SnIP Nanowires

Markus R. P. Pielmeier[a], Annabelle Degg[a], Kathrin Vosseler[a] Tom Nilges[a,]*

a) Technical University of Munich, Lichtenbergstraße 4, 85748 Garching (Germany).

1. Total Energy Data for SnIP@2D material hybrids

Table S1: DFT calculated D3-corrected total energies of all used self-standing systems, the multiplicity N(SC) used for the hybrid and the corresponding bandgaps.

	E_{tot}(Hartee)	E_{tot}(kJ/mol)	N(SC)	Etot SC(kJ/mol)	Bandgap (eV)
M-SnIP	-5.958717E+03	-1.564461E+07	1	-1.564461E+07	1.55
P-SnIP	-5.958717E+03	-1.564461E+07	1	-1.564461E+07	1.55
hBN(17,0)	-2.708266E+03	-7.110552E+06	2	-1.422110E+07	4.95
C_3N_4(9,0)	-5.993125E+03	-1.573495E+07	1	-1.573495E+07	2.76
C_6N_8(8,4)	-5.327316E+03	-1.398687E+07	1	-1.398687E+07	1.91
P_{grey}(16,8)	-1.091588E+04	-2.865964E+07	3	-8.597892E+07	2.15
P_{black}(11,0)	-1.500935E+04	-3.940704E+07	2	-7.881409E+07	0.85
MoS_2(9,9)	-1.554472E+04	-4.081267E+07	3	-1.224380E+08	1.26
CNT(10,10)	-4.565625E+03	-1.198705E+07	1	-1.198705E+07	0.00

Table S2: DFT calculated D3-corrected total energies of all evaluated hybrids and the corresponding bandgaps.

	E_{tot}(kJ/mol)		dE_{tot}(kJ/mol)		Bandgap (eV)	
Nanotube	*M*-SnIP	*P*-SnIP	*M*-SnIP	*P*-SnIP	*M*-SnIP	*P*-SnIP
hBN(17,0)	-2.986592E+07	-2.986592E+07	-202.14	-202.29	1.49	1.49
C_3N_4(9,0)	-3.137977E+07	-3.137977E+07	-211.16	-211.36	1.51	1.51
C_6N_8(8,4)	-2.963169E+07	-2.963165E+07	-207.14	-176.16	0.63	0.64
P_{grey}(16,8)	-1.016236E+08	-1.016236E+08	-108.98	-108.95	0.78	0.78
P_{black}(11,0)	-9.445903E+07	-9.445903E+07	-328.32	-328.47	0.42	0.42
MoS_2(9,9)	-1.380827E+08	-1.380827E+08	-115.57	-115.85	1.16	1.16
CNT(10,10)	-2.763189E+07	-2.763189E+07	-232.01	-232.13	0.00	0.00

2. Geometric Data for SnIP@2D material hybrids

Table S3: DFT optimized geometric parameters for all used self-standing nanotubes. The given units are Å for distances (e.g. B-N) and degrees (°) for angles (e.g. B-N-B). In carbon nitride, the distinction between cyclic (N_c) and bridging (N_b) nitrogen atoms is implemented.

	hBN(17,0)	C_3N_4(9,0)	C_6N_8(8,4)	P_{grey}(16,8)	P_{black}(11,0)	MoS_2(9,9)	CNT(10,10)
a	8.68	7.99	6.95	9.84	6.69	9.42	7.40
B-N	1.45						
B-N-B	118.7-119.8						
N-B-N	119.7-120.0						
N_b-C		1.40-1.45	1.42-1.44				
N_c-C		1.33-1.34	1.33-1.41				
C-N_b-C		117.3-119.9	113.9-121.8				
C-N_c-C		112.8-113.7	114.7-120.1				
N_c-C-N_c		122.6-124.9	117.7-129.1				
P-P				2.28	2.22-2.28		
P-P-P				84.2-99.8	94.3-101.0		
Mo-S						2.36-2.43	
S-Mo-S						70.8-96.4	
Mo-S-Mo						80.6-85.5	
C-C							1.42-1.43
C-C-C							119.7-119.8

Table S4: DFT optimized geometric parameters for all evaluated hybrids with M-SnIP. The given units are Å for distances (e.g. B-N) and degrees (°) for angles (e.g. B-N-B). The NT-I distance corresponds to the shortest distance between the nanotube and an iodine atom of the outer helix. In carbon nitride, the distinction between cyclic (N_c) and bridging (N_b) nitrogen atoms is implemented.

	hBN(17,0)	C_3N_4(9,0)	C_6N_8(8,4)	P_{grey}(16,8)	P_{black}(11,0)	MoS_2(9,9)	CNT(10,10)
a	8.66	8.00	7.00	9.72	6.79	9.34	7.41
P-P	2.25-2.26	2.22-2.23	2.21-2.22	2.28-2.33	2.21-2.22	2.28-2.29	2.21
P-P-P	98.2-98.4	95.3-96.3	91.3-91.7	99.4-108.6	90.6-90.8	100.9-101.5	93.2-93.4
Sn-I	3.04-3.05	3.05-3.10	3.24-3.32	2.96-3.46	3.14-3.26	2.97-3.03	3.07-3.08
I-Sn-I	151.5-152.2	149.0-151.5	152.8-154.0	150.9-155.9	144.3-148.8	147.6-150.8	147.8-148.0
Sn-I-Sn	107.7-107.8	107.7-109.1	104.5-105.2	95.9-105.7	110.9-112.3	106.5-108.6	110.9-111.1
Sn-P	2.75	2.68-2.71	2.65-2.66	2.74-3.10	2.65-2.68	2.77-2.87	2.65
NT-I	3.20	3.02	3.73	3.25	3.18	3.19	3.20
B-N	1.44-1.46						
B-N-B	118.9-119.2						
N-B-N	119.6-120.5						
N_b-C		1.41-1.45	1.42-1.45				
N_c-C		1.33-1.34	1.33-1.41				
C-N_b-C		117.8-120.1	113.7-123.6				
C-N_c-C		112.9-115.4	115.2-120.8				
N_c-C-N_c		122.6-125.0	116.9-128.7				
P-P				2.28-2.32	2.23-2.31		
P-P-P				79.3-102.6	93.3-113.3		
Mo-S						2.35-2.51	
S-Mo-S						71.9-96.9	
Mo-S-Mo						80.0-81.8	
C-C							1.43
C-C-C							119.6-120.0

Table S5: DFT optimized geometric parameters for all evaluated hybrids with **P-SnIP**. The given units are Å for distances (e.g. B-N) and degrees (°) for angles (e.g. B-N-B). The NT-I distance corresponds to the shortest distance between the nanotube and an iodine atom of the outer helix. In carbon nitride, the distinction between cyclic (N_c) and bridging (N_b) nitrogen atoms is implemented.

	hBN(17,0)	C_3N_4(9,0)	C_6N_8(8,4)	P_{grey}(16,8)	P_{black}(11,0)	MoS_2(9,9)	CNT(10,10)
a	8.66	8.00	7.01	9.72	6.79	9.34	7.41
P-P	2.25-2.26	2.22-2.23	2.21-2.22	2.27-2.33	2.21-2.22	2.28-2.29	2.21
P-P-P	98.2-98.4	95.3-96.4	91.4-91.8	99.4-108.6	90.6-90.8	100.9-101.5	93.2-93.4
Sn-I	3.04-3.05	3.05-3.10	3.22-3.28	2.97-3.46	3.14-3.26	2.97-3.03	3.08
I-Sn-I	151.5-152.0	148.9-151.3	152.0-153.2	150.8-155.8	144.3-148.9	147.8-150.9	147.8-148.0
Sn-I-Sn	107.70	107.8-109.1	105.2-106.8	96.0-105.8	110.9-112.4	106.6-108.6	110.9-111.1
Sn-P	2.75	2.68-2.71	2.64-2.67	2.74-3.10	2.65-2.68	2.77-2.86	2.65
NT-I	3.20	3.03	3.47	3.25	3.17	3.19	3.20
B-N	1.44-1.45						
B-N-B	118.9-119.9						
N-B-N	119.4-120.8						
N_b-C		1.41-1.45	1.42-1.45				
N_c-C		1.33-1.35	1.33-1.41				
C-N_b-C		117.1-120.0	113.6-121.1				
C-N_c-C		113.1-115.4	115.2-120.8				
N_c-C-N_c		122.5-125.0	116.9-128.4				
P-P				2.27-2.32	2.30-3.23		
P-P-P				79.4-102.7	93.2-113.4		
Mo-S						2.34-2.50	
S-Mo-S						70.9-98.1	
Mo-S-Mo						80.0-86.9	
C-C							1.43
C-C-C							119.3-120.0

Table S6: DFT optimized parameters of the C_6N_8 matrix with *M*- and *P*-SnIP. In the first column, the total charge of the mulliken population analysis (MPA) for the atoms (A) of the $[SnI]^+$ helix are given. The two nearest neighbors (NB1 and NB2) and their respective distances (D) to A are shown in the following columns. A, NB1 and NB2 refer to the element and the default numbering in the appended output files and the distances (D) are given in angstrom.

| A	*M*-SnIP					*P*-SnIP				
	MPA	NB1	D (A-NB1)	NB2	D (A-NB2)	MPA	NB1	D (A-NB1)	NB2	D (A-NB2)
Sn113	0.39	N31	3.66	N36	3.84	0.40	N25	4.01	N38	4.40
Sn114	0.39	N32	3.68	C80	4.14	0.36	N29	3.90	C101	3.94
Sn115	0.39	N35	3.71	N51	3.92	0.37	N26	3.59	C98	3.75
Sn116	0.38	N33	3.74	C100	3.87	0.40	N28	3.56	C100	3.95
Sn117	0.38	N38	3.70	C97	4.00	0.39	N31	3.47	C103	3.73
Sn118	0.4	N26	3.69	C98	4.08	0.39	N30	4.61	N35	4.89
Sn119	0.39	N29	3.85	C101	4.41	0.37	C104	4.19	N32	4.22
I120	-0.25	N58	3.78	C95	3.81	-0.22	N35	3.56	C67	3.88
I121	-0.23	N30	3.73	N22	4.03	-0.25	C92	3.58	N63	3.71
I122	-0.23	C89	3.87	N17	3.94	-0.26	C89	3.64	N33	3.65
I123	-0.24	C96	3.88	N59	3.94	-0.23	C95	3.73	N50	3.80
I124	-0.24	N61	3.80	C101	3.83	-0.22	N32	3.56	N8	3.79
I125	-0.25	C92	3.73	N63	3.89	-0.25	N38	3.55	C97	3.65
I126	-0.24	N64	3.61	C104	3.74	-0.21	N29	3.72	N53	3.95

3. COHP of SnIP@C_6N_8:
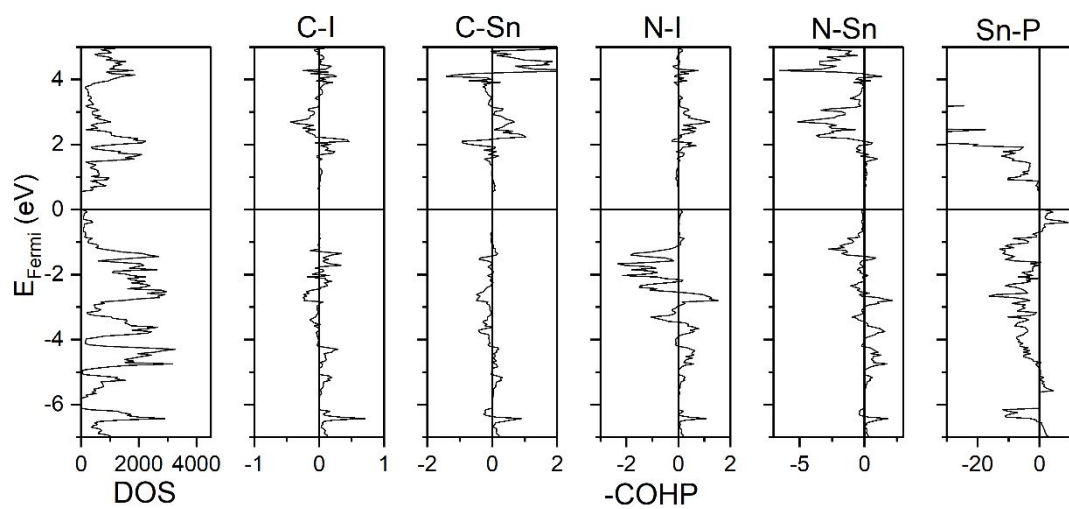
Figure S1: DOS and COHP of the *M*-SnIP@C_6N_8 hybrid. Positive values in the COHP representations correspond to antibonding states and vice versa.
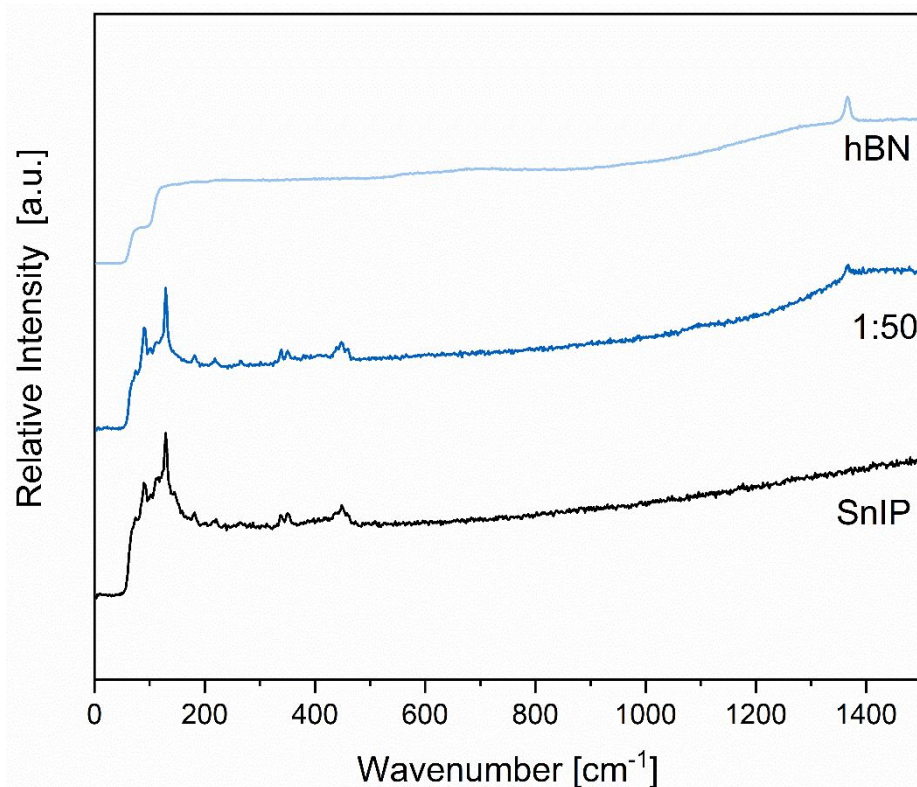
4. Raman Data

Figure S2: Exemplary Raman data of the SnIP@hBN 1:50 hybrid as well as both pristine materials. No new bands appear and thus no new covalent bonds are formed, supporting our core-shell particle claim with purely ionic/van-der-Waals interactions between the two materials.

5. DR-UV/Vis Data
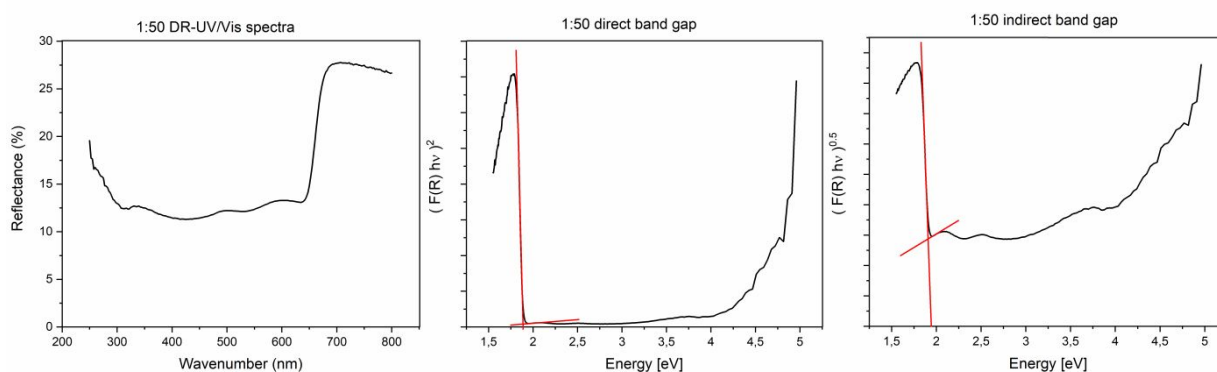

Figure S3: DR-UV/Vis spectra were used to determine bandgaps via double linear fitting of Tauc plots according to Makuła et al. and Gesesse et al[1, 2]. The shown data of the sample SnIP@hBN 1:50 resulted in values of 1.80 eV for the direct bandgap and 1.82 eV for the indirect bandgap.

6. Experimental Data

Synthesis of SnIP:

SnIP was synthesized in a chemical transport reaction according to literature[3]. 22.5 mg P_{red} (> 99.999%, Chempur), Sn (99.99%, VWR Chemicals) and SnI_4 were pressed into a pellet and sealed into a quartz glass ampoule under vacuum ($\rho < 10^{-3}$ mbar). This was heated in a Nabertherm muffle furnace (L3/11/330) to 673 K within 4 h, kept at that temperature for 48 h and then slowly cooled to room temperature for 5 days (120 h). The educts were placed close to the heating plates, enabling gas transport towards the cooler middle of the oven. Phase purity

of the material prior to consecutive experiments was confirmed by phase analysis through powder X-ray diffraction.

Delamination of SnIP:

SnIP bulk material was finely ground in an agate mortar and suspended in chlorobenzene. The suspension was treated for 150 min at 20 000 rpm with an IKA T18 Ultra Turrax and subsequently for 30 h at 0 °C with a Bandelin Sonoplus ultrasonic-homogenizer (70% active time, 85% power) to generate even smaller particles. It was dried in vacuum to yield a homogeneous powder that again was analyzed via powder diffraction.

Delamination of hBN:

Hexagonal boron nitride nanoflakes were acquired with a diameter of around 70 nm (99,99%, CHEMPUR). It was suspended in chlorobenzene, ultra sonicated at 0 °C for 5 h and dried in vacuum.

Synthesis of SnIP@hBN hybrids:

The two materials were weighed in specific ratios, taking into account their molecular weight and crystal structure, suspended in chlorobenzene and ultra sonicated for 30 min at 0 ˚C. They were stirred for 24 h and then dried in vacuum.

Transmission electron microscopy:

TEM was performed on a JEM-1400Flash transmission electron microscope by JEOL with an acceleration voltage of 120 kV. A very dilute suspension of sample in chlorobenzene was deposited on a lacy carbon coated copper TEM grid and dried on air.

Raman Spectroscopy:

Raman spectra were acquired on a RENISHAW nVia RE04 Raman microscope at a laser wavelength of 532 nm at 0.1 % - 1 % power (0.5 - 5 mW) and integration time of 60 s.

Diffuse reflectance UV/Vis:

DR-UVVis data was recorded within a wavelength range of 300 nm to 800 nm on a PERKINELMER Lambda 650 s UV-Vis-NIR spectrophotometer with an integrating sphere.

Data of van der Waals radii (Jmolvdwradii.txt) used in structure drawings, Crystal basis set data (Crystalbasissets.txt) and full Crystal data after structure optimization (Geometries.txt) are attached as separate files.

References:

1.   Makuła, P.; Pacia, M.; Macyk, W., How To Correctly Determine the Band Gap Energy of Modified Semiconductor Photocatalysts Based on UV–Vis Spectra. *The Journal of Physical Chemistry Letters* **2018,** *9* (23), 6814-6817.

2.   Gesesse, G. D.; Gomis-Berenguer, A.; Barthe, M.-F.; Ania, C., On the analysis of diffuse reflectance measurements to estimate the optical properties of amorphous porous carbons and semiconductor/carbon catalysts. *Journal of Photochemistry and Photobiology A: Chemistry* **2020,** *398*, 112622.

3.   Pfister, D.; Schäfer, K.; Ott, C.; Gerke, B.; Pöttgen, R.; Janka, O.; Baumgartner, M.; Efimova, A.; Hohmann, A.; Schmidt, P.; et al., Inorganic Double Helices in Semiconducting SnIP. *Adv. Mater.* **2016,** *28*, 9783-9791.

4 Conclusion

The content of this thesis is centered around the first inorganic double helix compound SnIP, which occurs in a racemic ratio of M- and P-SnIP enantiomers. The structure was analyzed thoroughly by Pfister et al.[34], but the reason for it's formation was cause for controversial discussions. The small discrepancy between P_{black} and SnIP educts pose the question, how this can lead to such completely different systems by essentially only changing the temperature during the synthesis process.

In 3.1 this topic is examined with the CalPhaD program Tragmin by calculating the ratios of relevant gas phase constituents. From there, the GAUSSIAN code is used to screen and evaluate energetically the chemically sensible steps. Results show, that at lower reaction temperature and higher SnI_2 quota the formation of SnIP via a dimerization to Sn_2I_4 is favored. After this intermediate activates the initial P_4 molecules by iodine elimination, both SnIP enantiomers can be achieved by polymerization. It should be mentioned, that the phosphorus helix of SnIP is the one determining the chirality of the system, depending on which side of the butterfly P_4 substructure is opened. However, high reaction temperature and low SnI_2 availability promote the phosphorene formation via a direct opening of the P_4 tetraeder by SnI_2 insertion. It could also be shown, that a saturation with SnI_2 at this stage would lead to an unreactive species and stop the reaction cascade. The opened tetraeders dimerize with each other to form a six-membered ring with two residual P atoms situated opposite to each other. This intermediate can be saturated by two more SnI_2, which are released again when the polymerization happens. For up to 8 phosphorus tetraeders this was shown and the typical corrugation of the phosphorene sheet was already visible in the gas phase. Of course, both systems will crystallize at some point, which was entirely neglected in this project.

For some reason, there is a physical property of SnIP, that could not be understood intuitively. While trying to get nanomaterial from the crystals by a top-down approach a size limit ($\approx$150 Å) occured, below which the seemingly independent double helices could not be separated anymore. This fact alone is the basis for all the following examinations done on the 1D system in the framework of DFT with the Crystal17 code. In 3.2, first of all the energetic influence of a single shell of SnIP rods on the stability of the system was tested. In this shell, six SnIP units, which are either left or right handed, are involved and modified in their chirality (all P-SnIP, all M-SnIP or racemate). The racemic mixture, as it is present in the bulk material, is favored by at least 8.5 kJ/mol per repetition unit compared to the other stacking variants. With the goal of a feasible bottom-up approach to single SnIP strands, the stabilization energy for the integration into CNT matrices with different properties (metallic, semi-metallic

and semiconducting) and diameters (13.8 to 15.1 Å) is calculated. The results show a maximum stabilization in total energy (D3-corrected) for the CNT(15,5) matrix (-364 kJ/mol per repetition unit), while in the bulk material this value is 126 kJ/mol per repetition unit. It's worth mentioning, that all used CNTs are rigid enough to induce geometric adaptions onto the SnIP substructure, while in general retaining their electronic properties. iCOHP analysis suggests, that all the tested matrix-host systems have covalent and dispersive interactions, but antibonding is still the dominant part. In 3.3 it is attempted to change this by keeping the diameter of the matrix comparable (13.1 - 13.8 Å) and varying its constitution. Promising 2D materials like CNT, MoS_2, P_{grey}, P_{black}, the melamine-based carbon nitride C_3N_4, the tri-s-triazine-based carbon nitride C_6N_8 and hBN are rolled-up to form the host cavities. Both enantiomeric forms of double helical SnIP are used for hybrid formation and total energy evaluation. Furthermore, a vibrational as well as a COHP analysis are thoroughly carried out, which permits detailed insight into the complex bonding situations.

In 3.3, table S1 it becomes evident, that stronger bonding between $[SnI]^+$ helix and matrix is not necessarily more favored in total energy because elevated attraction is always accompanied by rising repulsion. In fact, only the P_{black} hybrid has an advantage compared to the CNT system. Features like vacancies (e.g in matrices with C_3N_4 and C_6N_8) or a polar atom distribution (e.g. in systems with hBN, MoS_2, C_3N_4 and C_6N_8) do not lead to the goal, yet. Future projects in this field should focus on the optimization of the 2D materials used for hybrid formation. A better stabilization of single SnIP strands could be possible by identifying more suitable materials or modifying the hybrid. This can be achieved e.g. by doping of the matrix in order to have a majority of bonding states near the Fermi level while at the same time reducing antibonding interactions.

List of Publications

Nanotube Matrices for flexible SnIP Nanowires
M. R. P. Pielmeier, A. Degg, K. Vosseler, T. Nilges, *Journal of Physical Chemistry C*, **2022**, *30*, 12603-12614.

SnBrP - A SnIP-type representative in the Sn-Br-P system
F. Reiter, **M. R. P. Pielmeier**, A. Vogel, C. Jandl, M. Plodinec, C. Rohner, T. Lunkenbein, K. Nisi, A. Holleitner, T. Nilges, *Zeitschrift für Anorganische und Allgemeine Chemie*, **2022**, *e202100347*.

An Ordered Alite Cement Clinker Phase (Ca₃SiO₅, aP162) from Flux Synthesis
A. Utrap, **M. R. P. Pielmeier**, T. Lange, T. Gädt, T. Nilges, *Zeitschrift für Anorganische und Allgemeine Chemie*, **2021**, *647*, 2105.

Ultrafast Photoconductivity and Terahertz Vibrational Dynamics in Double-Helix SnIP Nanowires
D. N. Purschke, **M. R. P. Pielmeier**, E. Üzer, C. Ott, C. Jensen, A. Degg, A. Vogel, N. Amer, T. Nilges, F. A. Hegmann, *Advanced Materials*, **2021**, *33*, 2100978.

Formation Mechanisms for Phosphorene and SnIP
M. R. P. Pielmeier, T. Nilges, *Angewandte Chemie International Edition*, **2021**, *60*, 6816.

Toward Atomic-Scale Inorganic Double Helices via Carbon Nanotube Matrices - Induction of Chirality to Carbon Nanotubes
M. R. P. Pielmeier, A. J. Karttunen, T. Nilges, *Journal of Physical Chemistry C*, **2020**, *124*, 13338-13347.

Flexible and Ultrasoft Inorganic 1D Semiconductor and Heterostructure Systems Based on SnIP
C. Ott, F. Reiter, M. Baumgartner, **M. R. P. Pielmeier**, A. Vogel, P. Walke, S. Burger, M. Ehrenreich, G. Kieslich, D. Daisenberger, J. Armstrong, U. K. Thakur, P. Kumar, S. Chen, D. Donadio, L. S. Walter, R. T. Weitz, K. Shankar, T. Nilges, *Advanced Functional Materials*, **2019**, *29*, 1900233.

NaP$_{7\text{-}x}$As$_x$, Tuning of Electronic Properties in a Polypnictide and Heading towards Helical One-dimensional Semiconductors

M. Baumgartner, T. Wylezich, F. Baumer, **M. R. P. Pielmeier**, A. Vogel, R. Weihrich, T. Nilges, *Zeitschrift für Anorganische und Allgemeine Chemie*, **2017**, *643*, 1881-1887.

References

[1] A. C. Sparavigna, "Materials Science in Ancient Rome," *ARCHAEOGATE*, 2011. Available at SSRN: https://ssrn.com/abstract=2747880.

[2] W. Reschetilowski, "Da ist was dran: 150 Jahre Periodensystem," *Nachrichten aus der Chemie*, vol. 67, no. 6, pp. 8–13, 2019.

[3] W. Hume-Rothery and H. M. Powell, "On the theory of super-lattice structures in alloys," *Zeitschrift für Kristallographie-Crystalline Materials*, vol. 91, no. 1-6, pp. 23–47, 1935.

[4] E. Zintl and G. Brauer, "Über die Valenzelektronenregel und die Atomradien unedler Metalle in Legierungen," *Zeitschrift für Physikalische Chemie*, vol. 20, no. 1, pp. 245–271, 1933.

[5] Fahlman, Bradley, *Semiconducting Materials*, pp. 153–219. Dordrecht: Springer Netherlands, 2007.

[6] Y. Xiao, L. Zheng, and M. Cao, "Hybridization and pore engineering for achieving high-performance lithium storage of carbide as anode material," *Nano Energy*, vol. 12, pp. 152–160, 2015.

[7] M. Park, J. Ryu, W. Wang, and J. Cho, "Material design and engineering of next-generation flow-battery technologies," *Nature Reviews Materials*, vol. 2, no. 1, pp. 1–18, 2016.

[8] S. Sharma, K. K. Jain, A. Sharma, *et al.*, "Solar cells: in research and applications – a review," *Materials Sciences and Applications*, vol. 6, no. 12, p. 1145, 2015.

[9] R. Kshetrimayum, "A brief intro to metamaterials," *IEEE Potentials*, vol. 23, no. 5, pp. 44–46, 2005.

[10] S. Tretyakov, A. Urbas, and N. Zheludev, "The century of metamaterials," *Journal of Optics*, vol. 19, p. 080404, jul 2017.

[11] E. J. Mittemeijer, *Fundamentals of materials science*, vol. 8. Springer, 2010.

[12] Q. He, B. Yu, Z. Li, and Y. Zhao, "Density functional theory for battery materials," *Energy & Environmental Materials*, vol. 2, no. 4, pp. 264–279, 2019.

[13] Y. Peng, C. Huang, J. Huang, M. Feng, X. Qiu, X. Yue, and S. Huang, "Filling Octahedral Interstices by Building Geometrical Defects to Construct Active Sites for Boosting the Oxygen Evolution Reaction on $NiFe_2O_4$," *Advanced Functional Materials*, p. 2201011, 2022.

[14] S. Stranks, "Multimodal microscopy characterization of halide perovskite semiconductors: Revealing a new world (dis)order," *Matter*, vol. 4, no. 12, pp. 3852–3866, 2021.

[15] G. Barrow and G. Herzog, *Physikalische Chemie: Gesamtausgabe.* Springer, 1973.

[16] A. M. Smith and S. Nie, "Semiconductor nanocrystals: structure, properties, and band gap engineering," *Accounts of chemical research*, vol. 43, no. 2, pp. 190–200, 2010.

[17] L. Kou, T. Frauenheim, and C. Chen, "Phosphorene as a Superior Gas Sensor: Selective Adsorption and Distinct I–V Response," *The Journal of Physical Chemistry Letters*, vol. 5, no. 15, pp. 2675–2681, 2014.

[18] S. Das, M. Demarteau, and A. Roelofs, "Ambipolar Phosphorene Field Effect Transistor," *ACS Nano*, vol. 8, no. 11, pp. 11730–11738, 2014.

[19] W. Li, Y. Yang, G. Zhang, and Y.-W. Zhang, "Ultrafast and Directional Diffusion of Lithium in Phosphorene for High-Performance Lithium-Ion Battery," *Nano Letters*, vol. 15, no. 3, pp. 1691–1697, 2015.

[20] H. Liu, A. T. Neal, Z. Zhu, Z. Luo, X. Xu, D. Tomanek, and P. D. Ye, "Phosphorene: An Unexplored 2D Semiconductor with a High Hole Mobility," *ACS Nano*, vol. 8, no. 4, pp. 4033–4041, 2014.

[21] J. B. Smith, D. Hagaman, and H.-F. Ji, "Growth of 2D black phosphorus film from chemical vapor deposition," *Nanotechnology*, vol. 27, no. 21, p. 215602, 2016.

[22] P. Lange, Stefan Schmidt and T. Nilges, "Au_3SnP_7 @ Black Phosphorus: An Easy Access to Black Phosphorus," *Inorganic Chemistry*, vol. 46, no. 10, pp. 4028–4035, 2007.

[23] M. Köpf, N. Eckstein, D. Pfister, C. Grotz, I. Krüger, M. Greiwe, T. Hansen, H. Kohlmann, and T. Nilges, "Access and in situ growth of phosphorene-precursor black phosphorus," *Journal of Crystal Growth*, vol. 405, pp. 6 – 10, 2014.

[24] J. D. Watson and F. H. C. Crick, "Molecular Structure of Nucleic Acids: A Structure for Deoxyribose Nucleic Acid," *Nature*, vol. 171, no. 4356, pp. 737–738, 1953.

[25] F. Cramer, "The Synthesis of Oligo- and Polynucleotides," *Angewandte Chemie International Edition*, vol. 5, no. 2, pp. 173–184, 1966.

[26] X. Fan, E. C. Dickey, P. C. Eklund, K. A. Williams, L. Grigorian, R. Buczko, S. T. Pantelides, and S. J. Pennycook, "Atomic Arrangement of Iodine Atoms inside

Single-Walled Carbon Nanotubes," *Physical Review Letters*, vol. 84, pp. 4621–4624, May 2000.

[27] T. Fujimori, R. B. dos Santos, T. Hayashi, M. Endo, K. Kaneko, and D. Tomanek, "Formation and properties of selenium double-helices inside double-wall carbon nanotubes: experiment and theory," *ACS Nano*, vol. 7, pp. 5607–5613, 2013.

[28] T. Fujimori, A. Morelos-Gomez, Z. Zhu, H. Muramatsu, R. Futamura, K. Urita, M. Terrones, T. Hayashi, M. Endo, S. Y. Hong, Y. C. Choi, D. Tomanek, and K. Kaneko, "Conducting linear chains of sulphur inside carbon nanotubes," *Nature Communications*, vol. 4, p. 2162, 2013.

[29] A. S. Ivanov, T. Kar, and A. I. Boldyrev, "Nanoscale stabilization of zintl compounds: 1D ionic Li-P double helix confined inside a carbon nanotube," *Nanoscale*, vol. 8, no. 6, pp. 3454–60, 2016.

[30] F. Baumer, F. Reiter, and T. Nilges, "Towards MXPn-Type Compounds in the Systems Ge-I-Pn (Pn = P, As) - New Insights in the Structures and Properties of Inverse Type I Clathrates," *Zeitschrift für anorganische und allgemeine Chemie*, vol. 643, no. 21, pp. 1444–1450, 2017.

[31] M. Baumgartner, R. Weihrich, and T. Nilges, "Inorganic SnIP-Type Double Helices in Main-Group Chemistry," *Chemistry - A European Journal*, vol. 23, no. 26, pp. 6452–6457, 2017.

[32] F. Reiter, M. Pielmeier, A. Vogel, C. Jandl, M. Plodinec, C. Rohner, T. Lunkenbein, K. Nisi, A. Holleitner, and T. Nilges, "SnBrP - A SnIP-type representative in the Sn-Br-P system," *Zeitschrift für Anorganische und Allgemeine Chemie*, p. e202100347, 2022.

[33] T. Nilges, D. Pfister, C. Ott, K. Schäfer, M. Baumgartner, and R. Weihrich, "Inorganic Semiconducting Compounds," *German Patent*, no. WO/2017/008979, 2015.

[34] D. Pfister, K. Schäfer, C. Ott, B. Gerke, R. Pöttgen, O. Janka, M. Baumgartner, A. Efimova, A. Hohmann, P. Schmidt, S. Venkatachalam, L. van Wüllen, U. Schürmann, L. Kienle, V. Duppel, E. Parzinger, B. Miller, J. Becker, A. Holleitner, R. Weihrich, and T. Nilges, "Inorganic Double Helices in Semiconducting SnIP," *Advanced Materials*, vol. 28, no. 44, pp. 9783–9791, 2016.

[35] U. Müller, "Die Symmetrie von Spiralketten," *Acta Crystallographica Section B*, vol. 73, no. 3, pp. 443–452, 2017.

[36] M. R. P. Pielmeier, A. J. Karttunen, and T. Nilges, "Toward Atomic-Scale In-organic Double Helices via Carbon Nanotube Matrices - Induction of Chirality to Carbon Nanotubes," *The Journal of Physical Chemistry C*, vol. 124, no. 24, pp. 13338–13347, 2020.

[37] W. Kutzelnigg, *Einführung in die Theoretische Chemie.* Verlag Chemie, 1975.

[38] M. Born and R. Oppenheimer, "On the Quantum Theory of Molecules," *Annalen der Physik*, vol. 84, p. 457, 1927.

[39] W. Heisenberg, "Quantum-theoretical re-interpretation of kinematic and mechanical relations," *Zeitschrift für Physik*, vol. 33, pp. 879–893, 1925.

[40] W. Heisenberg, "Mehrkörperproblem und Resonanz in der Quantenmechanik," *Zeitschrift für Physik*, vol. 38, no. 6, pp. 411–426, 1926.

[41] E. Schrödinger, "Quantisierung als Eigenwertproblem," *Annalen der Physik*, vol. 385, no. 13, pp. 437–490, 1926.

[42] J. C. Slater, "The Theory of Complex Spectra," *Physical Reviews*, vol. 34, pp. 1293–1322, 1929.

[43] D. R. Hartree, "The wave mechanics of an atom with a non-coulomb central field, parts i-iii," in *Mathematical Proceedings of the Cambridge Philosophical Society*, vol. 24, pp. 89–110, 1927.

[44] J. A. Gaunt, "A Theory of Hartree's Atomic Fields," *Mathematical Proceedings of the Cambridge Philosophical Society*, vol. 24, no. 2, pp. 328–342, 1928.

[45] W. Pauli, "Über den Zusammenhang des Abschlusses der Elektronengruppen im Atom mit der Komplexstruktur der Spektren," *Zeitschrift für Physik*, vol. 31, no. 1, pp. 765–783, 1925.

[46] V. Fock, "Näherungsmethode zur Lösung des quantenmechanischen Mehrkörper-problems," *Zeitschrift für Physik*, vol. 61, no. 1, pp. 126–148, 1930.

[47] D. G. Anderson, "Iterative procedures for nonlinear integral equations," *Journal of the ACM*, vol. 12, no. 4, pp. 547–560, 1965.

[48] C. G. Broyden, "A class of methods for solving nonlinear simultaneous equations," *Mathematics of computation*, vol. 19, no. 92, pp. 577–593, 1965.

[49] P. Pulay, "Convergence acceleration of iterative sequences. The case of SCF iteration," *Chemical Physics Letters*, vol. 73, no. 2, pp. 393–398, 1980.

[50] F. Hund, "Zur Deutung verwickelter Spektren, insbesondere der Elemente Scandium bis Nickel," *Zeitschrift für Physik*, vol. 33, no. 1, pp. 345–371, 1925.

[51] F. Hund, "Zur Deutung der Molekelspektren. III.," *Zeitschrift für Physik*, vol. 43, no. 11, pp. 805–826, 1927.

[52] R. S. Mulliken, "The assignment of quantum numbers for electrons in molecules. I," *Physical Review*, vol. 32, no. 2, p. 186, 1928.

[53] F. Hund, "Zur Frage der chemischen Bindung," *Zeitschrift für Physik*, vol. 73, no. 1, pp. 1–30, 1932.

[54] F. Hund, "Zur Frage der chemischen Bindung. II," *Zeitschrift für Physik*, vol. 73, no. 9, pp. 565–577, 1932.

[55] R. S. Mulliken, "Electronic structures of polyatomic molecules and valence. II. General considerations," *Physical Review*, vol. 41, no. 1, p. 49, 1932.

[56] R. A. Kendall, R. J. Harrison, R. J. Littlefield, and M. F. Guest, *High Performance Computing in Computational Chemistry: Methods and Machines*, pp. 209–316. 1995.

[57] LRZ, "Energy Efficient Building Infrastructures," accessed 25.07.2022. https://www.lrz.de/wir/green-it_en/ee-infrastruktur_en.

[58] LRZ, "High Performance Computing," accessed 25.07.2022. https://doku.lrz.de/display/PUBLIC/High+Performance+Computing.

[59] A. Rossi, P. G. Baity, V. M. Schäfer, and M. Weides, "Quantum computing hardware in the cloud: Should a computational chemist care?," *International Journal of Quantum Chemistry*, vol. 121, no. 14, p. e26688, 2021. https://doi.org/10.1002/qua.26688.

[60] R. P. Feynman, "Simulating physics with computers," *International Journal of Theoretical Physics*, vol. 21, pp. 467–488, 1982.

[61] S. Stenholm and K.-A. Suominen, *Quantum Computing*, ch. 4, pp. 130–191. 2005. https://doi.org/10.1002/0471739367.ch4.

[62] T. F. Ronnow, Z. Wang, J. Job, S. Boixo, S. V. Isakov, D. Wecker, J. M. Martinis, D. A. Lidar, and M. Troyer, "Defining and detecting quantum speedup," *science*, vol. 345, no. 6195, pp. 420–424, 2014.

[63] D. Claudino, "The basics of quantum computing for chemists," *International Journal of Quantum Chemistry*, p. e26990, 2022.

[64] J. M. Foster and S. F. Boys, "Canonical Configurational Interaction Procedure," *Rev. Mod. Phys.*, vol. 32, pp. 300–302, 1960.

[65] P. Hohenberg and W. Kohn, "Inhomogeneous Electron Gas," *Physical Reviews*, vol. 136, pp. B864–B871, 1964.

[66] S. Sousa, P. Fernandes, and M. Ramos, "General Performance of Density Functionals," *The Journal of Physical Chemistry A*, vol. 111, pp. 10439–52, 11 2007.

[67] P. Pulay, "Improved SCF convergence acceleration," *Journal of Computational Chemistry*, vol. 3, no. 4, pp. 556–560, 1982.

[68] D. Hamann, "Semiconductor charge densities with hard-core and soft-core pseudopotentials," *Physical Review Letters*, vol. 42, no. 10, p. 662, 1979.

[69] T. J. Ypma, "Historical development of the Newton-Raphson method," *SIAM review*, vol. 37, no. 4, pp. 531–551, 1995.

[70] R. Dovesi, A. Erba, R. Orlando, C. M. Zicovich-Wilson, F. Pascale, B. Civalleri, K. Doll, N. M. Harrison, I. J. Bush, P. D'Arco, M. Llunel, M. Causa, Y. Noel, L. Maschio, M. Erba, M. Rerat, and S. Casassa, "CRYSTAL17 - User's Manual," 2017. https://www.crystal.unito.it/manuals/crystal17.pdf.

[71] I. Muz and M. Kurban, "Zinc oxide nanoclusters and their potential application as CH_4 and CO_2 gas sensors: Insight from DFT and TD-DFT," *Journal of Computational Chemistry*, vol. 43, no. 27, pp. 1839–1847, 2022.

[72] P. R. Linnebank, A. M. Kluwer, and J. N. H. Reek, "Unraveling the Origin of the Regioselectivity of a Supramolecular Hydroformylation Catalyst," *ChemCatChem*, p. e202200541. https://doi.org/10.1002/cctc.202200541.

[73] D. Zagorac, J. Zagorac, M. Fonovic, M. Pejic, and J. C. Schön, "Computational discovery of new modifications in scandium oxychloride (ScOCl) using a multimethodological approach," *Zeitschrift für anorganische und allgemeine Chemie*. https://doi.org/10.1002/zaac.202200198.

[74] R. Dovesi, A. Erba, R. Orlando, C. M. Zicovich-Wilson, B. Civalleri, L. Maschio, M. Rerat, S. Casassa, J. Baima, S. Salustro, and B. Kirtman, "Quantum-mechanical condensed matter simulations with CRYSTAL," *WIREs Computational Molecular Science*, vol. 8, no. 4, p. e1360, 2018.

[75] F. Bloch, "Über die Quantenmechanik der Elektronen in Kristallgittern," *Zeitschrift für Physik*, vol. 52, no. 7, pp. 555–600, 1929.

[76] V. V. Porsev, A. V. Bandura, and R. A. Evarestov, "Ab initio modeling of helically periodic nanostructures using CRYSTAL17: A general algorithm first applied to nanohelicenes," *Computational Materials Science*, vol. 203, p. 111063, 2022.

[77] S. A. Egorov and R. A. Evarestov, "Antiferromagnetism-induced spin splitting in monolayers of layered and non-layered crystals: Symmetry-based analysis and Density Functional Theory calculation," *Physica E: Low-dimensional Systems and Nanostructures*, vol. 139, p. 115118, 2022.

[78] N. Dimakis, S. Gupta, R. Wadud, and M. I. Bhatti, "Computational data of molybdenum disulfide/graphene bilayer heterojunction under strain," *Data in Brief*, vol. 42, p. 108054, 2022.

[79] M. Hart, E. R. White, J. Chen, C. M. McGilvery, C. J. Pickard, A. Michaelides, A. Sella, M. S. P. Shaffer, and C. G. Salzmann, "Encapsulation and Polymerization of White Phosphorus Inside Single-Wall Carbon Nanotubes," *Angewandte Chemie, International Edition*, vol. 56, pp. 8144–8148, 2017.

[80] N. L. Marana, S. Casassa, and J. R. Sambrano, "Piezoelectricity induced by gaseous molecules adsorbed on ZnO nanotubes," *Materials Science and Engineering: B*, vol. 281, p. 115729, 2022.

[81] R. Dronskowski and P. E. Bloechl, "Crystal orbital Hamilton populations (COHP): energy-resolved visualization of chemical bonding in solids based on density-functional calculations," *The Journal of Physical Chemistry*, vol. 97, no. 33, pp. 8617–8624, 1993.

[82] R. Dronskowski, "Crystal Orbital Hamilton Populations: The Official Reference Page," 2003 (accessed 03.05.2022). www.cohp.de.

[83] H. Wolff and R. Dronskowski, "First-principles and molecular-dynamics study of structure and bonding in perovskite-type oxynitrides ABO_2N (A = Ca, Sr, Ba; B = Ta, Nb)," *Journal of Computational Chemistry*, vol. 29, no. 13, pp. 2260–2267, 2008.

[84] S. Maintz, V. L. Deringer, A. L. Tchougreeff, and R. Dronskowski, "LOBSTER: A tool to extract chemical bonding from plane-wave based DFT," *Journal of Computational Chemistry*, vol. 37, no. 11, pp. 1030–1035, 2016.

[85] J. George, G. Petretto, A. Naik, M. Esters, A. J. Jackson, R. Nelson, R. Dronskowski, G.-M. Rignanese, and G. Hautier, "Automated Bonding Analysis with Crystal Orbital Hamilton Populations," *ChemPlusChem*, p. e202200123.

[86] R. Nelson, C. Ertural, J. George, V. L. Deringer, G. Hautier, and R. Dronskowski, "LOBSTER: Local orbital projections, atomic charges, and chemical-bonding analysis from projector-augmented-wave-based density-functional theory," *Journal of Computational Chemistry*, vol. 41, no. 21, pp. 1931–1940, 2020.

[87] M. Frisch, G. Trucks, H. Schlegel, G. Scuseria, M. Robb, J. Cheeseman, G. Scalmani, V. Barone, B. Mennucci, G. Petersson, *et al.*, "Gaussian09, Version 9.6," 2009. Gaussian, Inc, Wallingford, CT.

[88] N. H. Vu, H. C. Dong, M. V. Nguyen, D. Hoang, T. T. Trinh, and T. B. Phan, "Mechanism of proton transport in water clusters and the effect of electric fields: A DFT study," *Current Applied Physics*, vol. 25, pp. 62–69, 2021.

[89] V. Sharma, B. Roondhe, S. Saxena, and A. Shukla, "Role of functionalized graphene quantum dots in hydrogen evolution reaction: A density functional theory study," *International Journal of Hydrogen Energy*, 2022.

[90] R. Dennington, T. Keith, J. Millam, *et al.*, "GaussView, Version 5.0.9," 2009. Semichem Inc., Shawnee Mission, KS.

[91] M. S. Teynor, W. Scott, and D. H. Ess, "Catalysis with a Skip: Dynamically Coupled Addition, Proton Transfer, and Elimination during Au-and Pd-Catalyzed Diol Cyclizations," *ACS Catalysis*, vol. 11, no. 16, pp. 10179–10189, 2021.

[92] R. Bormann, F. Gärtner, and K. Zöltzer, "Application of the CALPHAD method for the prediction of amorphous phase formation," *Journal of the Less Common Metals*, vol. 145, pp. 19–29, 1988.

[93] E. Schnedler, "The calculation of complex chemical equilibria," *CALPHAD*, vol. 8, no. 3, pp. 265–279, 1984.

[94] U. Steiner, "Tragmin: Berechnung von Transport-Gleichgewichten durch Minimierung der freien Enthalpie Version 5.1," *HTW Dresden*, 2008.

[95] M. Schöneich, M. Schmidt, and P. Schmidt, "Chemical Vapour Transport of Bismuth and Antimony Chalcogenides M_2Q_3 (M = Sb, Bi, Q = Se, Te) ," *Zeitschrift für anorganische und allgemeine Chemie*, vol. 636, no. 9-10, pp. 1810–1816, 2010.

[96] S. Golbs, F. M. Schappacher, R. Pöttgen, R. Cardoso-Gil, A. Ormeci, U. Schwarz, W. Schnelle, Y. Grin, and M. Schmidt, "Europium Phosphate, Europium Arsenate, and Europium Antimonate - Correlation of Crystal Structure and Physical Properties," *Zeitschrift für anorganische und allgemeine Chemie*, vol. 639, no. 12-13, pp. 2139–2148, 2013.

[97] A. Utrap, N. Y. Xiang, and T. Nilges, "A yield-optimized access to double-helical SnIP via a Sn/SnI$_2$ approach," *Journal of Crystal Growth*, vol. 475, pp. 341–345, 2017.

[98] C. Ott, F. Reiter, M. Baumgartner, M. Pielmeier, A. Vogel, P. Walke, S. Burger, M. Ehrenreich, G. Kieslich, D. Daisenberger, J. Armstrong, U. K. Thakur, P. Kumar, S. Chen, D. Donadio, L. S. Walter, R. T. Weitz, K. Shankar, and T. Nilges, "Flexible and Ultrasoft Inorganic 1D Semiconductor and Heterostructure Systems Based on SnIP," *Advanced Functional Materials*, vol. 29, p. 1900233, 2019.

[99] J. Gracia and P. Kroll, "Corrugated layered heptazine-based carbon nitride: the lowest energy modifications of C$_3$N$_4$ ground state," *Journal of Materials Chemistry*, vol. 19, no. 19, 2009.